Materials Science and Engineering, Volume 42, No. 1 (2017), pp. 5–12.

EFFECT OF SAND QUALITY ON GAS EVOLUTION DURING DIPPING INTO LIQUID ALUMINUM

ENIKŐ ÁDÁM[1]–GYÖRGY FEGYVERNEKI[2]–
CSABA CSÁSZÁR[3]–JENŐ DÚL[4]

The amount of evolved gas was examined during decomposition of cold-box binder in this study. Spherical core samples were used for the COGAS tests with different binder content and basic sand. The volume and rate of gas evolution were increasing both by the ratio of fine and separated black (used) sand in the mixture. The gas evolution rate was higher by 60% in case of separated black sand than at reclaimed sand. The measurement results were use in the simulation of the filling process.

Keywords: sand core, cold-box, spherical sample, COGAS test, evolving gas

INTRODUCTION

The knowledge of the core properties and sand mixtures is important for designing and manufacturing the molding process. The binders start to decompose and evolve to gas when the sand cores are in contact with the liquid metal. This gas can cause casting defects.

Measurements of the evolved gas were performed on cold-box samples with the COGAS measuring equipment. Considering the results of gas evolution rate can be drawn valuable conclusion in order to ensure good mould filling.

1. EVOLVING GAS FROM THE RESIN BONDED SAND MIXTURES

The quantity and pressure of evolved gas have influence on the quality of castings. The adsorbed moisture is evaporated by heat load at lower temperature. The binder degradation processes and partial decomposition of bonding bridges start at further increasing of temperature. The dry distillation and complete decomposition of binder components start at 700 °C [1]. The quantity of evolved gas from the resin bonded sand mixtures is influenced by the type and quantity of binder, granulometry properties of sand, geometry, type of coating used, core storage time and molten metal temperature [1–3].

---

[1] Nemak Győr Aluminium Foundry Ltd.
Ipari Park – Nyírfa sor, Győr 9027
eniko.adam@nemak.com

[2] Nemak Győr Aluminium Foundry Ltd.
Ipari Park – Nyírfa sor, Győr 9027
gyorgy.fegyverneki@nemak.com

[3] Nemak Győr Aluminium Foundry Ltd.
Ipari Park – Nyírfa sor, Győr 9027
csaba.csaszar@nemak.com

[4] University of Miskolc, Institute of Foundry Engineering
Miskolc-Egyetemváros 3515, Hungary
ontdul@uni-miskolc.hu

2. EXPERIMENTAL METHODS

The tool insert made for a multi-step series of measurements. This study was the first phases enter. The shape of the test piece is relevant in later phases. Green sand (fine and medium grain size) mixtures, reclaimed sand mixtures (fine and medium grain size) and sand mixtures with black sand were examined *(Table 1)*. The samples were blown by core blowing machine. Cylindrical specimen core box was completed with a removable tool insert in one cavity *(Figures 1–3)*. Uniform and stabile measurement conditions were provided by the use of spherical core samples. Spherical cold-box core samples (d = 32 mm) were dipped into liquid aluminum. Cold-box resin and activator addition were modified in order to prepare the core samples. *Table 2* contains the information of examined sand mixtures.

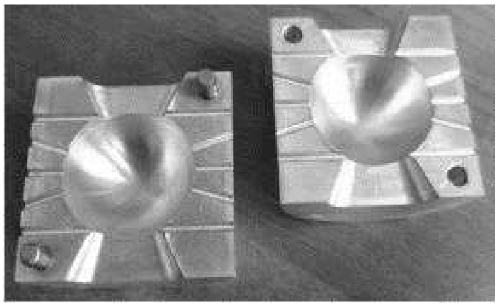

Figure 1
Used tool insert for the core shooting

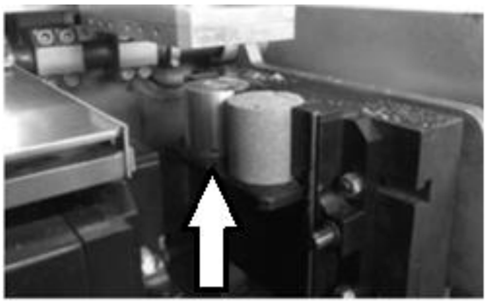

Figure 2
Cylindrical specimen core box with a removable tool insert in one cavity

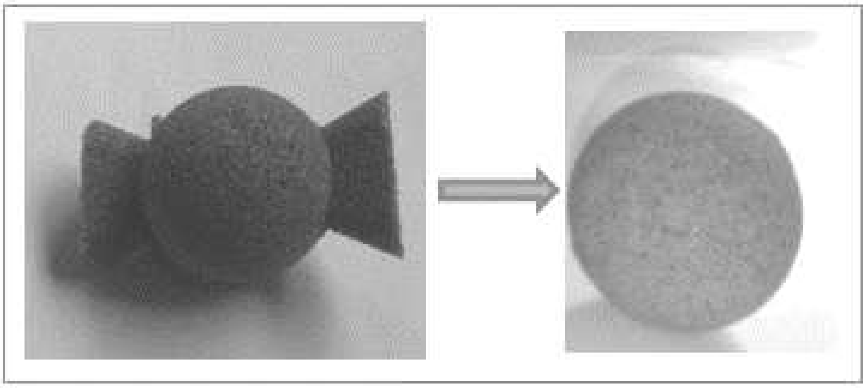

Figure 3
Rough-and prepared specimen

Table 1
Examined sands

Identification	
SH32	Green sand - Medium grain size silica sand (Šajdíkove Humence)
F35	Green sand - Fine grain size silica sand (Frechen)
RM	Medium grain size silica sand (thermal reclaimed sand in the foundry)
RF	Fine grain size silica sand (thermal reclaimed sand in the foundry)
B	Separated black silica sand (only mechanically reclaimed sand)

The company have thermal sand reclamation system. There are 3 possible sand conditions for core making: green sand, thermal reclaimed sand and only mechanically reclaimed sand.

Table 2
Information from the examined sand mixtures

Type of sand		**Identification**	**Resin content, %**	**Mean grain size, mm**	**Loss on ignition, %**
Green sand	SH32	SH32	0.55	0.524	1.09
	F35	F35	0.55	0.22	0.85
Reclaimed sand	Medium	RM 0.4	0.4	0.477	0.67
		RM 0.55	0.55		0.85
		RM 0.7	0.7		1.12
	Fine	RF 0.55	0.55	0.239	0.84
		RF 0.7	0.7		1.11
Mixed sand	B = 25% RM = 75%	25B–75RM	0.55	0.475	1.17
	B = 50% RM = 50%	50B–50RM	0.55	0.465	1.27
Black sand	Separated black sand	B	0.55	0.453	1.75
Moisture is under 0.1% except of separated black sand					

The cores were dipped into the melt during the COGAS tests. The gas flow is evolving from the sample due to the heat load and it was registered and recorded during 180 seconds. The gas passes the core through a thin metal pipe which is fit onto the surface of core. The gas is going through a cooled condensate trap. The chemicals with low boiling point are condensated and the rest part of the gas going to the gas collector. The amount of core gas was determined by the amount of water displaced in gas collector [4].

Figure 4 shows the COGAS equipment.

The measurements were made with COGAS measuring equipment at the Nemak Győr Ltd. The temperatures of liquid metal were 690 ^{0}C or 720 ^{0}C during the tests.

The samples had same size, but the weight were different, because of different grain size. We defined values of specific amount of gas to compare these sand mixtures. The specific amount of gas is the quantity of evolved gas during 180 seconds divided by the mass of specimen (ml/g).

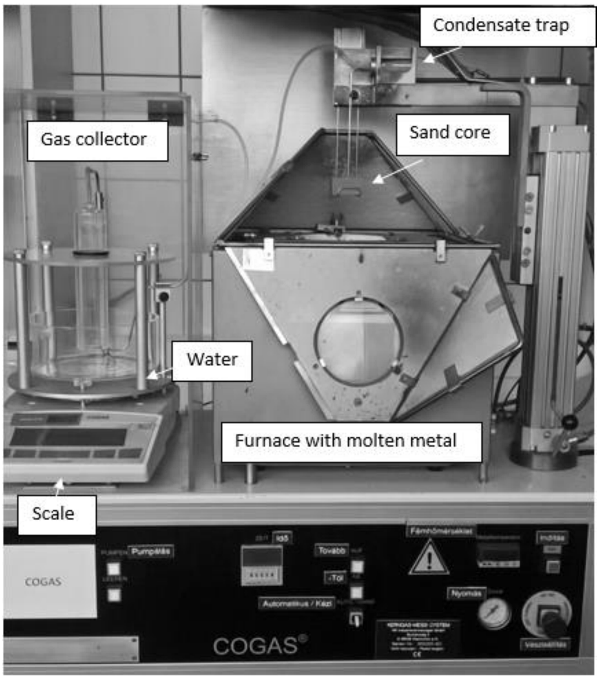

Figure 4
The COGAS equipment

3. EVALUATION OF RESULTS

3.1. The effect of basic sand quality

We examined the influence of the quality of basic sand to the amount of evolved gas. We compared sand mixtures with different grain size (fine and medium) but the same ratio of binder. The specific amount of gas was bigger at fine sand as medium sand. We found the specific amount of gas was bigger at fine sand as at reclaimed and green sand. The difference was same at 690 and 720 ^{0}C too.

The effect of reclamation is an important factor. In case of SH32 sand the value of specific amount of gas is bigger than at reclaimed medium sand. This can be explained by a higher loss on ignition of green sand (organic impurities). It contains more organic material, but we didn't find this relation between reclaimed medium and fine sand.

The separated black sand that haven't been reclaimed and it have a high content of residual organic material. Remains of different type of binders (binders of cold-box and hot-box methods used in the foundry) are on the surface of the black sand grains. Knowing that the different binder systems burn out differently from the sand cores. Therefore the value of evolved gas is different too [5]. The amount of evolved gas is grown thus the heat transport intensifies by increasing the ratio of separated black sand.

The value of specific amount of gas is bigger by more than 1 ml/g in case of separated black sand mixture than the reclaimed at 720 ^{0}C *(Figure 5).*

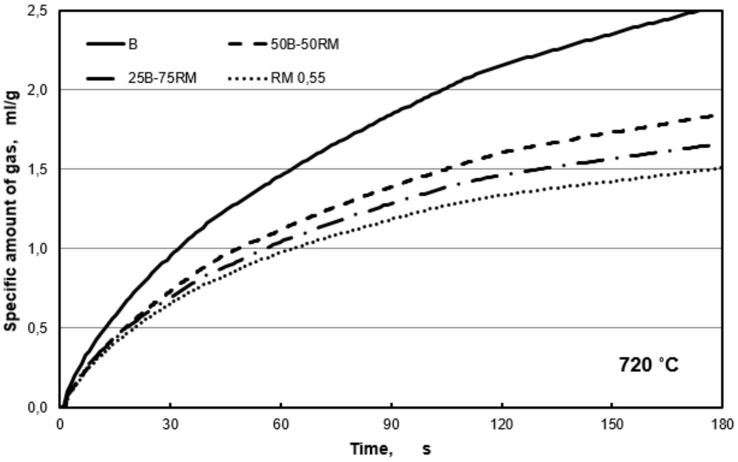

Figure 5
Effect of ratio of separated black sand

3.2. Effect of binder system

The amount of evolving gas increases in case of fine and medium grain sized sand (contained the same quantity of resin) by increasing the resin content. The specific amount of gas increases more than 15% by increasing the resin content *(Figure 6* and *7).*

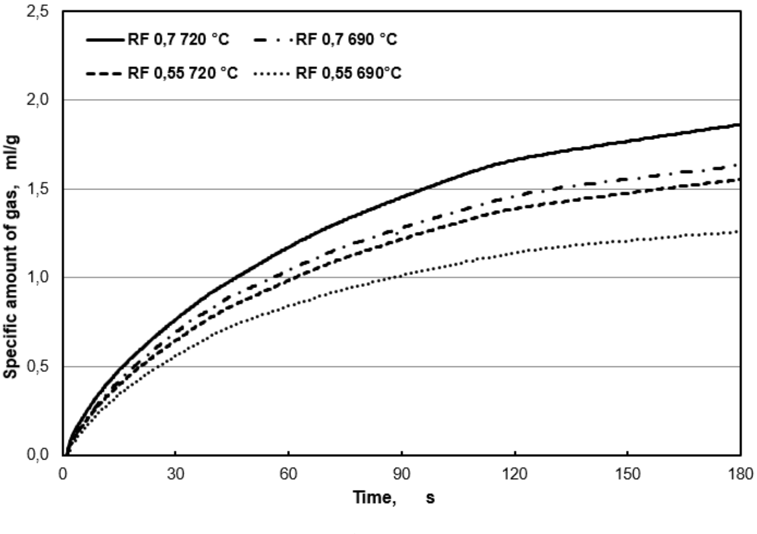

Figure 6
Effect of binder content at different temperatures in case of fine grain size sand and different resin content

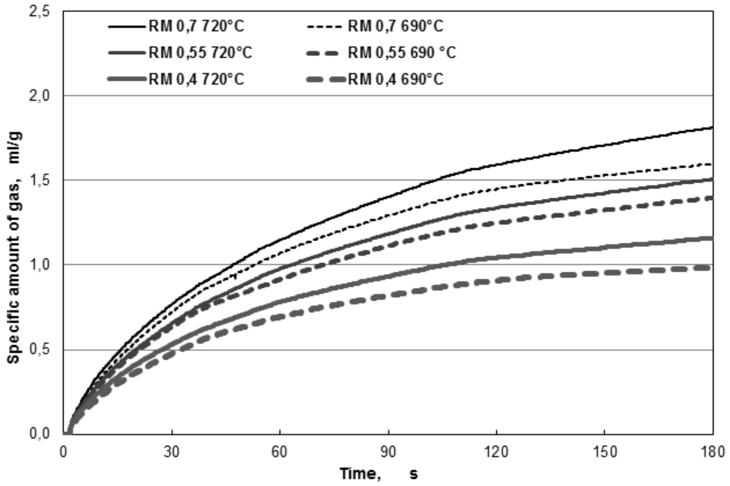

Figure 7

Effect of binder content at different temperatures in case of medium grain size sand and different resin content

3.3. The relative amount of condensate

The amount of condensate is different in each mixture. It is influenced by the temperature of liquid metal and the binder content. Higher binder content causes bigger amount of condensate. The separated black sand content in the mixture increases the amount of condensate too.

3.4. Relative amount of gas in various intervals

Table 3

Relative amount of gas in different intervals, Resin content 0.55%, test temperature 690 °C

690 °C	**Relative amount of gas, %**			
Mixture/ Interval	**1st period**	**2nd period**	**3rd period**	**4th period**
	0–30 s	**30–60 s**	**60–120 s**	**120–180 s**
SH32	49.14	20.21	23.32	7.34
F35	44.47	23.06	26.78	5.69
RM 0.55	45.95	22.47	23.73	7.85
RF 0.55	45.38	22.19	23.35	9.08
25B–75RM	44.62	21.89	23.86	9.62
50B–50RM	43.65	22.07	27.15	7.13
B	40.4	21.24	25.31	13.05

The test time was divided into periods. We observed that the gas formed in different amounts *(Table 3* and *4)*.

40–50% of the gases evolve during the first period after dipping the samples into liquid metal. During the next 30 s this amount is halved. It's the same quantity of the evolving gas forming during the second minute. The remaining quantity (7–13%) evolves during the third minute.

At lower temperature (690 °C) during the first 30 s more gas evolve higher in percent than at 720 °C.

Table 4

Relative amount of gas in different intervals,
Resin content 0.55%, test temperature 720 °C

720 °C	**Relative amount of gas, %**			
Mixture/ Interval	**1st period**	**2nd period**	**3rd period**	**4th period**
	0–30 s	**30–60 s**	**60–120 s**	**120–180 s**
SH32	46.37	20.22	22.58	10.83
F35	42.88	20.8	25.07	11.25
RM 0.55	48.6	21.73	22.39	7.27
RF 0.55	41.77	21.67	25.89	10.67
25B–75RM	41.49	20.89	25.54	12.08
50B–50RM	39.91	20.67	26.46	12.95
B	38.31	19.88	26.79	15.02

3.5. Gas evolution rate

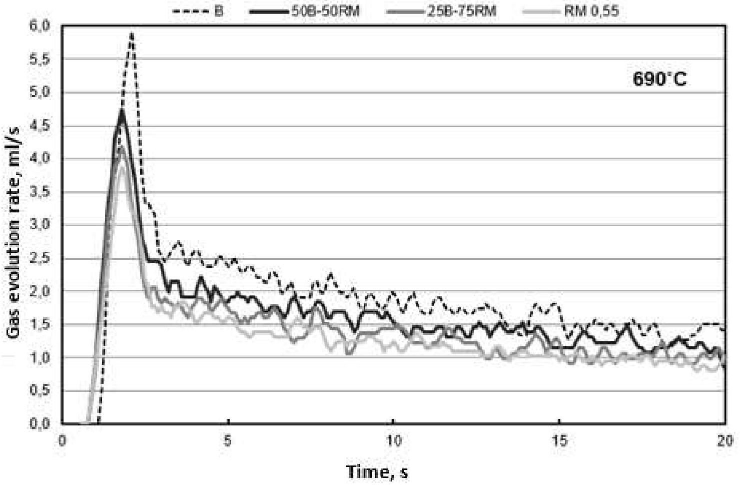

Figure 8

Gas evolution rate in case of sand mixtures contained black sand

The gas evolution rate was different at different test temperatures. The gas evolution rate was directly proportional to the amount of resin in case of same basic sand. The biggest intensity measured right after dipping the samples into the melt. Thereafter the intensity decreased gradually. Pressure increase can be observed during the first seconds. The reason of this observation is the suddenly evolved gas amount caused by the warming of trapped air in the pore and the presence of large temperature gradient on the mould wall. It fills the pores and the gas evolution starts [6].

The gas evolution rate increases by increasing the ratio of black sand in case of mixtures contained black sand *(Figure 8).*

CONCLUSIONS

The aim of this study is the statement of factors that have an influence on the amount and intensity of evolved gas from the sand core mixtures. Uniform and stabile measurement conditions are provided by the use of spherical core samples. Thus the results were comparable for evaluation.

The results can be used in the simulation of filling process.

ACKNOWLEDGEMENT

The research was supported by the Nemak Győr Ltd. and the Foundry Institute at University of Miskolc.

REFERENCES

[1] SVIDRÓ J.: *Transzportfolyamatok a fém/formázóanyag határfelületen*. PhD-értekezés, Miskolci Egyetem, 2011. 77, 78, 81, 82, 43–45, 51.

[2] ORLENIUS, J.–GOTTHARDSSON, U.–DIÓSZEGI, A.: Mould and core gas evolution in grey iron castings. *International Journal of Cast Metals Research,* 2008.

[3] WINARDI, L.–GRIFFIN, R. D.–LITTLETON, H. E.–GRIFFIN, J. A.: Variables affecting gas evolution rates and volumes from cores in contact with molten metal. *American Foundry Society Transactions,* 2008.

[4] BENDER, W.: MK Industrievertretungen GmbH: The COGAS Measuring Process. *Manufacturer's description,* http://www.mk-gmbh.de/

[5] ÁDÁM E.–MÁDI L. J.: Műgyantás homokkeverékek gyantakiégési folyamatának vizsgálata. *Bányászati és Kohászati Lapok,* 2015. 6. 20.

[6] TÓTH L.: A vegyi kötésű formázóanyagokból öntés során képződő gázoknyomás változásainak elemzése. *Bányászati és Kohászati Lapok – Öntöde,* 1986. 6. 130–134.

Materials Science and Engineering, Volume 42, No. 1 (2017), pp. 13–20.

INVESTIGATIONS TO REDUCE THE INCLUSION CONTENT IN AL-SI FOUNDRY ALLOYS

MARIANNA BUBENKÓ[1]–MONIKA TOKÁR[2]–
GYÖRGY FEGYVERNEKI[3]

The aim of the experiments with various Al-Si alloys was to examine how different experimental conditions affect the inclusion content of the molten alloys. The utilisation of two cleaning salts from different manufacturers were examined during degassing treatment, in case of *AlSi7MgCu0.5* alloy.

In order to determine the degree of purity, K-mould test were carried out and evaluated. To acquire more realistic results, several test bars were prepared for each technological step.

Beside K-moulds, test bars for density index (Dichte-index) measurement were also casted, to determine the dissolved hydrogen content of the melt.

Keywords: Al-Si alloy, inclusion, K-mould, cleaning salt, rotary degassing, electron microscope, aluminium accompanying elements

INTRODUCTION

The main issue of any melting and melt treatment technology is the reduction of the inclusion content in the melt. Casting defects can result in unfavourable mechanical properties, and the machine tools may be broken by the inclusions. The aim of the optimisation of melt treatment is to achieve such melt purity that reduces the inclusion content of melts as much as possible. The effects of various cleaning salts added during degassing were compared.

Non-metallic accompanying elements are usually oxides, nitrides and other intermetallic phases which develop into independent phases and damage the homogeneity of the metallic structure. The strength of the equipment part is drastically lowered because of the negative effect of the oxides, especially the oxide film, on the exterior notch sensitivity of the castings. To achieve adequately high casting quality, the prevention of impurities in the melt and the casting is essential. Thus, the determination of melt quality is necessary [1].

The presence of impurities in the structure may result in the development of stress concentrators which may lead to decreased mechanical properties. The most common form of impurities in aluminium melts are oxide films and fine disperse oxide inclusions [2].

The mechanical properties of castings are impaired by inclusions and other hydrogen porosities. Small fractures can arise at such impaired surfaces of castings as a result of pressure or other kinds of stresses, leading to even more damage [3].

Many types of inclusions can be in the melt. Oxides, membranes and films are the most common inclusions. These are formed during oxidation, or by reacting with steam [1, 3].

---

[1] University of Miskolc, Institute of Foundry Engineering
Miskolc-Egyetemváros 3515, Hungary
b.marianna1228@gmail.com

[2] University of Miskolc, Institute of Foundry Engineering
Miskolc-Egyetemváros 3515, Hungary

[3] University of Miskolc, Institute of Foundry Engineering
Miskolc-Egyetemváros 3515, Hungary

The quality of the base material is of high importance for the production of foundry castings, which can be significantly improved by melt preparation. The quality of Al-Si based foundry alloys relate to their accompanying element content. Secondary base material, which is made out of scrap metal, is used in higher and higher proportions and the effects of the possible accompanying elements are not fully understood [4].

1. EXPERIMENTAL

1.1. The reduction of gas content using flushing treatment with inert gas

The primary gases used for flushing metal treatment are nitrogen, argon and chlorine. The oxides present in the melt are flushed to the surface where they are bound by the previously applied salt layer. The gas is added mainly through graphite pipes during spinning rotary treatment. In order to achieve as much diffusion surface as possible, the bubbles floating to the melt surface should be as small and as many as possible [1, 2].

In case of the rotary metal cleaning equipment used, inert gas is added from above in the direction of the rotor shaft, where it exits to the melt on the bottom of the mixing head (rotor head). The purpose of the rotary movement is to create finer and more equal gas distribution, and to provide homogenous bubble ration in the melt. This is a widespread method for hydrogen removal from aluminium melts [3, 5, 6].

1.2. Lowering the inclusion content by salt addition during degassing

K-mould test were carried out to detect the inclusions and density index test to determine the dissolved hydrogen content.

K-mould tests were carried out to detect the inclusions by counting the number of impurities using a stereo microscope, then calculating the K-values using *Equation (1)*. K-values determine the purity of the melt. The melts were classified based on the given ranges of K-values in *Table 1* [2].

$$\mathbf{K} = \frac{S}{n} \tag{1}$$

where: **S** = the number of inclusions on the fractured surface; **n** = the number of fractured surfaces (n = 4) [2].

Table 1

Melt classification based on K-values [2]

Classification	*K-value*	*Melt quality*
A	< 0.1	Pure
B	0.1 – 0.5	Relatively pure
C	0.5 – 1.0	Somewhat pure
D_1	1.0 – 2.0	Impure
D_2	2.0 – 5.0	
D_3	5.0 – 10	Impure
E	> 10	Extremely impure

Density index tests are frequent measurement methods in foundries. These are indirect and discontinuous manufacturing tests. The results of the density index measurements give information on the effectiveness of the melt treatment. Density index can be determined based on the density of the test bar at 80 mbar pressure. Classification is based on the relation to theoretical density [2].

The density of the test bar has to be determined after cooling (the density is determined with Archimedes' principle) *(Figure 1)* [2].

Figure 1

"MK 2200" type precision scale for density index measurements (1 – Sample stage of the scale; 2 – Test bar container in distilled water) [2]

The density index values (DI %) were determined with the following equation:

$$DI = \frac{D_1 - D_2}{D_1} \cdot 100 \ (\%) \qquad (2)$$

where: **DI** – density index (%), **D2** – the density of the test bar crystallised and cooled on the metal test bar holder of the "MK3VT" type equipment, at 1 bar pressure (g/cm^3) (reference density), **D3** – the density of the test bar crystallised and cooled inside the "MK2VT" type equipment, at 80 mbar pressure (g/cm^3) [2].

2. RESULTS

2.1. AlSi7MgCu0.5 alloy – the comparison of the effects of "A" and "B" cleaning salts

The aim of cleaning salt addition is to make the aluminium oxide inclusions of the melt less dense and easier to remove in the form of another compound. Because of their non-wettability, these compounds float to the surface either with or without the nitrogen bubbles.

The two types of cleaning salts used are named "A" type salt and "B" type salt. Technological test bars were prepared from 15–15 doses in case of both salts. Test bars were prepared for K-mould test, density index test, chill test and thermal analysis as well.

2.2. The results of K-mould tests

The average K-values of the test with the two cleaning salts at each technological step are illustrated on *Figure 2*.

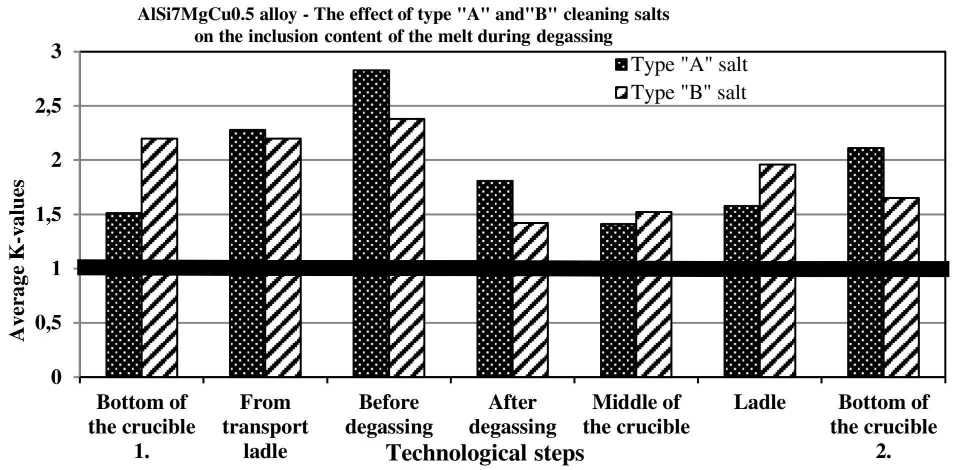

Figure 2
The comparison of the K-values of the two cleaning salts

The results show that the inclusion content of the samples from the melts treated with type "A" and "B" are almost identical. It can be observed that the inclusion content of both melts were decreased after degassing. This means that the use of cleaning salts is effective, as it resulted in decreased K-values and number of impurities.

The thick black line illustrates the level of impurity. Thus, the quality of the each melt sample is considered impure (based on the values in *Table 1*). However, these values are obviously improved, as it is confirmed by the results of the mechanical property analyses.

2.3. Density index test results

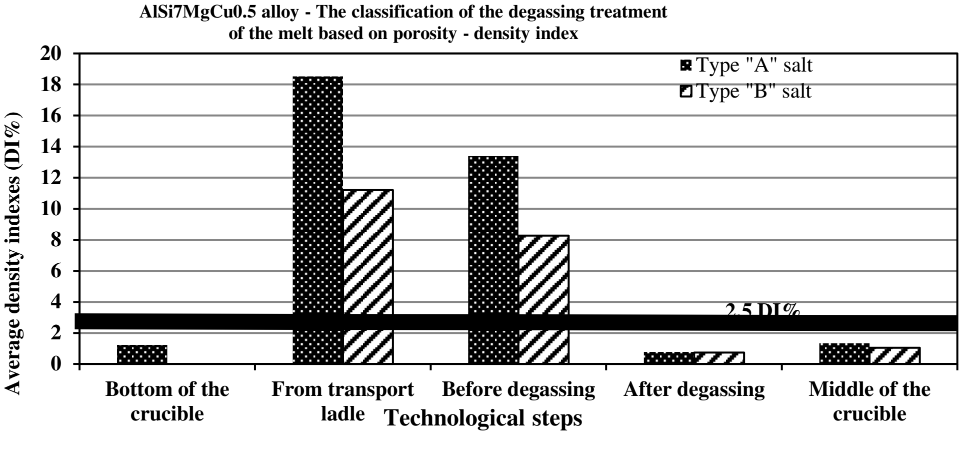

Figure 3
Density index results

In parallel with the preparation of K-mould samples, the density index test bars were prepared to determine the dissolved hydrogen content.

Figure 3 shows the density index values.

The specified values are not exceeded by the density index values. As a result of the effective degassing treatment, the density index values were within the limit after degassing.

2.4. Examination of mechanical properties

Castings made out of the previously selected melts were also selected. After heat treatment, tensile test specimens were prepared to determine the yield point, tensile strength and elongation of the specimens, also the Brinell-hardness of the experimental casting.

The measured values of yield point, tensile strength, Brinell-hardness and elongation are summarised in *Table 2*. The specification values are also given in the second column.

Table 2
The mechanical properties and specifications of the test bars

AlSi7MgCu0.5 alloy	Specification	Type "A" salt	Type "B" salt
Yield point (Rp 0.2 [MPa])	***min. 120***	168.9	168.1
Tensile strength (Rm [MPa])	***min. 200***	234.6	234.9
Brinell-hardness	***70–90***	79.4	79.5
Elongation (A [%])	***min. 1.5***	9.94	10.33

Based on the results, it can be concluded that the mechanical property values were almost identical in case of each salts. The Brinell-hardness values did not exceed the limit value, and the rest of the results were above the given minimum values. The elongation values were approximately ten times higher than the limit value. This is the result of the purity of the structure of the castings, the elongation values are high for this reason. If these values were higher, the inclusion content of the castings would be higher.

2.5. The examination of inclusions with scanning electron microscope (SEM)

The inclusions on the surfaces of the K-mould samples were examined with stereo and scanning electron microscopes. Typical K-mould samples with inclusions were selected for the scanning electron microscopy analysis.

Figure 4 shows the surface of the test bar for the K-mould test, prepared from the melt with **type "A" cleaning salt**, using the leftover melt on the bottom of the crucible after emptying the holding furnace. *Figure 5* illustrates the electron microscopic image (200X magnification) of the impurity on the surface.

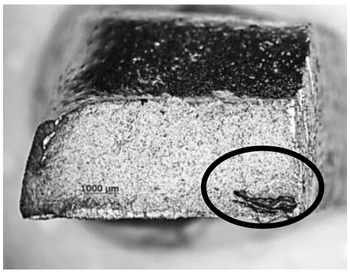

Figure 4
The impure surface of a K-mould test bar on stereo microscope

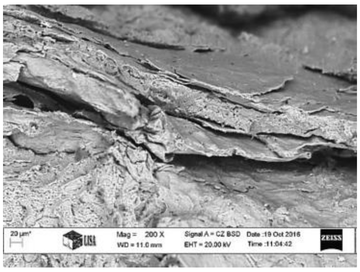

Figure 5
SEM image of the impure K-mould test bar surface, M = 200x

The results of the SEM analysis of the test bar in *Figure 5* can be found in *Table 3*.

Table 3
The results of the SEM analysis of the test bar

Elements (wt%)	**C**	**N**	**O**	**Mg**	**Al**	**Si**	**Cl**	**Cu**	**Total**
Average surface	**2.58**	**8.75**	**5.97**	**1.8**	**68.3**	**11.07**	**0.15**	**1.37**	**100**

Based on the SEM analysis of K-mould samples from the melt with type "A" cleaning salt it can be determined that the oxygen, nitrogen and carbon content of the section with inclusions, Al and Mg oxides developed.

Figure 6 shows the surface of the test bar for the K-mould test, prepared from the melt treated with **type "B" cleaning salt**, under the same condition as the previous test bar. The electron microscopic image of the inclusion with 500X magnification can be observed on *Figure 7*. The results of the SEM analysis can be seen in *Table 4*.

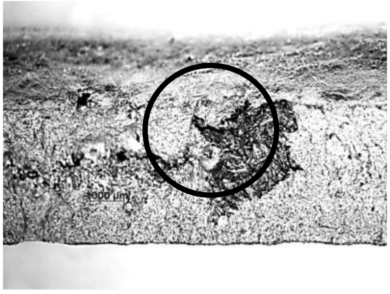

Figure 6
The impure surface of a K-mould test bar on stereo microscope

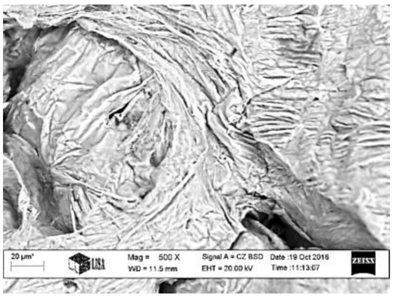

Figure 7
SEM image of the impure surface of the K-mould test, N = 500x

Table 4
Elemental composition based on the average surface analysis

Elements (wt%)	**C**	**O**	**Mg**	**Al**	**Si**	**Cu**	**Total**
Average surface	**1.1**	**8.74**	**3.3**	**69.25**	**16.53**	**1.09**	**100**

Based on the results in *Table 4*, the oxygen content suggests the presence of Al and Mg oxides on the fracture surface. The thick polyhedral oxide layer might be caused by the Mg content.

The fracture surfaces of the K-mould test bars contained Al and Mg oxide inclusions in both cases of type "A" and "B" cleaning salt treatments.

According to the tests using cleaning salts, the inclusion content is decreased during rotary degassing treatment. This is confirmed not only the K-mould tests and the density index values, but the results of the analysis of the slag removed after degassing as well. The slag samples collected after degassing from the melt with type “A” and “B” salts were powdery and their aluminium content was smaller than the slag’s of the non-treated melt. *Figure 8* illustrates the SEM image of the slag sample of the melt after degassing using type “A” salt, with 1000X magnification. The elemental compositions of the numbered spots can be found in *Table 5*.

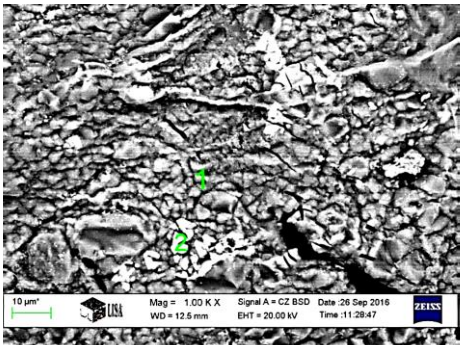

Figure 8
The SEM image of the slag from the melt, using type “A” cleaning salt, after degassing

Table 5
The composition of the slag from the melt with type “A” cleaning salt, after degassing

Test	***Type “A” cleaning salt***											
Elements (wt%)	**Na**	**N**	**O**	**Mg**	**Al**	**S**	**Sr**	**Si**	**Cl**	**Mn**	**Fe**	**Total**
Spot 1	**0.29**	**0.51**	**4.62**	**1.55**	**47.23**	**0.55**	**0**	**44.91**	**0.35**	**–**	**–**	**100**
Spot 2	**0.14**	**1.07**	**2.23**	**0.92**	**78.76**	**0.38**	**0**	**6.61**	**0.29**	**2.69**	**6.91**	**100**

The SEM image (25X magnification) of the slag from the melt, prepared using type “B” cleaning salt and after degassing can be seen on *Figure 9*, while *Table 6* contains the average surface values.

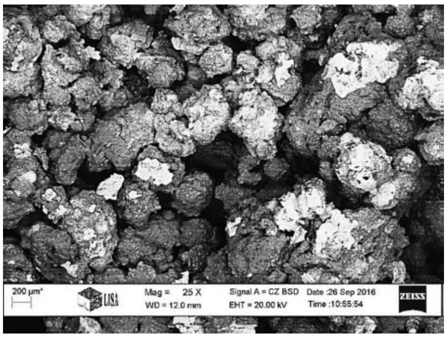

Figure 9
The SEM image of the slag from the melt, using type “B” cleaning salt, after degassing

Table 6

The results of SEM analysis of the slag from the melt, using type "B" cleaning salt, after degassing

Test	***Type "B" cleaning salt***									
Elements (wt%)	**C**	**O**	**Na**	**Mg**	**Al**	**Sr**	**S**	**Cl**	**K**	**Total**
Average	**8.64**	**38.01**	**18.39**	**3.34**	**9.50**	**2.05**	**0.30**	**14.76**	**5.00**	**100**

The slag obtained after the cleaning salt treatment contains various compounds. The oxide and chloride content of the slag from type "A" salt were lower, while slag from type "B" salt has low aluminium content but with relatively high strontium loss.

CONCLUSIONS

The effects of two cleaning salts on *AlSi7MgCu0.5* alloy were examined. It was concluded that the effects of type "A" and "B" salts on the inclusion content of the melt were almost identical. In both cases, the inclusion content were smaller after degassing than it was without salt treatment. The K-values were below 2.0 in case of both cleaning salts.

The tests confirmed that the hydrogen content decreased below the limit value because of the rotary degassing treatment.

According to the scanning electron microscopy analysis, Al and Mg oxide inclusions developed in case of both cleaning salts. Chlorine can be found in the melt treated with type "B" melt, which may be the result of a high dose of cleaning salt addition.

ACKNOWLEDGEMENT

The main author is thankful for the rest of the authors' help, patience and advice to make the realisation of this article possible.
The authors are grateful to Árpád Kovács from the Institute of Physical Metallurgy, Metal Forming and Nanotechnology at the University of Miskolc for carrying out the tests with scanning electron microscope.
The authors are grateful to Mária Ambrus for her advice.

REFERENCES

[1] SZOMBATFALVY A.: Járműipari öntészeti AlSi – ötvözetek tulajdonságainak vizsgálata – PhD-értekezés. 2012. 17., 23.

[2] JÓNÁS P.: Könnyűfém öntészeti ismeretek tankönyv, 2011. 182–183.

[3] KAUFMAN, J. G.–ROOY, E. L.: *Aluminium Alloy Castings – Properties, Process and Applications*. ASM International, 2004. 50.

[4] TOKÁR M.–TÓTH M.–DÚL J.–FEGYVERNEKI Gy.: Szennyezőelemek változékonysága az öntészeti Al-Si-ötvözetekben. BKL, *Kohászat,* 2012. 5. 25.

[5] Foseco Products & Services, Non Ferrous Foundry, Melt Treatment, Metallurgical & Pouring Coveral System, Degassing Equipment & Metal Treatment Station. https://www.vesuvius.com/en/our-solutions/international/foundry/non-ferrous-foundry/melt-treatment.html

[6] BROWN, J.: *Foseco – Non-Ferrous Foundryman's Handbook*. 1999. 73–74.

Materials Science and Engineering, Volume 42, No. 1 (2017), pp. 21–28.

THE DETERMINATION OF THE PROPERTIES OF FOUNDRY SANDS WITH DYNAMIC SPECTRAL ANALYSIS

VIKTÓRIA DARGAI[1]–HARTMUT POLZIN[2]–LÁSZLÓ VARGA[3]

The granulometric properties of foundry sands with different grain sizes and granular structures were determined using standard grading analysis and dynamic spectral analysis. The results of the two analyses were compared and the reasons behind their differences were revealed.

Keywords: sieve analysis, granulometric properties, spectral analysis, foundry sand

INTRODUCTION

One of the most important properties of foundry sands is grain size, along with grain distribution. These granulometric properties are taken into consideration in case of buying basic sand and are continuously monitored by foundries during the manufacturing process. The determination of these properties has various methods, including dry dispersion and laser diffraction [1].

In case of dry dispersion, two methods can be distinguished: conventional granulometric analysis or sieve analysis and grain distribution determination via spectral analysis. Classification using spectral analysis counts as a fairly new method in case of foundry sands. The method of operation differs from the operation of standard sieve analysis. In order to achieve this economically and efficiently, foundries should stay up-to-date with the latest technologies and apply these if possible.

1. STANDARD SIEVE ANALYSIS

50 g sand samples were used for standard sieve analysis. The various sieve sizes used for the measurements are summarised in *Table 1*.

Numerous parameters of the various sand samples can be determined based on the evaluation of the data from the sieve analysis. Some of these parameters can be calculated from the cumulative curve of the sample [3]. A cumulative curve and its evaluation can be seen in *Figure 1*.

The average grain size D (mm) and the degree of uniformity E (%) can be determined based on the cumulative curve, which are related to the quality of sands with respect to the grain distribution. The average grain size value equals with the theoretical size of the sieve on which 50% of the analysed sand passes through and 50% is retained. Equality ratio can

---

[1] University of Miskolc, Institute of Foundry
Miskolc-Egyetemváros 3515, Hungary

[2] Freiberg University of Mining and Technology
Akademiestraße 6, 09599 Freiberg, Germany

[3] University of Miskolc, Institute of Foundry
Miskolc-Egyetemváros 3515, Hungary
ontvlaci@uni-miskolc.hu

be determined based on the mean particle size. In this case, a value 1/3 smaller than the mean particle size at a certain point and a value 1/3 higher than the mean particle size at another point are determined. The difference of these values is the equality ratio in percentages [3].

Table 1

Sieve sizes for standard sieve analysis [2]

Sieve size (mm)	1.400 <
	1.400 – 1.000
	1.000 – 0.710
	0.710 – 0.500
	0.500 – 0.355
	0.355 – 0.250
	0.250 – 0.180
	0.180 – 0.125
	0.125 – 0.090
	0.090 – 0.063
	< 0.063

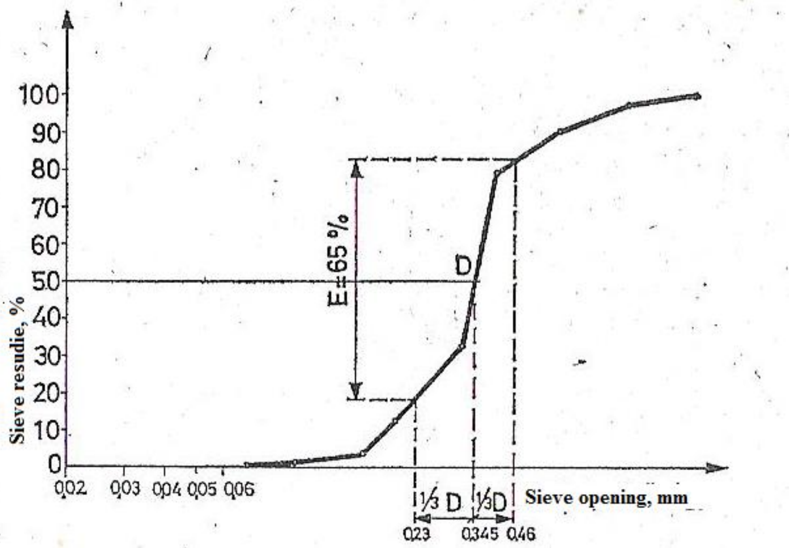

Figure 1

A cumulative curve and its evaluation [3]

2. THE DETERMINATION OF GRAIN STRUCTURE WITH SPECTRAL ANALYSIS

Static and dynamic spectral analysis can be distinguished. The static spectral analysis (Standard ISO 13322-1) is based on the operating principles of a microscope. During the analysis, the grains are spread on a holder and photos are taken to determine the size and shape of the grains. Gravity evening the sand grains makes this method advantageous as the particles can be studied with a depth of field (Ɛ) well-controlled by the optics. Thus, the needle-like shapes of sand grains can be properly measured and graded as well. The disadvantage of static spectral analysis is that only a small portion of sample can be analysed. Averagely only a few 1000 particles can be photographed at once which makes the precision of the results restricted and the evaluation is aggravated by the overlapping particles. The schematic structure of spectral analysis can be seen on *Figure 2*.

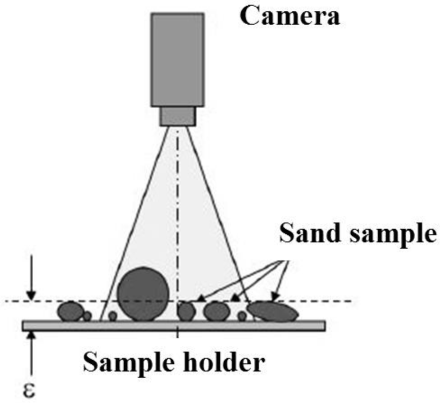

Figure 2
The theoretical structure of spectral analysis [1]

During dynamic spectral analysis (Standard ISO 13322-2), pictures are taken of freely moving sand particles by a fixed camera. Based on the 2D projection of the particles their sizes are determined. The schematic structure of dynamic spectral analysis can be observe on *Figure 3* [1].

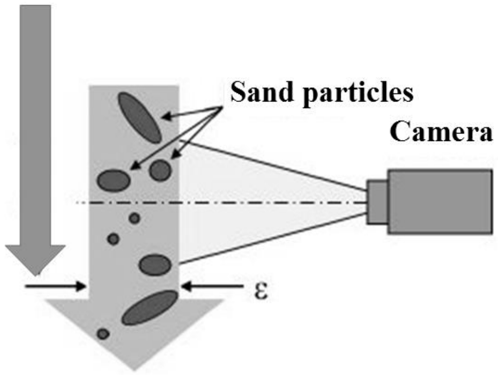

Figure 3
The theoretical structure of dynamic spectral analysis [1]

3. THE FRITSCH ANALYSETTE 28 DYNAMIC IMAGE SIZER

Figure 4 shows a Fritsch Analysette 28 equipment. This instrument operates on the operating principles of dynamic spectral analysis. It is suitable for the determination of the size and shape of sand grains. The pictures taken by the camera can be evaluated with the help of the Image Sizing Software (ISS). Changing the photo/second ratio is possible to increase the precision of the measurement. The grain size can be measured from 20µm to 20 mm. The shapes and shape factors of the sand grains can be determined based on the pictures taken by the camera [4] [5].

Figure 4
A Fritsch Analysette 28 equipment [4]

4. THE COMPARISON OF THE RESULTS OF THE STANDARD SIEVE ANALYSIS AND THE DYNAMIC SPECTRAL ANALYSIS

Granulometric properties of sand samples with various grain sizes and grain distributions were measured with both standard sieve analysis and an Analysette 28 equipment. The measurements were carried out at the sand laboratory of the Institute of Foundry Technology at Freiberg University. The aim of the measurements was to determine the differences between the granulometric parameters measured with standard sieve analysis and dynamic spectral analysis.

The average grain sizes which were determined with both standard sieve analysis and Analysette 28 are summarised in *Table 2.*

Table 2

The average grain sizes determined with standard sieve analysis and Analysette 28

Sand sample	**Average grain size (mm), Standard sieve analysis**	**Average grain size (mm), Analysette 28**	**Deviation from sieve analysis (%)**
F-70	0.20	0.20	0.00
FMX-40	0.38	0.35	–7.89
H32	0.30	0.28	–6.67
Szerb 0.24	0.24	0.20	–16.67
GBM 45	0.37	0.33	–10.81
Regenerated fine sand	0.25	0.23	–8.00
SH 32	0.39	0.38	–2.56
SH 32 regenerated	0.36	0.33	–8.33
SH 34	0.23	0.21	–8.70

The deviation of average grain size values calculated from the cumulative curves representing the granulometric properties measured with standard sieve analysis and Analysette 28 were between 0–17%. The average grain size values determined with dynamic spectral analysis were lower than the average grain size values determined with standard sieve analysis in almost all cases.

The degrees of uniformity determined with both standard sieve analysis and the Analysette 28 equipment are summarised in *Table 3.*

Table 3

The degree of uniformity values determined with standard sieve analysis and Analysette 28

Sand sample	**Degree of uniformity (%), Standard sieve analysis**	**Degree of uniformity (%), Analysette 28**	**Deviation from sieve analysis (%)**
F-70	73	71	–2.74
FMX-40	70	60	–14.29
H32	70	71	1.43
Szerb 0.24	64	52	–18.75
GBM 45	70	54	–22.86
Regenerated fine sand	90	65	–27.78
SH 32	81	68	–16.05
SH 32 regenerated	86	68	–20.93
SH 34	81	57	–29.63

The deviation of the degrees of uniformity calculated from the cumulative curves representing the granulometric properties measured with standard sieve analysis and Analysette 28 were between 2–30%. The degrees of uniformity determined with dynamic spectral analysis were lower than the degrees of uniformity determined with standard sieve analysis in almost all cases.

The reasons behind the deviations can be attributed to the inhomogeneity of the sand samples and the differences between the two measuring methods. Sand grains occur in various, complex shapes, the size of which cannot be characterised with only one parameter. The shape of grain particles can be spheroidal, flat or completely irregular. The more complex the shape is, the more difficult it is to describe it. Thus, the particles are normally characterised by the diameter of a theoretical sphere during spectral analysis that is similar to the examined particle from a certain aspect. This parameter is called geometrical diameter in case of geometrical similarity and equivalent diameter in case of any other physical parameters [6].

Values determined using equivalent diameter during spectral analysis might drastically deviate from values determined by standard sieve analysis.

3–7% deviation is the technological tolerance of the sieve sizes used for sieve analysis. However, certain holes might be 50% larger than the standardised size. The shape of the particles might lead to miscalculations as well. The flatter or more misshaped the particle is, the more likely it is retained on the sieve. Furthermore, elongated (acicular shape) particles with smaller size than length may fall through sieves [6]. The cumulative curves of sample H32 were recorded using the data from both standard sieve analysis and the Analysette 28 equipment. The difference between the cumulative curves from the two measurements can be seen in *Figure 5*.

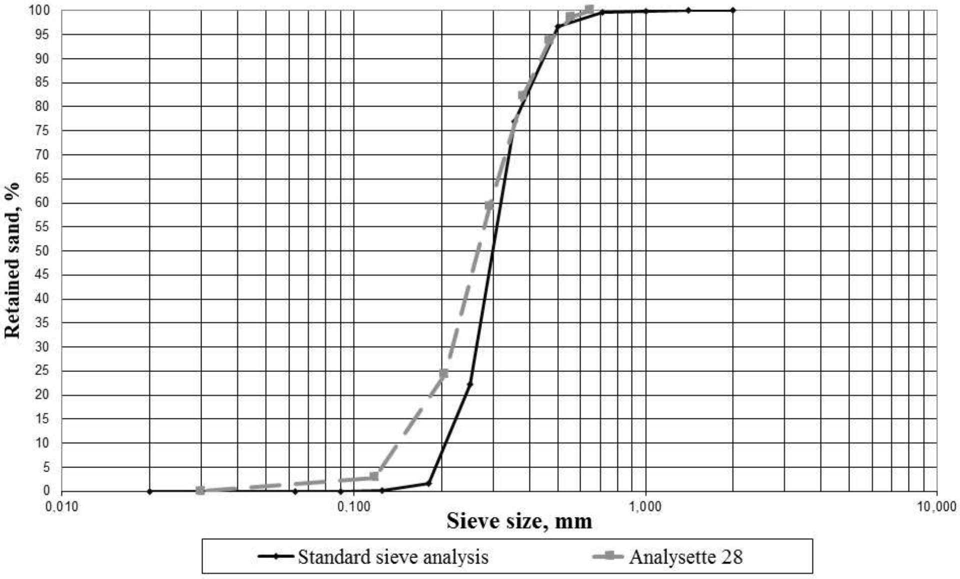

Figure 5
The cumulative curves for sample H32

The deviation between the average grain size values and the differing slopes of the two cumulative curves can be observed on *Figure 5*. The result of these differences is the deviation of the degrees of uniformity. The reasons behind the deviations can be attributed to the various shapes of the sand samples and the differences between the two measuring methods. The differences between sand particles can be determined by the photos of dynamic spectral analysis. However, this method of determination is rather subjective. A photo of sample H32 can be examined on *Figure 6*, while a photo of sample SH34 can be seen on *Figure 7*.

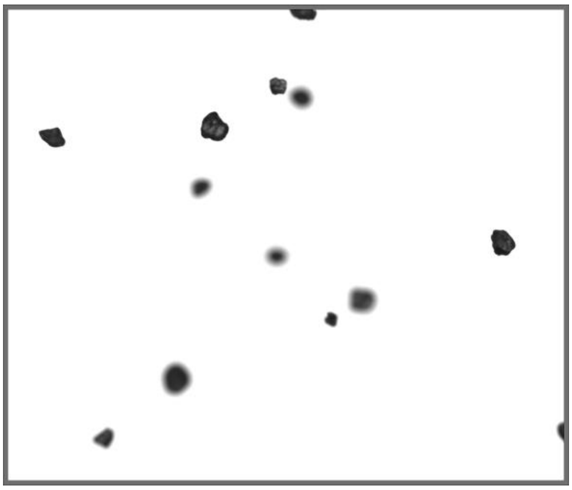

Figure 6
Photo of sample H32 during dynamic spectral analysis

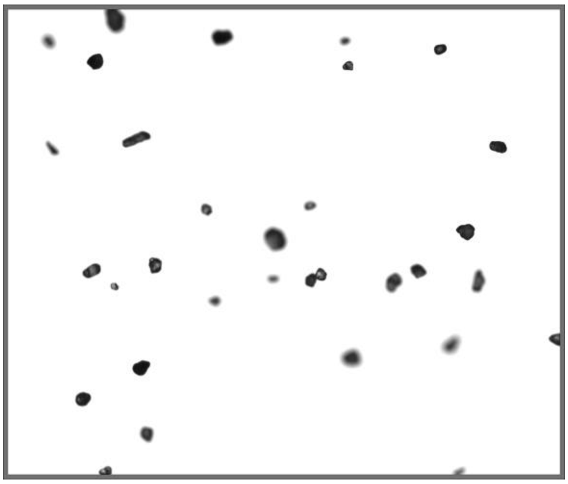

Figure 7
Photo of sample SH 34 during dynamic spectral analysis

CONCLUSION

Based on the comparison of the data determined with standard sieve analysis and dynamic spectral analysis it can be concluded that both the average grain size values and the degrees of uniformity differ. This result is supported by data from international literature [7]. Fast measurements make the usage of Analysette 28 advantageous, especially economically, but in case of sands with elongated, flat or misshaped particles deviations should be expected which may be compensated using a suitable software. The shapes, shape factors and further morphological parameters of the base sand can be determined using the photos from dynamic spectral analysis. The safety of the production can be improved with such further details which can provide basis for determining subsequent relations as well.

ACKNOWLEDGEMENT

The authors are grateful to Mária Ambrus for her advice.

REFERENCES

[1] WITT, DR.RER.NAT. WOLFGANG–KÖHLER, DR.-ING. ULRICH–LIST, DR.-ING. JOACHIM: *Hochgeschwindigkeits Bildanalyse zur Charakterisierung von Partikelgrösse und – form*, Sympatec GmbH, System-Partikel-Technik, Am Pulverhaus 1, 38678 Clausthal-Zellerfeld 1–27.

[2] POLZIN, DR. ING. HABIL. HARTMUT–TILCH, PROF. EM. DR.–ING. HABIL. DR. H.C. WERNER: *Grundlagen der Formstoffe.* (Vorlesungsunterlagen) Freiberg, 2013.

[3] *Öntészeti szabványok.* II. kötet. Szabványkiadó, 1977

[4] Fritsch-Sizing. Access date: 05. 03. 2017
http://www.fritsch-sizing.de/uploads/tx_downloads/e_ANALYSETTE_28_ImageSizer.pdf

[5] Fritsch-Sizing. Access date: 05. 03. 2017
http://www.fritschSizing.de/fileadmin/Redakteur/Downloads/Reports_sizing/Dynamic_Image_Analysis/Partikelanalyse_mit_der_Kamera.pdf

[6] Dr. TÖRÖK, T.–FERENCZI, T.–SZIRMAI, G.: *Pormetallurgia.* Nemzeti Tankönyvkiadó. Access date: 18. 03. 2017.
http://www.tankonyvtar.hu/hu/tartalom/tamop425/0001_1A_A4_01_ebook_pormetallurgia_poranyagok_gyartasa_es_feldolgozasa/adatok.html

[7] Retsch Technology. Access date: 09. 03. 2017
http://www.retsch-technology.de/de/rt/applikationen/fachberichte/

Materials Science and Engineering, Volume 42, No. 1 (2017), pp. 29–35.

DEVELOPMENT OF COOLING TECHNOLOGY OF ALUMINIUM CASTINGS WITH COMPUTATIONAL FLUID DYNAMICS SIMULATIONS

RÓBERT DÚL[1]–GYÖRGY FEGYVERNEKI[2]

In this article parameters of surface heat transfer that can be influenced by the designer of cooling technology are outlined. Their effect on the efficiency of heat transfer are described. We also highlight the fact that Computational Fluid Dynamics (CFD) simulations provide data of vital importance for the user (ie. the foundry) in terms of demanding casting cooling technological parameters and for the mechanical designer of the cooling line in terms of how to fulfill those demands.

Keywords: cylinder head, controlled cooling, fluid dynamics simulation, heat transfer coefficient,

INTRODUCTION

From heat transfer viewpoint we face two essential challenges with regards to castings. The first one is that a certain mass of metal that corresponds to the casting, feeder and every other metallic parts of the casting assembly must be melted. The second one is that the freshly cast assembly must be cooled down to be handled later on in the production process. The efficiency of putting in then later removing heat energy plays an important role in terms of production cost as well.

This article deals with the cooling part of heat transfer challenge and also the benefits of using Computational Fluid Dynamics (from now on CFD) simulations for the design of controlled casting cooling are discussed [1]. By applying numerical simulations cooling technology of castings can be constructed and fulfillment of requirements in terms of mechanical properties which are strongly connected to intense cooling of freshly cast parts can be assured.

1. HEAT BALANCE OF CASTING

The practical use of numerical simulation of heat transfer between casting and surrounding environment enables the foundry to set realistic requirements towards cooling equipment supplier and to check the offered mechanical structure whether it meets these requirements before investing time and money into building it. Simulation can be regarded as a laboratory in which ideas can be tested: try setups of casting and air cooling nozzle positions, directions of cooling, investigate whether forced air cooling, high pressure air cooling or air + water vapour cooling is the right choice for the given production process.

---

[1] CFD Engineering Hungary Kft.
15. Pálya u., Erdőkertes 2113
robert.dul@cfdengineering.hu

[2] Nemak Győr Aluminium Foundry Ltd.
Ipari Park – Nyírfa sor, Győr 9027
gyorgy.fegyverneki@nemak.com

In order to check a casting cooling line, or to define cooling intensity necessary to decrease temperature of a net 22 kg aluminium casting from 530 °C to 80 °C in 80 minutes, heat content of the casting assembly must be known.

Let us look at the whole process as two arms of the balance. On one side there is the heat content of the casting assembly which was just removed from die. On the other side – when air cooling is used – there are positions of casting and cooling nozzle, average velocity of cooling air, its temperature and its humidity, which can be summarized as the intensity of cooling, with other words the capacity of transferring heat from the solid object into the cooling medium.

These two sides are characterized by one equation for each:

heat content of casting given in Joule: $Q = c \cdot m \cdot \Delta T,$ (1)

heat flux from the surface of solid given in Watt: $P_q = \alpha \cdot F(T_{wall} - T_{air}).$ (2)

where:

c: specific heat of solid [J/kgK],

ΔT: temperature difference of object having mass “m” during heat transfer [°C],

α: heat transfer coefficient [W/m^2K],

F: size of surface through which heat can be extracted [m^2],

T_{wall}: temperature of surface to be cooled [°C]

T_{air}: temperature of cooling medium (currently air) [°C]

These two sides are connected unitwise by the time given to carry out cooling process, since W = J/s.

2. HEAT CONTENT OF CASTING ASSEMBLY

Let us take a closer look at the heat content of the casting assembly. We use the term casting assembly which consists of the cylinder head and feeder and all the cores attached to the casting when it is placed in the cooling line.

If surface and internal temperature field of casting and cores are known either from measurements or from casting simulations and mass of casting and all of its attachments are known as well and finally specific heat of these are also available, then heat content of casting assembly can be calculated according to *Equation (1)*. For the sake of demonstration let us suppose that a casting assembly (cylinder head and feeder) containing 33.2 kg metal should be cooled from an averaged 530 °C to 80 °C. Heat content of the casting to be removed during cooling process is 18 MJ.

It can be noted that determination of heat content of casting assembly could be started from the heat energy required to melt a 33.2 kg mass of metal as well. While making these calculations one must bear in mind the heat energy to heat the given mass to 700 °C and the latent heat of phase change from solid to fluid must also be added.

The molten metal having the heat content calculated with the above described method is poured into the die cavity where this heat is decreased by many factors. Among these factors are the latent heat of solidification (of that given external layer of the casting that solidifies while in the die) driven by cooling of die and some heat goes into sand cores by conduction. This complex geometry having a complex temperature field at the surface and internally, built from materials having different thermal conductivity and specific heat is placed into the cooling line.

Since the casting assembly contains several sand cores in- and outside of the casting while in the cooling process, heat content of these should also be extracted by the cooling line. In case of some casting assemblies specific parts of the sand cores are either deliberately removed by breaking them off the casting, or because resin burns out of them they fall by themselves. These sand pieces together with their heat content leave the cooling line and thus their heat content should not be handled by the cooling process any more.

As it can be seen by now, heat transfer from 700 °C molten metal is influenced by many (sometimes unknown) factors, so within the limit of this article we carry on with using measured data that metallic parts of the casting assembly have 530 °C temperature when forced cooling starts.

Based on the above the heat content of the casting assembly to be removed by the cooling line is 18 MJ. On the other arm of the balance there is the heat removal capacity of the cooling line, which capacity is influenced by the elements of *Equation (2).* Some of these elements can be influenced by the designer or the operator of the cooling line.

3. INFLUENCING HEAT REMOVAL CAPACITY

Equation (2) has three parts, let us take a look at all of them to see what influence the designer has on them. The temperature part, expressing the difference between wall and cooling medium has an ever decreasing influence since temperature of wall has to decrease as cooling goes on while temperature of cooling medium tends to be constant, thus their difference decreases continuously playing less and less part in the multiplication.

The "F" part of *Equation (2)* is constant again, since outer surface of the casting cannot be changed during cooling unless some more sand covering metal parts break away from the assembly and expose a bigger surface of the casting or the feeder.

The only part of *Equation (2)* the designer or operator has an influence on is heat transfer coefficient (alpha, α), actually it is the only factor the designer of cooling technology has full influence on.

What are the features upon which heat transfer coefficient depends? If water cooling or dry ice provide too much of cooling intensity for our aims, air-based cooling is the choice, so its heat transfer depends on air velocity near the hot wall. But it also depends on flow features of air near the wall, meaning how turbulent airflow is, how fast it picks up heat and how fast it is driven away to carry heat with it.

Of course material properties of air have influence as well. The biggest challenge connected to heat transfer coefficient is that it is hard to measure, outer contour of a cylinder head is very complex and along this contour alpha could change within a significant range. But to design cooling technology heat transfer coefficient must be known.

Table 1 presents [1] heat transfer coefficient ranges in general achievable by gas and fluid flows, so these values are good enough for information only. From heat transfer point of view the fastest cooling applicable to foundry environment can be reached if hot casting is placed in a water tank which is a regular procedure after high temperature stage of T6 heat treatment.

But if freshly cast cylinder heads dropped in water right after being removed from die, cooling results in way too small elongation, not good for our purposes in order to avoid further heat treatment of the workpiece. The cooling technology must be found that is efficiently able to fulfill cooling in a given time (not 3 minutes in our case but 80–90 minutes) while all mechanical parameters of the finished product pass customer requirements. To achieve this, heat transfer coefficient must be accurately known.

Table 1

Ranges of heat transfer coefficient for several gas and fluid flow velocities [2]

Air, gases with natural convection	5–20 W/m^{2}K
Air, slow forced flow	20–50 W/m^{2}K
Air strong forced flow	50–250 W/m^{2}K
Overheated steam	23–116 W/m^{2}K
Water with natural convection	250–2000 W/m^{2}K
Water forced flow	2000–8000 W/m^{2}K
Boiling water	3000–6000 W/m^{2}K
Condensing steam	5000–15000 W/m^{2}K

At this point the importance and usefulness of fluid dynamics simulations come into the picture. In this virtual laboratory created by the computer and the simulation software tool together 3D models of cooling lines can be built on which heat transfer features between casting and cooling agent and geometry variations of casting and cooling nozzle positions can be examined.

We can quantify the effect of an air nozzle being closer or away from the casting. The effect of nozzle position compared to the complex surfaces of castings can be judged. It can be also calculated by how much heat transfer coefficient is increased if ventilator capacity is increased by 50% (be aware that it will be much less than 50%). Different shapes of cooling nozzles can be compared and based on quantified results a design decision can be made.

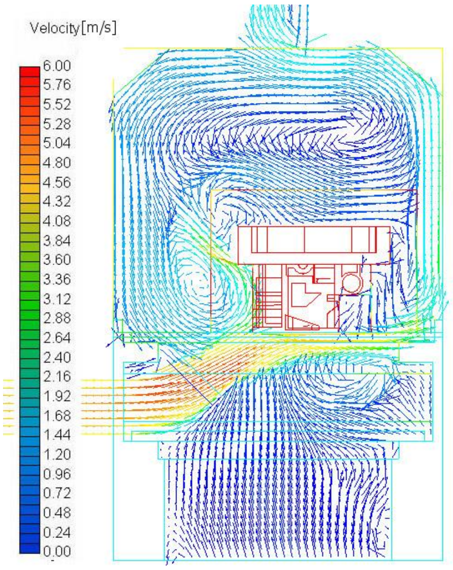

Figure 1

Velocity vectors around a casting and in its close circumference

Figure 1 and *2* show two examples of how complex a flow field around a single or multiple castings can be inside a cooling channel. In both cases the cylinder head assembly is cooled by dry air, coming from a nozzle. Each casing has one dedicated nozzle, in figure 1. this nozzle is cylindrical, for the cooling line on *Figure 2* nozzles have rectangular cross-section.

Among many valuable data such a numerical model can present in terms of efficient heat transfer, alpha distribution along casting surfaces is the most important one, as it can be seen on *Figure 3*. Heat transfer coefficient values can either be used and substituted into *Equation (2)* surface group by surface group, or the distribution can be averaged on the whole surface of the cylinder head assembly and used in *Equation (2)* this way.

The simulation software tool is also capable of calculating heat flux from cooled surfaces, the final result of *Equation (2)* at once. This is the way to go if several geometry versions are calculated during design process or instead of dry air cooling water spray is injected in the stream of cooling air.

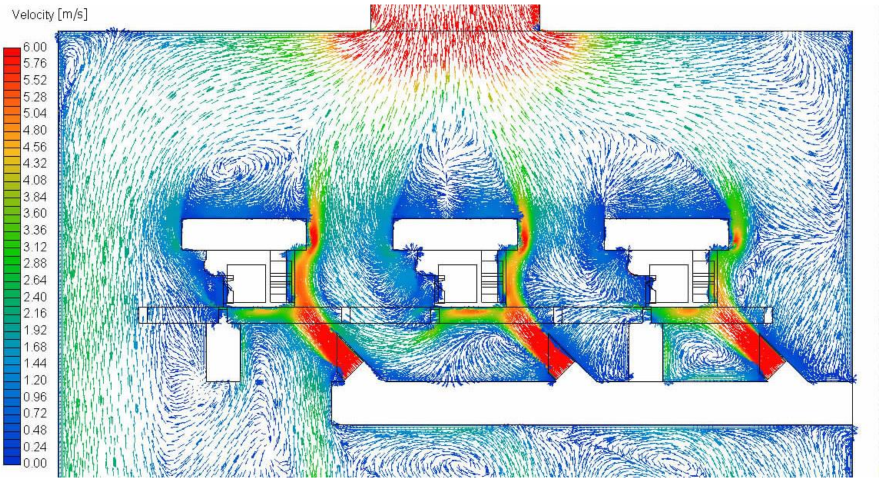

Figure 2
Velocity vectors around three castings placed in a high capacity cooling line

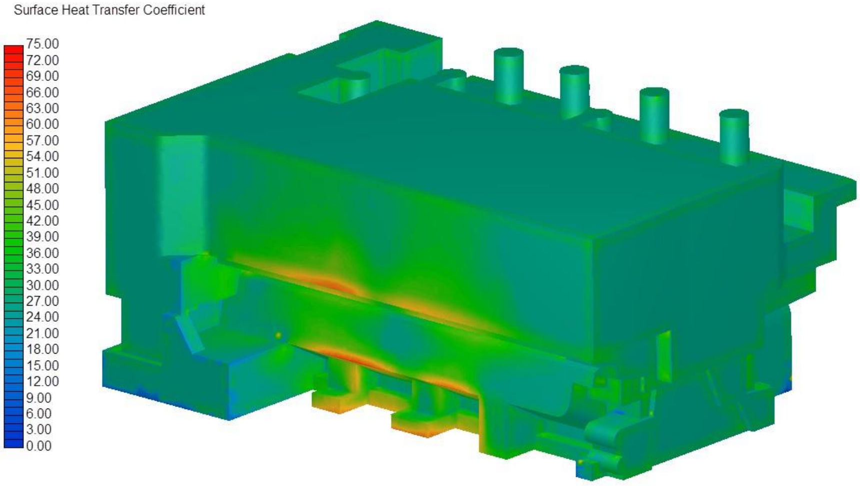

Figure 3a
Distribution of heat transfer coefficient [W/m^{2}K] on side and top surfaces of casting assembly

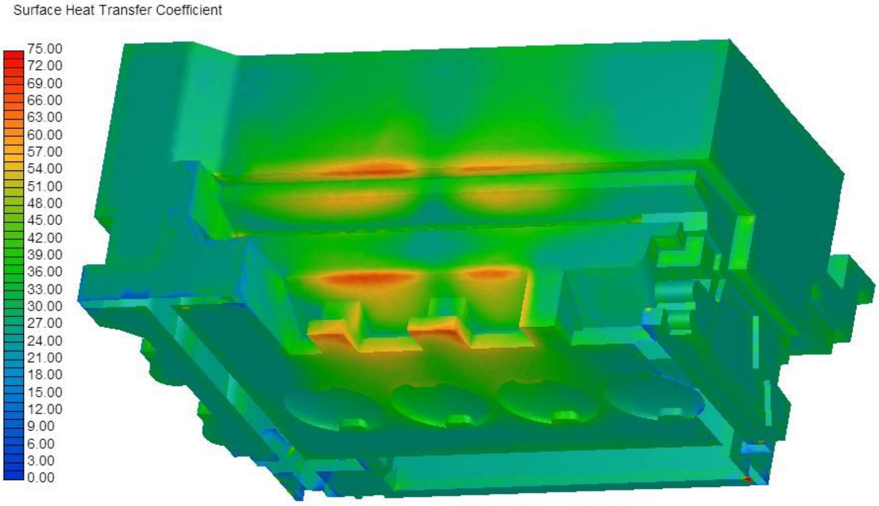

Figure 3b

Distribution of heat transfer coefficient [W/m^2K] on side and bottom surfaces of casting assembly

Based on the information above, simulation provides vital data for setting up the design of a cooling line, but the same is true for a heat treating furnace as well. From the point when simulation is completed for the whole length of the cooling process and heat flux throughout the time frame available for the cooling is calculated, providing the result of *Equation (2)*, this figure can be compared with the result of *Equation (1)*, the heat content of the casting assembly.

It becomes immediately clear if the designed cooling process is able to take at least the amount of heat content stored in the casting assembly. If heat flux is larger than heat content we can rest assure the casting will come out of the cooling line on or below the required 80 °C. At this point if excess heat removal capacity is too much, the designer may think about how to make the system more efficient with a smaller ventilator, or with an other air nozzle shape or arrangement.

In case results are not satisfactory, meaning that heat flux is smaller than heat content, then we need to get back to a previous stage of the design process and either try to reduce heat content (by braking some part of the topcore off the casting, as an example, which is good for the surface size through which heat can be removed as well) or increase efficiency of heat transfer.

This can be done by either decreasing temperature of cooling medium, which could be very costly, or take a look at alpha and increase it over the surfaces of casting assembly. This latter one is much easier than any other method because the first step usually is to increase velocity of cooling air, resulting higher nozzle speed without changing the geometrical arrangement.

In the majority of cases increasing speed of cooling air at the casting solves the lack of heat flux but as it was mentioned above we can not expect linear correlation between increasing air velocity and increasing heat transfer coefficient. Several cases prove that 50%

of ventilator flow rate increase only resulted in 10–12% increase in average heat transfer coefficient.

In such cases designer and cooling line operator could consider increasing heat flux by introducing evaporation into the heat flux by installing water vapour nozzles and injecting small water droplets into the main airstream. By the help of latent heat taken from the casting surface and absorbed by the evaporating water the efficiency of removing heat can be significantly increased assuring that heat flux becomes larger than heat content of the casting assembly.

All of the above can be and should be tested in a computer driven virtual laboratory without the need of welding one piece of steel to the other. After this process is done, only the best performing cooling method needs to be tested before an investment into a cooling line is made. This simulation aided design method is proven to be effective and cheap. Cheaper than building something that does not work, anyway.

REFERENCES

[1] Users' Guide SC/Tetra v13. Software CRADLE Co. Japan, 2017.

[2] *Négyjegyű függvénytáblázatok, összefüggések, adatok.* Budapest, 2005. Nemzeti Tankönyvkiadó, 2. javított kiadás.

Materials Science and Engineering, Volume 42, No. 1 (2017), pp. 36–45.

EASY TO USE TAILORED AUTOMATIC DATA LOGGER DESING USING MICROCONTROLLERS IN A TWO-STAGE GASIFICATION EXPERIMENT

ANDRÁS ARNOLD KÁLLAY[1]–VIVIEN VINCZE[2]–GÁBOR NAGY[3]

Microcontrollers have been around for almost five decades now. They have been and are still used in almost every consumer electronics since their first appearances in the calculator war of the 70's and 80's between the biggest names in electronics. However, their use was limited as their programming language was difficult and one had to be an expert in electronics and had to spend a large amount of funds just for basic programming equipment. Their cost and accessibility overcame their advantages for use in prototyping and research. In the last decade though, a platform emerged, with all the key features needed to make it popular and accessible. It is easy to program, accessible and very low priced. One of the most popular of these microcontroller boards are the Arduinos. In this paper, a working example of the implementation in our two-stage pyrolysis experiment will be presented discussing in detail the hardware and the software setup.

Keywords: data logger, microcontroller, Arduino, automatization

INTRODUCTION

Data logging is essential in every experiment of every single research branch. Besides making the process easier, automatization of data logging also speeds up the measurements. With a faster measurement, more frequent measurements can be made throughout the experiment. Thus, a more detailed dataset can be logged at the end of the experiment. The details of the current experiment are presented in the papers The analysis of the solid and liquid phase products of two-stage pyrolysis *The analysis of the solid and liquid phase products of two-stage pyrolysis* and *Two-stage pyrolysis of Hungarian brown coal to reduce hydrocarbons within synthesis gas*. The temperature of an experiment can have a profound effect on the synthesis gas produced during pyrolysis and gasification [1–3]. To precisely follow the processes taking place in the two-stage gasification experiment, the temperatures had to be measured in six different places of the two furnaces used in the experiment. This setup is also required in order to separate the high from the low temperature processes and assure that heat is not transferred from one process to the other. The experiment itself, including the low and high temperature pyrolysis, is usually no longer then a few hours. However, the temperature must be recorded frequently as the temperature can reach a heating rate of 20 ºC/min. There are commercially available solutions for temperature logging. The YTC YC-74UD Data

---

[1] University of Miskolc, Department of Combustion Technology and Thermal Energy
Miskolc-Egyetemváros 3515, Hungary
tuzaak@uni-miskolc.hu

[2] University of Miskolc, Department of Combustion Technology and Thermal Energy
Miskolc-Egyetemváros 3515, Hungary

[3] University of Miskolc, Department of Combustion Technology and Thermal Energy
Miskolc-Egyetemváros 3515, Hungary

logger thermometer as an example, which is capable of measuring temperatures from four different thermocouples and has an on-board memory to log the measurements [4].

These tools are relatively expensive and their use is rather cumbersome as it needs special cable and software to acquire the logged data. However, in the last decade a series microcontrollers have gained popularity with their user-friendly programming interface and a wide variety of sensor breakout boards that can be customised to fit the requirements of the users. In our case, this was temperature measurement from 6 thermocouples, real time data displaying and logging to a more commonly available and used data storage device. These series of microcontroller boards are commercially known as Arduinos [5], their board is based around *Atmel AVR microcontrollers* [6], their programing language is based on *Wiring* [7] and their software is based on *Processing* [8]. All these mean that the microcontroller boards are inexpensive, as they are open source and can be purchased with no licence fee. Therefore, they can be acquired through online web shops directly from the Chinese manufacturers for prices that often cost less delivered, than their domestic shipment would cost in Hungary.

Their developed software (Arduino IDE [9]) is cross-platform that works on all major operating systems, and has a simple and clear programming environment. Easy to use for beginners but flexible enough for more advanced users. The software is also extensible, the language is expanded through C++ libraries which is a key feature and also the reason it gained such high popularity over the years. Almost every single sensor breakout board that is available has a library written for it and the data can be acquired with a few simple lines of codes within the IDE. In this paper, the data logger we created for our research will be presented as an example to demonstrate how easily automated data logging microcontrollers can be used in your project. The data logger can easily be extended, modified and tailored as the research progresses. Therefore it is also useful for speeding up the process of the development.

1. MATERIALS AND METHODS

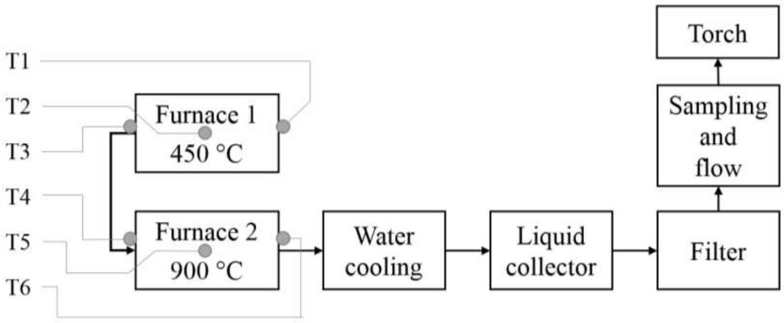

Figure 1
The schematic of the furnace setup for the gasification experiment, grey spots marking the temperature measurement points

The experiment was set up using two tube furnaces, in which the temperature was measured at the entry points of the heat resistant steel pipes placed inside the furnaces and halfway between the two entry points inside the furnace, as it is shown in the schematics on *Figure 1*.

The thermocouples used in the experiments are K-type thermocouples with MAX6675 modules. To display the temperature measurement in real time a 5110 LCD module was used with SPI protocol. The temperature data was logged with a MicroSD Card Adapter board. The microcontroller board used in this experiment was an Arduino Pro Mini with 5V logic level and an Atmel Atmega328P, 16MHz microcontroller. The components were placed on a prototyping board and the connection soldered to place as it is shown in the schematic, the details of the schematic and the placement will be detailed in the "Results and discussion" section of the paper.

2. RESULTS AND DISCUSSION

The discussion of the results will be sectioned in two parts, the first part describing the hardware. In the hardware section the potentials behind of this platform and their use in other data logging and capability to fulfil unique needs of individual research areas will also be discussed. The second part will discuss the software written for this experiment and details of how it can be expanded to other measurements and automated controlling, and finally an example of the measured data set will be presented.

2.1. Hardware setup for the data logger

The main controller used in this experiment for data logging is an Arduino Pro Mini using the Atmel Atmega328P microcontroller. There are many variation of microcontroller boards, differing in size, I/O pin numbers and features. One must consider the amount of data that has to be measured and/or the number of outputs that must be controlled to choose a microcontroller with the required number I/O pins and memory. Every single expansion board comes with its own specific chip and the required components installed on its own breakout-board, the user is only required to connect the wires according to the schematics of the board and upload the example code which is usually provided as a download.

The communication between the breakout-boards (board containing the microchip and the passive electric components) and the microcontroller are achieved through SPI or I^2C protocols in case of more advanced boards as a display, clock module, micro SD card board and libraries, as their implementation is also provided. The input from the switches can be read through digital inputs as high (5 volts) or low (ground, 0 volts). The analogue sensors can be read through the analogue inputs of the microcontroller, with signals between 0 and 5 volts with a 10-Bit resolution (1024 steps). Relays, switches or other modules can be controlled through the digital outputs of the microcontroller, either driving the pins of the Arduino high (5 volts) or low (ground, 0 volts,) or through a PWM signal with an average voltage between 0 and 5 volts and with an 8-Bit resolution (256 steps). To read or write analogue signals with resolutions higher than those provided by the microcontroller, ADC and DAC breakout-boards are also available.

Our requirements were 6 temperature measurements realised through K-type thermocouples and MAX6675 breakout-boards, a MicroSD Card Adapter and display attached to show the real-time temperature measurements, in this case a 5110 LCD display *(Figure 2)*. The microcontroller chosen for the data logger is and Arduino Pro Mini as it has the required number of input and output pins, the required amount of memory and it can be mounted on a prototyping board due to its small size. All chosen parts for the data logger communicate with the microcontroller through SPI protocol which communicates with 4 wires in a master-slave configuration. Two wires are used for the data communication: master in slave out (MISO), master out slave in (MOSI), serial clock (SCLK) and slave select (SS). One of the main advantages of the SPI communication is that if more than one slave is required, as in our case for the temperature sensors for each additional device, only one additional wire (SS) is required, the other wires can be shared between the devices. A disadvantage of this protocol is that more than one clock signal triggers exist (different polarity and phase) for data transmission depending on the used protocol. From the user's point of view this means that while the same type of sensors, displays or other modules can share the same MOSI, MISO and SCLK wires, others can vary. This is the reason behind the three different SPI bus generated for our data logger, which can be seen on *Figure 3*. The MAX6675 sensor board shares the same data out lines (DO same as MISO), SCK lines and the power lines and has separate pins set up for the chip select lines (CS same as SS). For the LCD, another SPI bus was generated with all the pins required and for the micro SD card adapter as well. In addition to the SPI lines, a toggle switch and an LED were implemented in the circuit as well, for turning on the data writing and a visual confirmation if the temperature data writing has started on to the micro SD card.

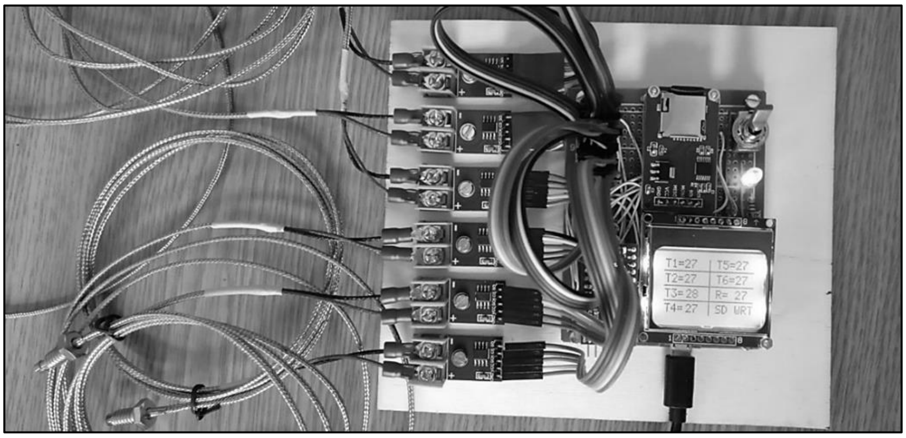

Figure 2
The temperature data logger fully wired, with the K-type thermocouples attached to the MAX6675 sensor boards

2.2. Software for the temperature data logger

The Arduino software environment (Arduino IDE) can be downloaded from the developers' page [9] as a free download and is available for the most popular operating systems, including Windows, Mac OS and Linux. The Arduino environment is written in Java and based on processing and other open-source software. After the software is installed, the required libraries for each breakout board must installed in the Arduino's library folder. The software written within the Arduino IDE is called sketch. After the sketch has been written, it can be uploaded to the microcontroller board through USB cable or, in the case of the Arduino Pro Mini, using USB to Serial converter board. The written sketch is translated to machine language by the Arduino software and after uploading, the uploaded sketch is ran by the microcontroller continuously.

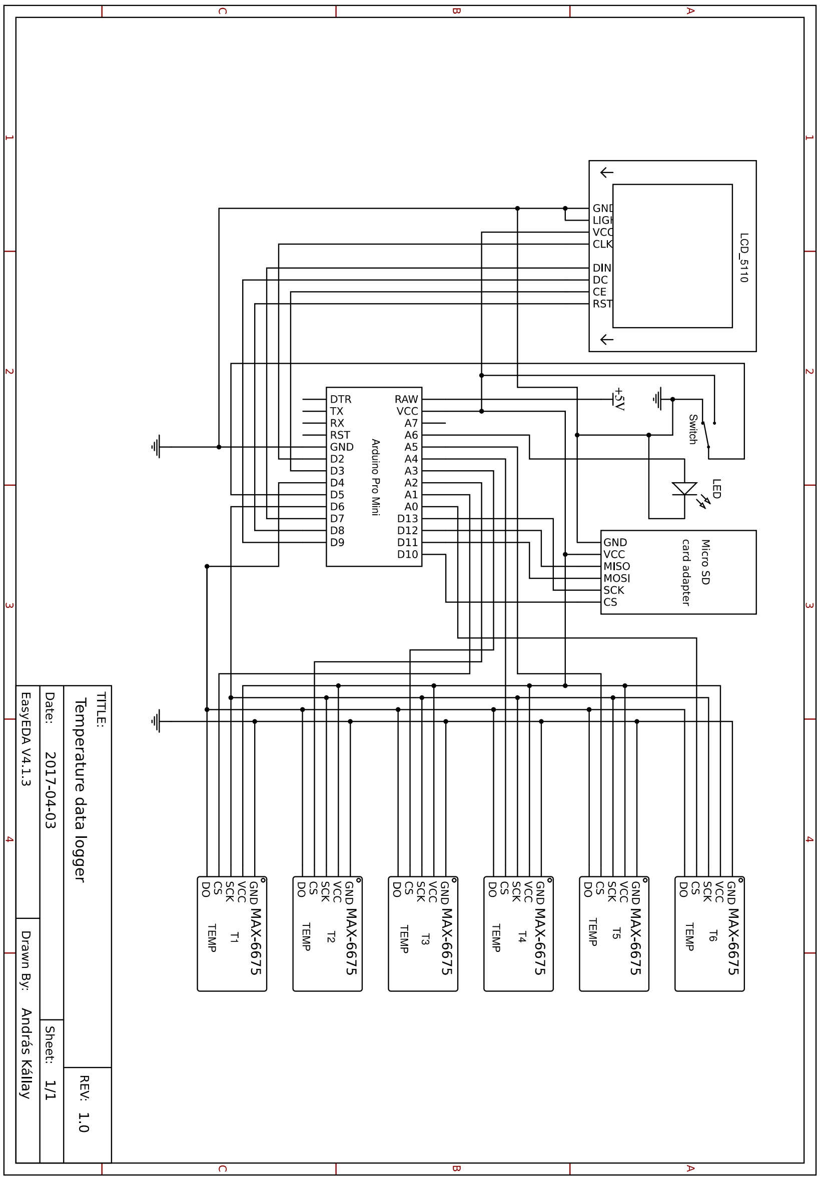

Figure 3

Schematic of the temperature data logger wiring diagram

The sketch is usually divided to two sections. The first is the setup section and the second is the loop section. The inclusion of the libraries required, the declaration of the variables and constants and the assignment of the pin function are contained by the setup section of the code.

All codes presented in this paper are shown as they appear in the written sketch for the temperature data logger in the Arduino IDE, broken down into smaller segments for the comfortable explanation and reading. In our temperature data logger sketch, the included libraries *(Sketch segment 1)* for the three types of boards used in our setup are contained in the first part.

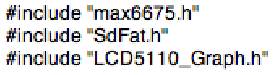

```
#include "max6675.h"
#include "SdFat.h"
#include "LCD5110_Graph.h"
```

Sketch segment 1
Code written for the inclusion of libraries required

The inclusion of libraries is followed by the assignment of the pins for each board *(Sketch segment 2)*. The text written after the double slash signs are comment placed by the writer of the sketch. The assignment of each pins for the "SdFat" library is predefined, except for the chip select (SS) pin that can be changed by the user. The pins of the other two boards are arbitrarily chosen by the user and placed within the code as it is shown in the example. In addition to the assignment of pins, the font is also assigned in this section for the LCD. The following lines of code *(Sketch segment 3)* contain the assignment of the pins for the LED and the toggle switch, as well as the initialisation of the "millis" function that is necessary to be able to measure the time, and the micro SD card file name. Next is the "void setup" part of the code where the LCD and the micro SD card are initiated *(Sketch segment 4)*.

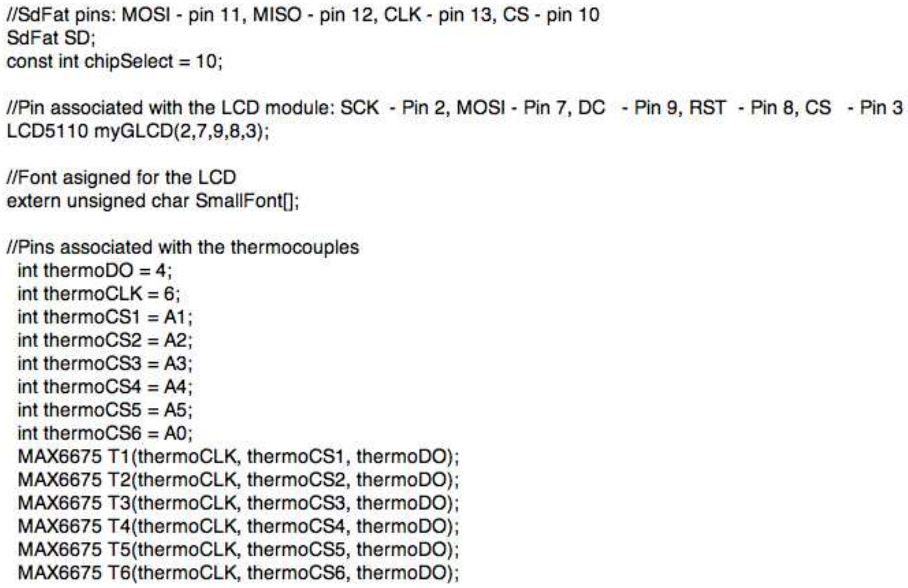

```
//SdFat pins: MOSI - pin 11, MISO - pin 12, CLK - pin 13, CS - pin 10
SdFat SD;
const int chipSelect = 10;

//Pin associated with the LCD module: SCK  - Pin 2, MOSI - Pin 7, DC   - Pin 9, RST  - Pin 8, CS   - Pin 3
LCD5110 myGLCD(2,7,9,8,3);

//Font asigned for the LCD
extern unsigned char SmallFont[];

//Pins associated with the thermocouples
  int thermoDO = 4;
  int thermoCLK = 6;
  int thermoCS1 = A1;
  int thermoCS2 = A2;
  int thermoCS3 = A3;
  int thermoCS4 = A4;
  int thermoCS5 = A5;
  int thermoCS6 = A0;
  MAX6675 T1(thermoCLK, thermoCS1, thermoDO);
  MAX6675 T2(thermoCLK, thermoCS2, thermoDO);
  MAX6675 T3(thermoCLK, thermoCS3, thermoDO);
  MAX6675 T4(thermoCLK, thermoCS4, thermoDO);
  MAX6675 T5(thermoCLK, thermoCS5, thermoDO);
  MAX6675 T6(thermoCLK, thermoCS6, thermoDO);
```

Sketch segment 2
Code for the assignment of the pins to the breakout-boards

After the setup section of the sketch is followed by the loop section. In the loop section of the sketch, the code that will cycle through the microcontroller after the upload is contained. The microcontroller follows the code line by line and the task in the code are performed. The setup of the LCD screen, divided into separate sections, for the six temperature measurement data and the micro SD card state *(Sketch segment 5)* are contained in the first part of the code. The insertion of the data read from the sensors in each segment set up on the LCD is also included in the command.

```
//Initialising switch and led pins and state of the switch
  int Switch = 5;
  int SwitchState = 0;
  int LedPin = A6;

//Millis fucntion required for time measurement
  unsigned long previousMillis = 0;
  unsigned long interval = 100;

//File name decalration for the SD card
  File TimeFile;
```

Sketch segment 3

Code for the initialisation of the switch, LED, time and micro SD card functions.

```
void setup() {

  pinMode(Switch, INPUT);
  pinMode(LedPin, OUTPUT);
  SD.begin(chipSelect);

  myGLCD.InitLCD();
  myGLCD.setFont(SmallFont);
}
```

Sketch segment 4

Code written for “void setup”

```
//Main loop
void loop() {

//Setup LCD to show if the SD card has initialized correctly(if yes = ON, if not= OFF)
  myGLCD.clrScr();
  if (!SD.begin(chipSelect)) {
  myGLCD.clrScr();
  myGLCD.print("SD OFF", 48, 36);
  }
  else{
  myGLCD.print("SD ON", 48, 36);
  }

//LCD setup for alignment of the grid and displaying the read thermocouples and flowmeter data
  myGLCD.drawLine(42,0,42,45);

  myGLCD.print("T1=", LEFT, 0);
  myGLCD.printNumF(T1.readCelsius(), 0, 18, 0);
  myGLCD.drawLine(0,9,84,9);

  myGLCD.print("T2=", LEFT, 12);
  myGLCD.printNumF(T2.readCelsius(), 0, 18, 12);
  myGLCD.drawLine(0,21,84,21);

  myGLCD.print("T3=",LEFT, 24);
  myGLCD.printNumF(T3.readCelsius(), 0, 20, 24);
  myGLCD.drawLine(0,33,84,33);

  myGLCD.print("T4=", LEFT, 36);
  myGLCD.printNumF(T4.readCelsius(), 0, 20, 36);

  myGLCD.print("T5=", 48, 0);
  myGLCD.printNumF(T5.readCelsius(), 0, 66, 0);
  myGLCD.drawLine(0,9,84,9);

  myGLCD.print("T6=", 48, 12);
  myGLCD.printNumF(T6.readCelsius(), 0, 66 , 12);
  myGLCD.drawLine(0,21,84,21);
```

Sketch segment 5

Code for the LCD setup

The micro SD card adapter is set up with a condition statement *(Sketch segment 6)*. The function of the condition statement, the writing function, can be turned on with an input from the user, in our case with a toggle switch. In addition to this functionality, the availability of the micro SD card is also checked, if it has been inserted and it can be successfully written in the file defined in the sketch. The file produced by the code is a text file saved on the micro SD card. The temperature values from each sensor are written in the same line, including a time stamp from the “millis” function. If the data writing is successful, the wired led is lit up and the LCD screen presents a “WRT” status in the section of the SD card state defined in the LCD section. If the card is not inserted, the card state section of the SD card shows “OFF” as a written feedback. If the SD card is inserted but the toggle switch is not in the writing position, the “ON” written feedback is shown on the LCD’s SD card state section. In the last part of the loop section, the LCD is refreshed and a delay of 1000 milliseconds is inserted before the loop section starts again.

```
//setup of the switch to start the data logging in the SD card
  SwitchState = digitalRead(Switch);
    if (SwitchState == HIGH){
      unsigned long currentMillis = millis(); //millis function for time stamping the logged data
      if (currentMillis - previousMillis >= interval){
        previousMillis = currentMillis;
        TimeFile = SD.open("DATALOG.txt", FILE_WRITE);//creating file on the SD card
        if (TimeFile) {
          myGLCD.print("SD WRT", 48, 36); //displaying if the file opened succesfully
          analogWrite(LedPin, 255);     //indicating the file opening with a LED
          TimeFile.print(currentMillis/1000);
          TimeFile.print(", ");
          TimeFile.print(T1.readCelsius());
          TimeFile.print(", ");
          TimeFile.print(T2.readCelsius());
          TimeFile.print(", ");
          TimeFile.print(T3.readCelsius());
          TimeFile.print(", ");
          TimeFile.print(T4.readCelsius());
          TimeFile.print(", ");
          TimeFile.print(T5.readCelsius());
          TimeFile.print(", ");
          TimeFile.println(T6.readCelsius());
          //TimeFile.print(", ");
          //TimeFile.println(R6.readCelsius());
          TimeFile.close();
        }
      }
    }
   else {                    //turning of the LED if the data logging is switched off.
        digitalWrite(LedPin, LOW);
        }
    myGLCD.update(); //neceseary refres of the LCD

    delay(1000);
}
```

Sketch segment 6
The micro SD card loop section

2.3. Experiment using the data logger

With the sketch setup presented, the loop runs in every second and returns the temperature measured with the K-type thermocouples. The measured data is presented in real time on the LCD and if the data logging is turned on, a file is created and the data is also written to a text file at every second of the experiment. Each line of the text file contains a time stamp and the 6 temperatures registered by the MAX6675 sensors, separated with commas. The text file can be easily imported in to MS excel data sheets, from where it can be further processed as desired. The data logging speed presented here is limited by the delay and it is obvious that it can be increased and decreased if necessary. In our case, the temperature logged every second is more than the required data.

Using the described hardware setup and software, the exact temperatures of the various data logging points could be measured automatically using the data logger, the result of which can be seen in *Figure 4*. The presented experiment was 95 minutes long. Increasing temperatures can be observed on the presented figure up to the 95-minute period point, when the furnace was turned off, after which the furnace temperatures started to decrease as the furnace continuously cooled down.

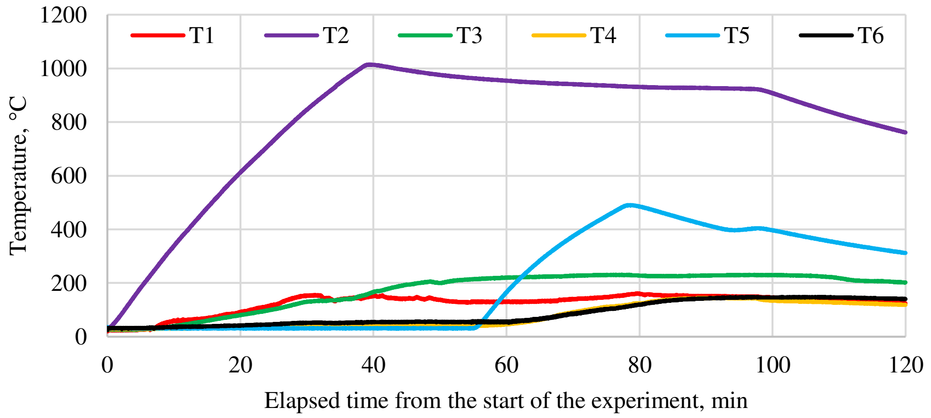

Figure 4
Temperatures collected by the data-logging system during an experiment

CONCLUSION

A temperature data logger setup has been presented, controlled by a microcontroller registering temperatures and with data rate speed set up by the user within the sketch running on the microcontroller. Setting up the hardware is relatively easy following this paper with step by step description, and connecting the right pins on the microcontroller to the appropriate pins on the breakout boards of the sensor. The written sketch is built up from the examples provided with the libraries of the breakout boards and are just pieced together. With this setup, the temperature data logger can show real time temperature measurements on an LCD screen and create a text file on a micro SD card with the data being registered every second with comma separated values. The text files created can be further processed in spreadsheet handling applications, like MS Excel. Furthermore, the setup can be easily customised to fit special setups, and the whole setup can cost ten times less compared to the commercially available temperature data loggers with just four thermocouple inputs.

To extend the data logger, measuring temperatures from more thermocouples is just a question of attaching more MAX6675 breakout boards to the microcontroller and including them in the sketch. If more input pins are required, there are larger microcontroller boards available. To increase or decrease the frequency of the measurement, a simple adjustment is needed in the sketch written. As almost every commercial sensor for data measurement, an analogue output or input function that operates at 5V logic level is included. The data sent by the sensor can be read, registered, displayed, converted by the microcontroller, while the analogue and digital write functions of the microcontrollers allow precise control of motors, controllers, relays and solid state switches operating high powered applications, etc. For higher resolution, analogue read/write function breakout boards are also available. The opportunities opened by this microcontroller platform are almost endless and including it in our research has undeniable advantages in the measurements and controlling of the experiments.

ACKNOWLEDGEMENT

The authors are grateful to Mária Ambrus for her advice.

REFERENCES

[1] WANG, Q.H.–ZHANG, R.–LUO, Zy Y.–FANG, M. X. –CEN, K. F.: Effects of Pyrolysis Atmosphere and Temperature on Coal Char Characteristics and Gasification Reactivity. *Energy Technology,* Vol. 4, Issue 4 (2016), 543–550.

[2] ZHANG, H.X.–GUO, X.W.–ZHU, Z.P.: Effect of temperature on gasification performance and sodium transformation of Zhundong coal. *Fuel*, Vol. 189 (2017), 301–311.

[3] BEHNIA, I.–YUAN, Z. S.–CHARPENTIER, P.–XU, C.B.: Production of methane and hydrogen via supercritical water gasification of renewable glucose at a relatively low temperature: Effects of metal catalysts and supports. *Fuel Processing Technology*, Vol. 143 (2016), 27–34.

[4] Webshop, YC-747UD Hand-held Data Logger 4ch. Thermocouple Thermometer with USB PC Interface. http://www.tmswebshop.co.uk/buy/yc-747ud-hand-held-data-logger-thermometers-with-usb-pc-interface-yc747dlogger.html. (Downloaded 2017. 04. 05.)

[5] Arduino - Home, 2017. https://www.arduino.cc/. (Downloaded 2017. 04. 04.)

[6] Atmel AVR 8-bit and 32-bit Microcontrollers, 2017.
http://www.atmel.com/products/microcontrollers/avr/default.aspx.
(Downloaded 2017. 04. 06.)

[7] BARRAGN: H., Wiring, 2017. http://wiring.org.co/. (Downloaded 2017. 04. 05.)

[8] P. Foundation, Processing.org, 2017. https://processing.org/. (Downloaded 2017. 04. 04.)

[9] Arduino – Software, 2017. https://www.arduino.cc/en/Main/Software.
(Downloaded 2017. 04. 04.)

Materials Science and Engineering, Volume 42, No.1 (2017), pp. 46–58.

THE ANALYSIS OF THE SOLID AND LIQUID PHASE PRODUCTS OF TWO-STAGE PYROLYSIS

ANDRÁS ARNOLD KÁLLAY[1]–VIVIEN VINCZE[2]–
GÁBOR NAGY[3]–TAMÁS KOÓS[4]

During the experiments, the material and energy conversions during the pyrolysis of Hungarian low rank coal at low (450 °C) and high temperatures (900 °C), and the residue char and liquid phase were examined.

Temperature increase results in higher material and energy conversion. Thus, the amount of solid residue decreases and the energy content of the final product is higher. Despite this, char with significant carbon content – and calorific value – is produced during the experiments at 900 °C which may be further utilised.

Keywords: coal gasification, power generation

INTRODUCTION

Coal is among one of the most important fossil fuels and takes up about 75% of all fossil based reserves from the world [1]. Based on 2013 data, research shows that the available fossil fuel reserves would serve the global requirements for more than a century (114 years) with the current consumption rate [2]. Apart from the Asian region, the reserves of Europe and North-America would serve the local consumption for almost three centuries *(Figure 1)*. However, with the ever-increasing consumption of China and India, these estimates are far from that mark point.

On the contrary, coal reserves are decreasing and the consumption rate shows an increasing tendency, particularly in the three major mining countries, namely China, India and Australia [3].

The primary use of coal is in electrical power generation which is followed by iron production, where coke is used as fuel and reducing agent. In 2012, from the total coal share of world energy consumption 43.24% was used in electrical power generation, 25.07% was consumed by the industrial sector, while less the one third was used by the rest.

---

[1] University of Miskolc, Department of Combustion Technology and Thermal Energy
Miskolc-Egyetemváros 3515, Hungary
tuzaak@uni-miskolc.hu

[2] University of Miskolc, Department of Combustion Technology and Thermal Energy
Miskolc-Egyetemváros 3515, Hungary

[3] University of Miskolc, Department of Combustion Technology and Thermal Energy
Miskolc-Egyetemváros 3515, Hungary

[4] University of Miskolc, Department of Combustion Technology and Thermal Energy
Miskolc-Egyetemváros 3515, Hungary

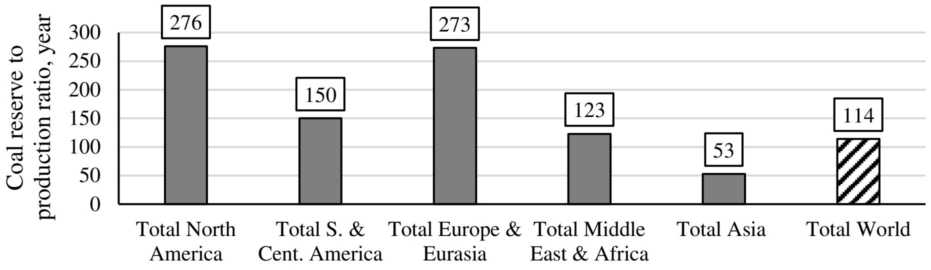

Figure 1
Coal reserves to production ratio (2013) [2]

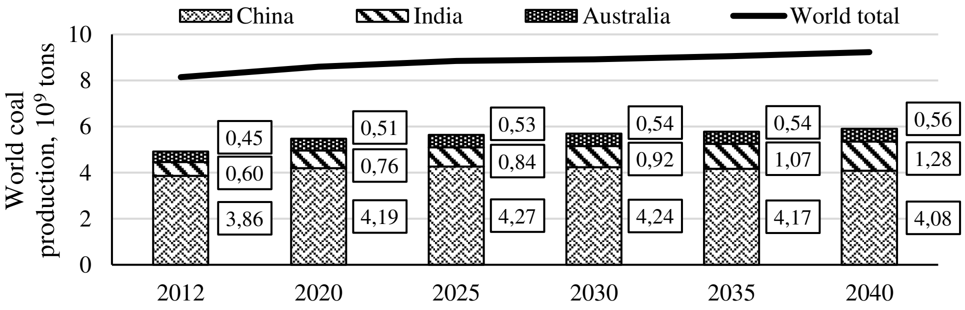

Figure 2
World coal production (2012–2040) [3]

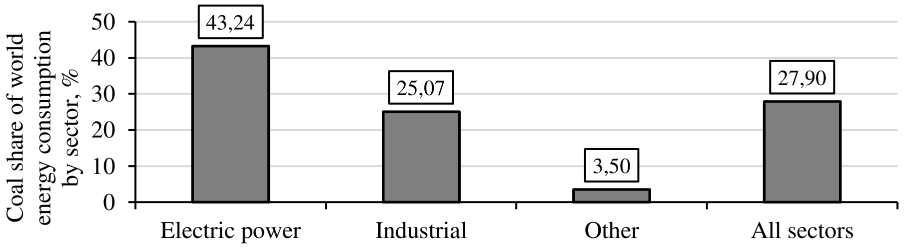

Figure 3
Coal share of world energy consumption by sector (2012) [3]

The primary consumption of coal is based on the release of the chemical energy stored within. As the ratio of the available quantity and the quality of coal reserves are inversely proportional, lower rank coals are often used as base materials to produce char coke in coking procedures. The by-product of the procedure is synthesis gas. A part of the synthesis gas is used in-situ, to supply the energy required by the coking [4]. Coal also serves as a base material in gasification processes where the solid energy source is converted into synthesis gas, that could be used either as a base material in chemical synthetisations or as fuel in power generation. The process of the gasification has several advantages [5-8]:

- through gasification, a more valuable product can be produced that can not only serve as fuel in power generation, but also as a base material for chemical industrial applications;
- carbon dioxide emission rates are lower, even if the synthesis gas is used in power generation applications;
- the sulphur released from coal steam gasification is in form of H_2S rather than SO_2, which can be removed from the synthesis gas and can be used in sulphur and sulphuric acid production, thus, producing a valuable product as a by-product;
- nitrous oxides are primarily converted into ammonia, which can be removed from the synthesis gas at a lower cost;
- emission rates of furan and dioxin are significantly lower compared to the combustion of coal;
- the total volume of gas that has to be cleaned after gasification is lower than that of the combustion.

1. MATERIALS AND METHODS

The low rank brown coal used in the gasification experiment is from the North-East brown coal basin in Hungary. In the series of experiments prepared, the gasification was investigated in a two-stage setup using two furnaces with separate temperature control. Heat resistant steel pipes were used in the experiments as gasifiers, where the two gasifiers were connected through a third steel pipe *(Figure 4)*. The setup allowed an investigation of the pyrolysis divided into two stages where one was set up for a low temperature and the other for a higher temperature pyrolysis. The synthesis gas produced in the lower temperature pyrolysis was routed through the high temperature zone of the setup.

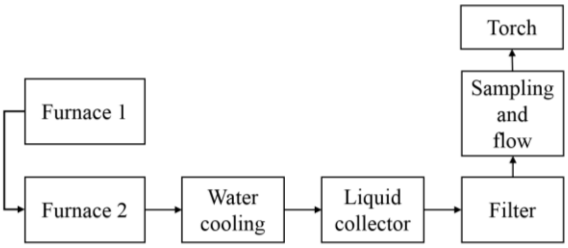

Figure 4
The route of the synthesis gas produced in the two-stage gasification experiment

The base material (low rank brown coal) and the solid phase products were examined with the following analysis techniques:

Moisture contents were analysed with a Mettler Toledo HB43-S type analyser, using the *EN 14774:2009: Solid biofuels. Determination of moisture content – Oven dry method* standard analysis procedures.

Standard *EN 14775:2010: Solid Biofuels – Determination of Ash Content* was used to determine the ash content. The analysis was carried out in a HK-45/12 V type heating furnace with 12 kW nominal power.

The elemental composition of the samples was analysed based on Standard *EN 15104-2011: Solid Biofuels – Determination of Total Content of Carbon, Hydrogen and Nitrogen – Instrumental Methods* with a Carlo Erba EA 1108 elemental analyser. The program Eager 200 was used to collect and analyse the data.

Standard *EN 14918:2009: Solid biofuels – Determination of calorific value* was the basis of the determination of the higher heating value (HHV), using a Parr 6200 type calorimeter, then in the light of certain corrections, i.e. the hydrogen or moisture content of the sample, the lower heating value (LHV) was calculated.

The softening and melting properties of the ash ware analysed with a SYLAB IF2000G type instrument a based on the standard *CEN/TS 15370-1: 2006: Solid biofuels – Method for the determination of ash melting behaviour. Characteristic temperatures method*:

Thermoanalytical measurements were conducted with MOM Q1500D Derivatograph capable of TG-DTG-DTA measurements.

The synthesis gas analysis for the energy conversions is detailed in the article *The Two-Stage Pyrolysis of Hungarian Brown Coal to Reduce Hydrocarbons within Synthesis Gas,* also published in the current issue.

2. RESULTS

2.1. Base material conversion

During pyrolysis, the base material is exposed to heat to release its moisture content and part of its volatile content. Thus, the coal produced has higher carbon content and has better combustion parameters. Part of the moisture and volatile content released during pyrolysis can condense when passing through the cooling system, while the rest of the gas produced is composed of combustible gases like hydrogen, carbon monoxide and methane. Beside the non-condensable gases, carbon dioxide and, in a small volume percentage, hydrocarbons are also produced.

Within the gasification, the main objective beside clean synthesis gas production is the highest rate of conversion with the least amount of carbon retained in the ash and slug. The conversion rate is mostly defined by the temperature of the gasification [9], which can be observed in our investigation as well *(Figure 5).*

The weight loss of the converted base material (low rank brown coal), which was predried at 110 °C, at 450 °C pyrolysis was 17.8%. The same base material at 900 °C pyrolysis shows a weight loss of 30.9%w/w. Most of the base material in the pyrolysis is converted to gas phase while between 2–3.55%w/w is re-condensed in the cooling procedure. The liquid condensed can be separated to two phases. One phase is a dense tar phase, while the other is a thin phase mostly composed of water. The tar phase is about 0.3–0.5% of the base material. The most convenient recycling of this phase is the re-insertion in the gasifier, where it can be further decomposed in the high temperature pyrolysis.

After the pyrolysis, the residual solid phase material still has high carbon content that can transformed through steam gasification to produce synthesis gas or it can be used as a base material in power generation.

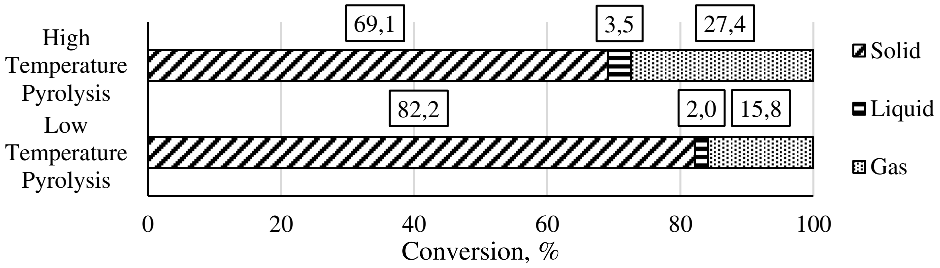

Figure 5
Conversion rate of the base material

2.2. Solid phase analyses

2.2.1. Moisture and ash content

The starting material, low rank brown coal, had a moisture content just below 15%w/w *(Table 1)*. The moisture content was removed in the drying procedure before the experiments, therefore, the produced liquid phase in the pyrolysis can be measured in relation to the dry base material.

The relation between the temperature of the pyrolysis and the residual ash content of the solid phase after the experiments can be revealed by ash content determination. The low temperature pyrolysis slightly increased the ash content ratio to 25.68%w/w, while the high temperature pyrolysis further increased it to 40.70%w/w. This is the expected result of the released volatiles, which are mostly composed of hydrocarbons. Therefore, the initial carbon content of the coal decreases, while having the same amount of ash as the base material.

Table 1
Moisture and ash contents

Moisture content of the base material	14.95%w/w
Ash content of the base material	19.95%w/w
Ash content after the low temperature pyrolysis	25.68%w/w
Ash content after the high temperature pyrolysis	40.70%w/w

2.2.2. Elemental analyses

The low rank brown coal used in the experiments has a carbon content below 50%w/w and an oxygen content of 20%w/w, which is typical for low rank coals *(Figure 6)*. However, the sulphur content is rather increased compared to typical values in these types of coals, which further increases the cost of the removal from the synthesis gas. After the first stage of the experiment, the low temperature pyrolysis (L.T.P.), the elemental analysis showed a decreased elemental content in every element measured apart from sulphur. This can be concluded as an enrichment due to the low temperature pyrolysis, as it results in an increased sulphur ratio. Further increasing the temperature, the elemental contents show a decreasing tendency with the exception of the carbon content. The enrichment of carbon in the resulted solid phase of the high temperature pyrolysis (H.T.P.) can be related to the considerably reduced oxygen content that slows down the char gasification reactions.

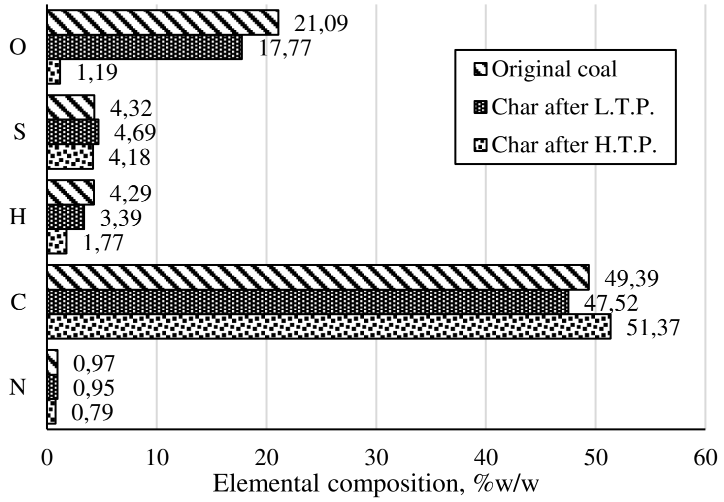

Figure 6

Elemental composition of the analysed materials

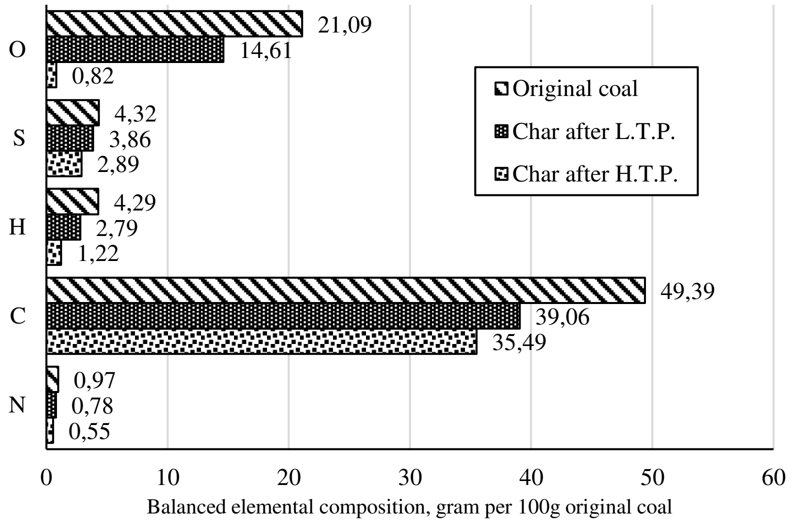

Figure 7

Elemental composition of the base material and the solid residues after the low and high temperature pyrolysis

Further calculations balanced to 100g of the originally introduced base material is used to calculate the amount of each element remained within the residual material after each experiment *(Figure 7)*. It is apparent from the analysis that the amount of oxygen remaining after the low temperature pyrolysis has a significantly higher concentration than that from the high temperature pyrolysis, where the oxygen from the base material is almost completely absent. The sulphur content of the base material, even after the high temperature pyrolysis, is present with 70%w/w of its original quantity. This high amount of sulphur content after the high temperature pyrolysis indicates that brown coal coke is still not the most suitable material for power generation purposes through combustion, as it requires SO_2 removal from the flue gas which significantly decreases its value in this sector. However, it is still a proper base material for both steam gasification and power generation because of the 70%w/w residual carbon content. Due to the quantity of hydrogen after the high temperature pyrolysis, only steam gasification is validated as a route for synthesis gas production.

2.2.3. Thermal analysis

Through thermal analysis the structural composition of the base materials can be derived, which includes the moisture, volatile, char and ash content of the analysed material *(Figure 8)*.

The finely ground materials used in thermal analysis can bind moisture from the environment (3–6%w/w) within a short timeframe, which is evidently visible in *Figure 8*. The combustible carbon (volatile and char) from the base material has a significantly higher volatile to char ratio than the coke from the 900 °C pyrolysis experiment. Even at 900 °C, the thermal analysis suggests 22% volatile content within the coal. However, these results must be handled with care as the measurements are short compared to a pyrolysis experiment and the results can show significant deviations when they are compared to elemental analyses *(Figure 7)* or standard ash content determination procedures *(Figure 9)*. The standard procedure of the ash content determination is achieved by a several-hour-long heat retention compared to that of the derivatograph, which is completed after reaching a certain temperature (1330 °C) of the measurement. The values of the ash content determination are 2–3% higher in every case of the samples and these should be considered as real quantities in the determination.

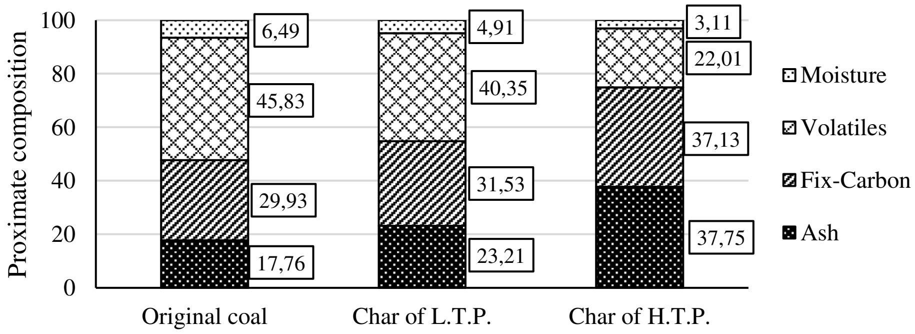

Figure 8
Proximate analysis of the samples

The measurements with the dervivatograph can also give information about the weight loss kinetics of the samples *(Figure 9)*. In all three samples, the weight decreases linearly and slowly, therefore, the interpretation of each separate processes (volatilisation, combustion etc.) are difficult. After time-derivation of the curves and comparing them to the original weight loss curves, the exact interval of each process can be determined. The determined temperature intervals are presented in *Figure 10*.

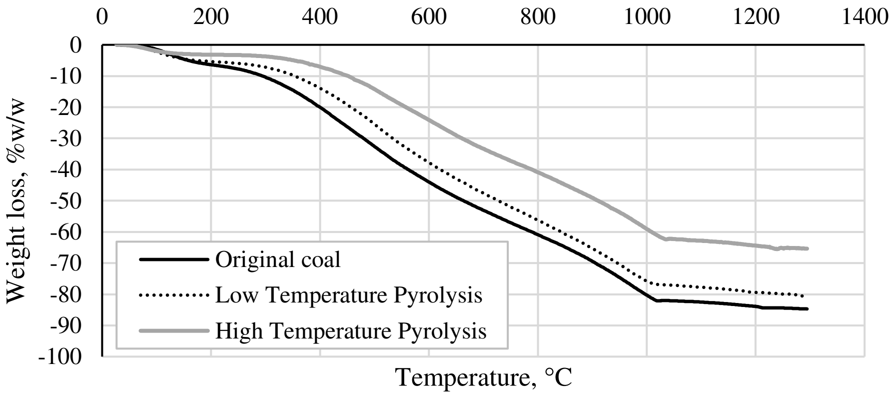

Figure 9
The weight loss of samples with temperature increase

Examining each process, it can be seen that the samples from the base material and the low temperature pyrolysis behaved similarly. The drying, volatilisation and combustion of fixed carbon happened in the same temperature frame. Since the moisture content of the samples are retained through absorption in the preparation phase, it will not be analysed further. If the samples from the base material and the low temperature pyrolysis are compared it can be noticed that the combustion of the volatiles is shifted up in temperature. Therefore, it can be concluded that the easily mobilised light weight hydrocarbons are no longer present in this sample. Examining the typical temperature ranges of the sample from the high temperature pyrolysis it can be seen that the combustion of the volatiles start at the same temperature as well. This suggests that the composition of the released hydrocarbons is similar to that of the low temperature pyrolysis. However, the amount of the released hydrocarbons is lower in the case of former. The lower amount of released hydrocarbons is also supported by the volatilisation temperature interval which, in the case of the sample from the high temperature pyrolysis, is significantly lower. The final temperature of the sample combustions are consistent with the elemental compositions *(Figure 6)*: the higher the carbon content, the higher the final burning temperature is.

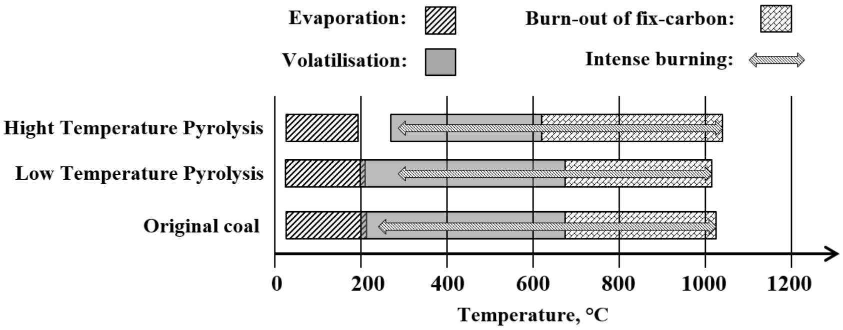

Figure 10
The temperature intervals of each process for the three analysed samples

2.2.4. Heat of combustion and calorific value

The determination of the combustion heat and calorific values *(Table 2)* shows that the base material (pre-dried low rank brown coal) has the highest heat of combustion. The heat of combustion decreases as the pyrolysis temperature increases. Comparing the sample from the base material to the sample from the low temperature pyrolysis, the heat of combustion drops 1%. On the other hand, high temperature pyrolysis shows a drop of 14% compared to the base material. The source of the drop in the heat of combustion is the increased specific ash content for each temperature treatment (pyrolysis). During pyrolysis, the produced coke has less combustible components per weight which results in a higher inert component (ash) per weight. The calorific value of the residual coke after the high temperature pyrolysis still has high energy content, its heat of combustion is comparable to high-quality wood pellets.

Analysing the calorific value of the samples showed higher value for the sample from the low temperature pyrolysis, contrary to the combustion heat values which was only 1% lower. This is the result of the higher hydrogen content of the base material. As it can be seen in the following equitation, the amount of hydrogen within the sample has more dramatic effect on the results calculated:

$$LHV = HHV - 24.493 * (9 * H + W) \; [kJ/kg] \tag{1}$$

where: H – hydrogen content, w%
W – moisture content, w%

Table 2
Heat of combustion and calorific value of the samples

Sample	**Heat of combustion, MJ/kg**	**Calorific value, MJ/kg**
Base material	20.76	19.65
Pyrolysis at 450 °C	20.60	19.73
Pyrolysis at 900 °C	17.95	17.48

2.2.5. Ash softening analysis

The ash softening temperature of the base material is essential in the design phase of the experiment, regarding the gasifier and the furnace properties. Our experiment was planned to be carried out at 900 °C. Still, taking into account the inertia of the furnace and the later planned gasification medium, in which partial oxidation reactions can occur, the temperature can swing up to 200–300 °C in certain zones of the gasification.

Because of the temperature increase, the deformation of the test bars prepared from the ash based on standard *CEN/TS 15370-1: 2006* can be characterised with the following 5 states/temperatures *(Figure 11.)*:

1) Original sample;
2) Shrinkage starting temperature: the area of the test bar decreases by 5 % because of sintering, the departure of CO_2 and/or volatile alkaline metals;
3) Deformation temperature: the temperature at which the softening of the test bar seems to start, i.e. the surface is changing, the edges are getting rounded, the test bar is starting to swell. The starting temperature of the softening;

4) Hemisphere temperature: the temperature at which the shape of the test bar resembles a hemisphere. The height of the molten test bar is the half of its diameter;
5) Flow temperature: the temperature at which the height of the test bar is the half of the height measured at hemisphere temperature.

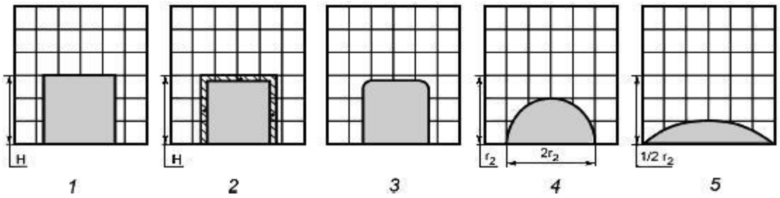

Figure 11
Phases in the ash melting process [11]
1) Original sample; 2) Shrinkage; 3) Deformation; 4) Hemisphere; 5) Flow

The shrinkage of ash from the low rank brown coal used in our experiment starts at 1108 °C and the deformation takes place at 1257 °C. This temperature range is within the temperature zone of our experiment. In case of incidental occurrences of temperature swings, this can cause clogging if the softened ash sticks to the wall of the gasifier. Therefore, the close tracking of temperatures is an essential requirement in our experiments. The temperature logger created for this experiment is detailed in the article *Easy to Use Tailored Automatic Data Logger Design Using Microcontrollers in a Two-Stage Gasification Experiment* also published in the current issue.

Table 3
The softening properties of the ashes of the coal

Properties	Temperature, °C
Shrinkage starting temperature	1108
Deformation temperature	1257
Hemispherical temperature	1346
Fluid temperature	1376

2.3. Water fraction analysis

The water fraction formed in our experiment is mainly composed of water and small amounts of condensed hydrocarbons (tar). The amount of water fraction was measured and sampled after each experiment and the combustion heat of the tar fraction was also determined. Presented in the base material conversion section in *Figure 2*, it is noticeable that the amount of liquid phase formed during the high temperature pyrolysis is higher than that of the low temperature. After settling, the liquid phase can be separated into two phases which shows the same tar to water ratio phase after both low and high temperature pyrolysis, 13% to 87% respectively. After analysing the combustion heat of the formed tar, it was concluded that while the amount of tar formed is small, it cannot be overlooked as its average heat of combustion 16.48 MJ/kg. Based on these results, the amount of tar formed can be used in power generation. However, according to the literature its corrosive properties is a main disadvantage [12, 13] of its usage. The implementation of corrosion-resistant combustion equipment entails considerable additional costs, but due to the small amounts produced, further gasification can be a considerable solution.

2.4. Energy conversion

From the data acquired from the elemental composition, heat of combustion and quantities, we can determine the energy conversion rates. As a consequence of the space constraints, the formation and the analysis of the synthesis gas are detailed in the article *The Two-Stage Pyrolysis of Hungarian Brown Coal to Reduce Hydrocarbons within Synthesis Gas,* also published in the current issue.

The base material used in our experiment has higher heating value (HHV). In the pyrolysis experiment, this was partly converted to a gas phase and partly to a liquid phase. The distribution of each phase from the samples of the two pyrolysis experiments and the base material are presented in the *Figure 12*. With the increase of the experiment temperature, the energy content locked in the solid phase is transformed into gas and liquid phase.

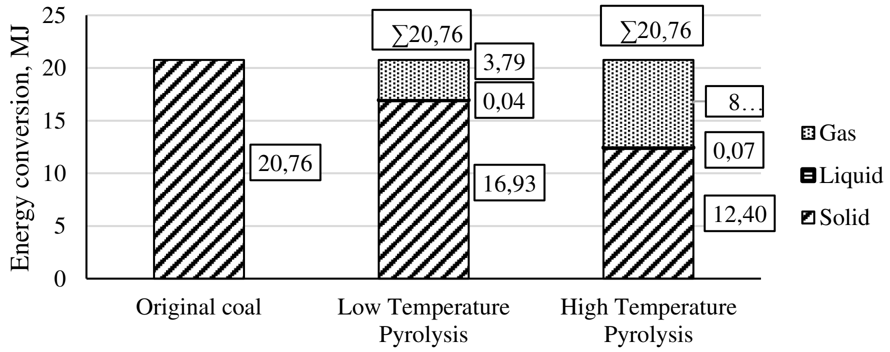

Figure 12

The energy content of the sample taken from the base material and pyrolysis experiments

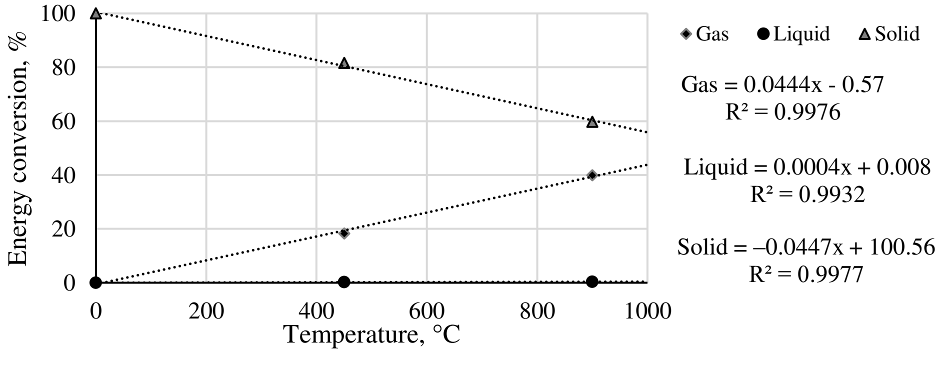

Figure 13

Energy content of the produced materials presented in relation to temperature

If the transformed energy is considered 100% (20.76 MJ/kg), the linear coefficient is clearly visible when the generated weighed combustion heat is presented in relation to the temperature *(Figure 13)*. Based on the equations given on the diagram, the percentage of the energy content of the base material at the given temperature present as solid, liquid and gaseous phase can be determined.

SUMMARY

The analysis of the solid and liquid phase products were presented in this paper, detailing the conversion rates and processes from our two-stage pyrolysis experiment. The experiment setup is based on two reactors placed in two independently controlled furnaces, and connected to allow the flow of the produced synthesis gas from one reactor to another. In each reactor, different reactions take place at different temperatures. The aim of this paper was to present the analysis of the produced solid and liquid phases.

The conversion rate at the high temperature pyrolysis was expected to be higher than at lower temperature. However, around 70% of the carbon and sulphur content of the base material is still in the product, even after the high temperature pyrolysis. Therefore, the most apparent route for further energetic use of the product is steam gasification, especially considering the high sulphur content still trapped in the produced coke.

From the determination of ash softening it became evident that the precise tracking and control is essential to avoid any malfunction of the system that could be caused by ash softening and clogging the reactor pipes.

Also, it was determined that the liquid phase formed in the cooling systems contains small quantity of by product in the form of tar. Although, the quantity of tar is small, it has significant energy content. Therefore recycling it can also be beneficial.

By examining the energy conversion, a relation between the percentage of the energy content of the base material and the temperature can be drawn. At any given temperature the solid, liquid and gaseous phase present in the product can be estimated.

ACKNOWLEDGEMENT

The authors are grateful to Mária Ambrus for her advice.

REFERENCES

[1] BÜKI, G.: *Energetika*. Műegyetemi Kiadó, 1997.

[2] DUDLEY, B.: *BP Statistical review of world energy*. 2016. https://www.bp.com/content/dam/bp/pdf/energy-economics/statistical-review-2016/bp-statistical-review-of-world-energy-2016-full-report.pdf (Downloaded: 2017. 04. 01.)

[3] *International energy outlook 2016*. U.S. Energy Information Administration. Washington. 2016. https://www.eia.gov/outlooks/ieo/pdf/0484(2016).pdf (Downloaded: 2017. 03. 28.)

[4] SPEIGHT, J. G.: *The chemistry and technology of coal*. CRC Press, 2013, Boca Raton

[5] PINTÉR, I.: *A termikus kezelés helye és szerepe a hulladékgazdálkodásban. Hulladékok termikus hasznosítása*. Budapest, 2014.

[6] WETHEROLD, B.–Orr, D.–MAXWELL, D.: *A Comparison of Gasification and Incineration of Hazardous Wastes*. U.S. Department of Energy National Energy Technology Laboratory, Morgantown, 2010.

[7] DAI, Q.J. –JIANG, X .G.–JIN, Y .Q.–WANG, F.–CHI, Y.–YAN, J. H.–XU, A. H.: Investigation into advantage of pyrolysis over combustion of sewage sludge in PCDD/FS control, *Fresenius Environmental Bulletin*, Vol. 23, Issue 2A (2014), 550–557.

[8] BASU, P.: *Biomass Gasification, Pyrolysis and Torrefaction: Practical Design and Theory - Second Edition*, Elsevier Inc., Burlington, 2013.

[9] REZAIYAN, J.: *Gasification technologies: A primer for engineers and scientists*. CRC Press, 2005.

[10] Lackner, M.–Palotas, A.–Winter, F.: *Combustion: From Basics to Applications*. Wiley-VCH Verlag GmbH & Co. KGaA, Weinheim, 2013.

[11] CEN/TS 15370-1: Solid biofuels. Method for the determination of ash melting behaviour. Characteristic temperatures method, 2006.

[12] LEHTO, J.: Known Challenges Associated with the Production, Transportation, Storage and Usage of Pyrolysis Oil in Residential and Industrial Settings. *Technical Information Exchange on Pyrolysis Oil*, Manchester, 2012.

[13] REDFEN, K.: Utilization of pyrolysis oil in industrial scale boilers, 2013. http://lib.dr.iastate.edu/cgi/viewcontent.cgi?article=4074&context=etd (Downloaded: 2017. 01. 01.).

Materials Science and Engineering, Volume 42, No. 1 (2017), pp.59–68 .

TWO-STAGE PYROLYSIS OF HUNGARIAN BROWN COAL TO REDUCE HYDROCARBONS WITHIN SYTHESIS GAS

ANDRÁS ARNOLD KÁLLAY[1]–VIVIEN VINCZE[2]–GÁBOR NAGY[3]

During the research, the aim was the expansion of the potential of coal gasification and pyrolysis by the production of synthesis gas that can be used as a chemical raw material. Controlling the process of the pyrolysis experiment can be challenging. The temperature control of the process on its own is not enough to alter the composition of the produced synthesis gas, especially if all reactions take place in a single stage. The main objective of our research is to separate the low temperature and high temperature pyrolysis, and gain additional control over the whole process. Two separate reactors were connected through a still pipe that could allow gas flow between them, and they were inserted in two independent temperature controlled furnaces. Even though synthesis gas produced at low temperatures has high methane quantity, this perhaps can be thermally decomposed by forcing it through the high temperature zone of the experiment setup. The prospects of this setup have been investigated detailing the gasifier setup. The results of experiments will also be discussed in this article.

Keywords: coal gasification, synthesis gas utilisation, two stage gasification

INTRODUCTION

Nowadays, coal is one of the most significant energy sources. This fact is well demonstrated by the world's energy consumption expressed in primary energy sources. The amount of energy obtained from coal alone is almost equal to the energy obtained by all other energy sources combined *(Figure 1)* [1].

The most widespread method for coal-based energy production is combustion. Almost half of the coal used worldwide as primary energy source is used for electric power generation [2], and heat generation for industrial processes is in second place. In recent years, the conversion of coal to gaseous and liquid raw materials (chemical raw material or fuel) is also becoming increasingly important. Coal is a non-renewable fossil fuel, so the supplies are constantly decreasing. According to a 2015 study, the available reserves will last for another 114 years, considering the current rate of consumption [3]. However, the demand has been steadily increasing in last few decades. The utilisation of coal in power generation can be beneficial, having a relatively low cost compared to other fossil-based fuels like natural gas, but it also has many disadvantages. One of the major disadvantages is the SO_2 emission rates of coal combustion. Flue gas can be cleaned but the cost of these processes, especially considering the by-products and the ever-stricter emission regulations, can slowly outweigh the benefits, and the processes will become unsustainable.

---

[1] University of Miskolc, Department of Combustion Technology and Thermal Energy
Miskolc-Egyetemváros 3515, Hungary
tuzaak@uni-miskolc.hu

[2] University of Miskolc, Department of Combustion Technology and Thermal Energy
Miskolc-Egyetemváros 3515, Hungary

[3] University of Miskolc, Department of Combustion Technology and Thermal Energy
Miskolc-Egyetemváros 3515, Hungary

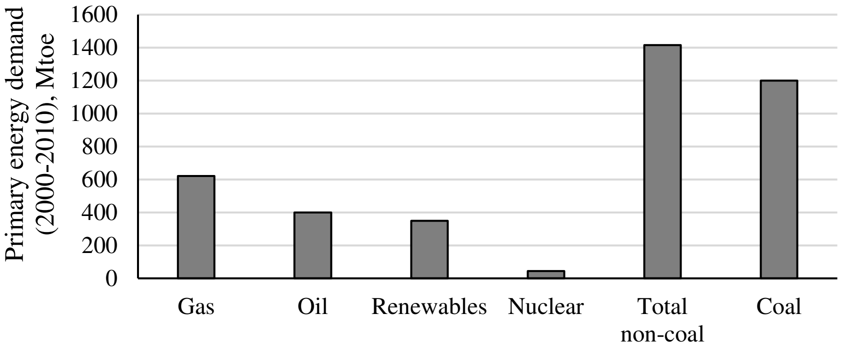

Figure 1

Incremental world primary energy demand by fuel (2000–2010) [1]

One solution could be reductive steam gasification, as the released sulphur in this case is in the form of hydrogen sulphide. This can be cleaned and converted to valuable by-products, as sulphur or sulphuric acid are in high demand by the chemical industry. This could be especially significant in the case of low rank coals that have 2–3% sulphur content within the raw material. The gasification of low rank coals is not as straightforward, in terms of producing synthesis gas with the required H_2/CO ratio for specific chemical industrial applications (*Table 1* [4]).

Table 1

Synthesized final products and the required H_2/CO ratios for the synthesis [4]

Product	Basic chemical reactions	H_2/CO ratio
FT liquid fuels	$2n\ H_2 + n\ CO \rightarrow C_nH_{2n} + n\ H_2O$ $(2n+1)\ H_2 + n\ CO \rightarrow C_nH_{2n+1} + n\ H_2O$	2.0 2.1
Methanol	$2\ H_2 + CO \rightarrow CH_3OH$	2.0
Ethanol	$2\ CO + 4\ H_2 \rightarrow C_2H_5OH + H_2O$	2.0
Higher alcohols	$n\ CO + 2n\ H_2 \rightarrow C_nH_{2n+1}OH + (n-1)\ H_2O$	2.0
Dimethyl ether	$2\ CO + 4\ H_2 \rightarrow CH_3OCH_3 + H_2O$	2.0
Acetic acid	$2\ CO + 2\ H_2 \rightarrow CH_3COOH$	1.0
Ethylene	$2\ CO + 4\ H_2 \rightarrow C_2H_4 + 2\ H_2O$	2.0
Ethylene glycol	$2\ CO + 3\ H_2 \rightarrow C_2H_6O_2$	1.5
Acetic anhydride	$4\ CO + 4\ H_2 \rightarrow (CH_3CO)_2O + H_2O$	1.0
Ethyl acetate	$4\ CO + 6\ H_2 \rightarrow CH_3COOC_2H_5 + 2\ H_2O$	1.5
Vinyl acetate	$4\ CO + 5\ H_2 \rightarrow CH_3COOCHCH_2 + 2\ H_2O$	1.25

Synthesis gas or syngas is produced via the gasification or pyrolysis of coal. The main components are carbon monoxide and hydrogen. The gasification setups can be rather different regarding the application of the produced syngas, the base material used and if the synthesis gas represents the main product of the gasification. Hydrocarbon rich synthesis gas is mainly utilised by the energy industry. Synthesis gas that is mainly composed of hydrogen and carbon monoxide is chiefly used by the chemical industry. Within the chemical industry, the required ratio of these two components, as represented in Table 1, is determined by the final product of the chemical synthesis.

A single stage setup is used in most gasifier systems (Lurgi, Shell, GE Energy, U-Gas etc.) [5], where the raw-material is introduced in a step-by-step fashion. However, two-stage setups are less widely used. One example is coke production where pyrolysis takes place at a low temperature, then the produced hydrocarbon rich syngas is used in coking process for heat generation [6].

The used method is different, in terms of setup. The synthesis gas produced in the low temperature pyrolysis is forced through the high temperature pyrolysis zone in a closed system. The final syngas is expected to have reduced hydrocarbon ratio and increased quantities of H_2 and CO.

1. MATERIALS AND METHODS

The low rank brown coal used in the gasification experiment is from the North-East brown coal basin in Hungary.

The flow route of the syngas produced in the experiment is presented in the *Figure 2*.

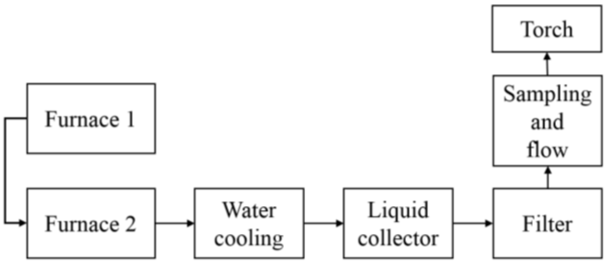

Figure 2
The flow route of the synthesis gas produced during the experiment

Two series of experiments were conducted in this research, all with different setups:

- In the first series of experiments, both reactors in the furnaces were filled with previously dried brown coal. Both furnaces were set to 450 °C final temperature, with a maximum heating rate.
- In the second series of experiments, the two furnaces were set to different temperatures, with coals from the different stages of pyrolysis. The reactor in the bottom furnace *(Figure 2, Furnace 2)* was filled with brown coal from the previous series of low temperature pyrolysis experiments and set to a final temperature of 900 °C. The high temperature pyrolysis was started and when the gas flow rate decreased below 2 l/h, the furnace on the top *(Figure 2, Furnace 1)* was turned on. The reactor in the top furnace was filled with pre-dried brown coal and the temperature was set to 450 °C. The produced syngas in the top reactor, following the gas flow path, must flow through the bottom side reactor where the temperature is set to 900 °C. The hydrocarbons in the syngas of the low temperature pyrolysis (450 °C) are expected to break down to carbon monoxide and hydrogen while flowing through the high temperature zone of the gasification setup. This way, synthesis gas with low ration of hydrocarbons and with hydrogen and carbon monoxide as main components can be produced, which is the aim of the experiments.

The quantity of the gas produced in the gasification experiment was measured with Medingen type rotameters (3–30 and 20–260 l/h). As the amount of coal fed to the furnace was not always the same, to be able to compare the l/h values, they were converted to 1 kg base material. The gas compositions were determined with an Agilent 490 Micro GC, using a COX column channel. Using the COX column, the MicroGC can detect the main components of the synthesis gas (CO, CO_2, H_2, CH_4) with a sampling rate of 2 minutes.

The adiabatic flame temperatures (T_{max}) were calculated for every gas sample taken using an iterative method, taking into consideration the calculated LHV [7], the specific heat capacities found in the literature [8] and the combustion theory equations [9].

2. RESULTS

2.1. Single stage experiment

To produce a starting material with high energy density for the high temperature pyrolysis, both reactors were filled with previously dried low rank brown coal in the first stage. The temperatures were set to 450 °C with a heating rate of 20 °C/min. Even though both furnaces were set up to the same temperatures and heating rates, there were observable differences in the actual heating rates *(Figure 3)* as a result of the differences in their nominal power output. The evolution of the produced syngas in relation to time is also presented on *Figure 3*. Observable synthesis gas flow is first detected at the 300 °C which steadily increases to 120 l/kg at 450 °C. After this point, the gas flow stabilises until the volatiles, which can be released at this low temperature, are discharged. The experiments were concluded after the gas flow decreased to 2 ml/h.

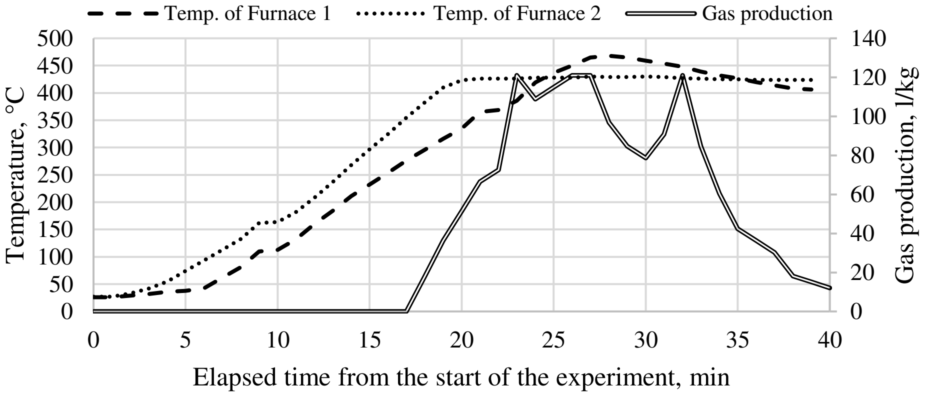

Figure 3

The evolution of temperatures and gas flow in relation to time in the two reactors (Single stage experiment)

Based on the composition of the produced synthesis gas *(Figure 4)*, it can be stated that the initial temperature, where the volatiles release starts, is sufficient for the volatiles to react with the oxygen trapped within the reactor and combust. This is analysed in depth along with the results obtained with the use of a derivatograph detailed in the in the article "*Analysis of*

Solid and Liquid Phase Products of the Two-Stage Pyrolysis" also published in the current issue. At the beginning of the gas flow, as it can be seen on the *Figure 4*, the oxygen quantity is declining while the ratio of the carbon dioxide is increasing. The ratio of carbon dioxide is peaking at 50%V/V. With the declining oxygen ratio, there is not enough oxidizer left for combustion reactions. Therefore, the amount of carbon monoxide, methane and other hydrocarbon compounds start to increase within the produced synthesis gas. Previous experiments showed that the amount of other hydrocarbons within the synthesis gas can be accounted for the 20%V/V of the total amount of the methane produced. The methane production of the pyrolysis experiment shows an increasing trend throughout the process, peaking at 12%V/V of the syngas produced.

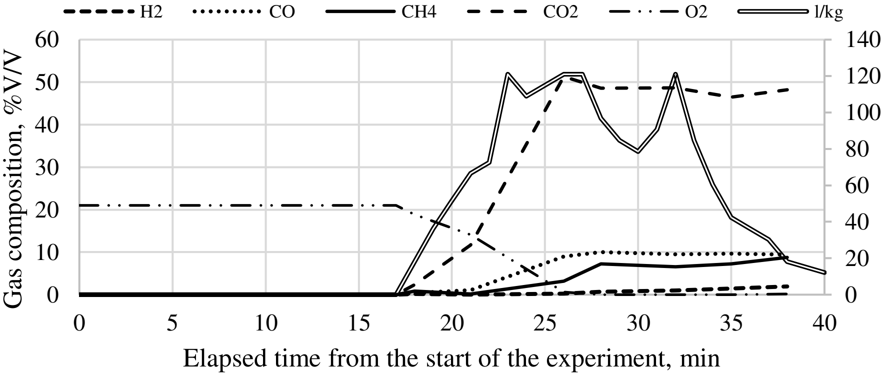

Figure 4

The evolution of the synthesis gas composition in time (Single stage experiment)

For the produced synthesis gas to be utilised in the chemical industry, it would require at least a H_2/CO ratio of 1 *(Table 1)*. However, the ration of the syngas from low temperature pyrolysis is well below this *(Figure 5)*. The use of this synthesis gas case would require a large amount of hydrogen addition. Furthermore, the high ratio of other gas compounds, like hydrocarbons, would require a separation which would further increase the cost.

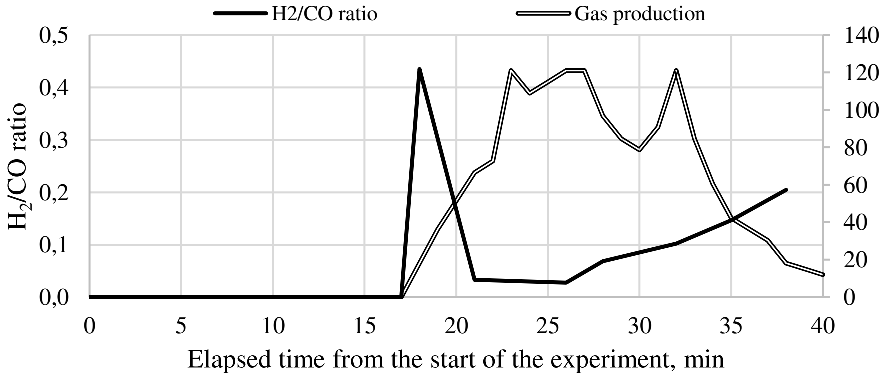

Figure 5

The evolution of H_2/CO ratio throughout the experiment (Single stage experiment)

The calculated adiabatic temperature is increasing in time, due to the increasing ratio of combustible compounds within the synthesis gas. The calculated flame temperature using the data acquired from the DSO-Tigáz Ltd – with 90–95%V/V methane, 3–5%V/V other hydrocarbons and 1–3%V/V non-combustible compounds [10] – is just below 1500 °C at its peak. However, it is still well below the 2000 °C of adiabatic flame temperature measured in the case of the natural gas *(Figure 6)*.

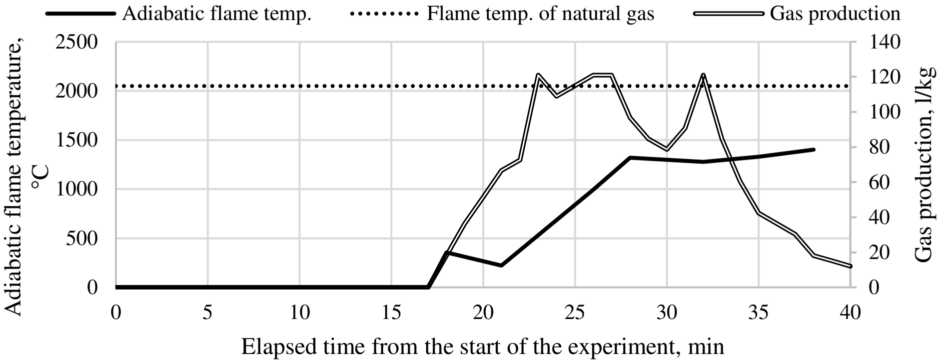

Figure 6

The evolution of adiabatic flame temperature in the one stage experiment

2.2. Two stage experiment

In this series of experiments the two furnaces were started with a time shift between the stages. First, the furnace marked as *Furnace 2* was turned on *(Figure 7)*. The furnace was set to 900 °C final temperature with a heating rate of 20 °C/min. After the gas flow decreased to 2 l/h, the other furnace marked with *Furnace* 1 was turned on and set to 450 °C, with a heat rate of 20 °C/min. *Furnace 2* was held at 900 °C. The aim of the experiment was to investigate the possibility of hydrocarbon ratio reduction during the low temperature pyrolysis, by forcing the gas through a high temperature zone (*Furnace 1*). *Figure 7* also shows the synthesis gas flow rate throughout the experiment. It is apparent, that in the case of *Furnace 2,* syngas production starts around 450 °C, where the low temperature pyrolysis was finished in the first stage of the experiment.

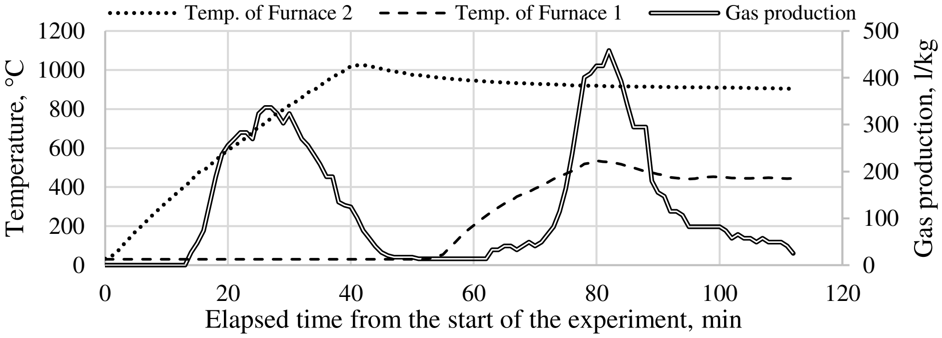

Figure 7

The evolution of the temperatures and the gas flow of the two-stage experiment

Separating the two stages of the gasification, it is obvious that the low temperature pyrolysis (450 °C) has lower synthesis gas yield than the higher temperature (450–900 °C) pyrolysis *(Figure 8)*. The flow rates of the single- and two-stage gasification are also different, comparing the low temperature pyrolysis with and without passing through the high temperature zone (900 °C). In case of the latter, the flow rate is noticeably higher. This effect is mostly caused by the decomposition of hydrocarbons in the gas phase and the volatiles in the vapour phase that would otherwise condense. At this higher temperature gasification also takes place, using oxygen and water vapour from the decomposed hydrocarbons (detailed in the in the article *Analysis of Solid and Liquid Phase Products of the Two-Stage Pyrolysis* also published in the current issue).

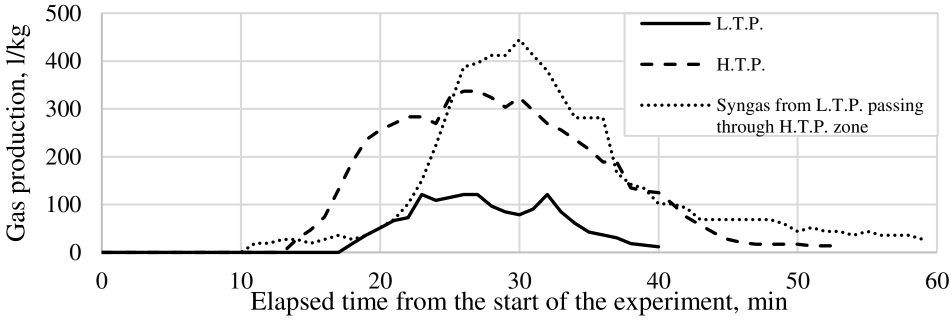

Figure 8
The flow rate comparison of the synthesis gas in the case of the two stage gasification at different temperature ranges and stages

Similarities between the composition of the syngas from high and low temperature pyrolysis can also be observed *(Figure 9)*. First of all, both the carbon dioxide and oxygen ratios were high at the beginning of the experiment. This is the result of the similar start up conditions, namely the non-inert filling of the gasifier with brown coal.

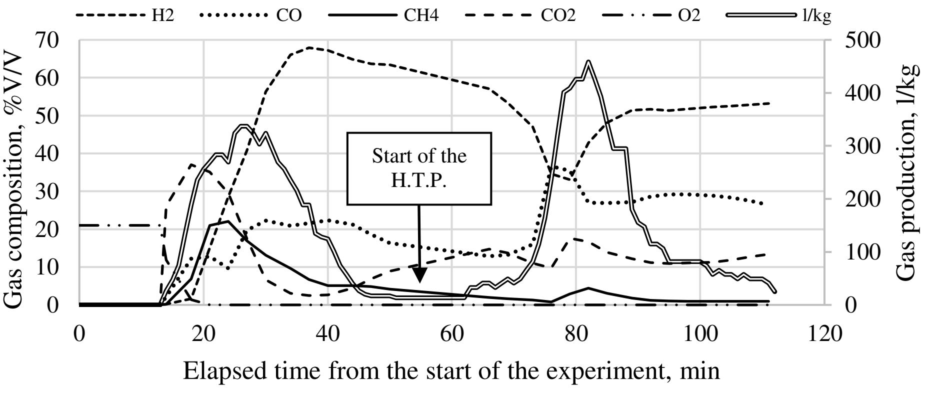

Figure 9
The evolution of the gas composition in the two-stage experiment

The reaction of the oxygen and the char results in high carbon dioxide ratio. After reaching the maximum peak, the ratio of carbon dioxide is starting to drop, while the ratio of methane and hydrogen is rising within the synthesis gas. By the time the flow rate reaches its peak point, the concentration of carbon dioxide is fallen below 20%V/V, and the carbon monoxide and hydrogen ratios are increased above 20%V/V and 40%V/V, respectively, and are steadily increasing. The methane concentration between the temperature range 500–700 °C are steadily above 20%V/V, with its peak concentration of 23%V/V.

The most significant reactions taking place at the high temperature (900 °C) zone of the gasifier are shown below *(Equations 1–6)*. The equilibrium of the reactions presented are shifting to the right, as it can be seen from our results shown in *Figure 9*. The CO ratio is almost doubled, while the methane ratio is decreased to just a few percent, compared to the single stage gasification experiment. The ratio of CO_2 decreased as well, to nearly half of that in the single stage experiment. The presented results are clear evidence of the advantages of the two-stage gasification compared to the single stage gasification if the aim of the gasification is to produce synthesis gas with increased carbon monoxide and hydrogen ratios and decreased carbon dioxide ratio.

Methane reforming	$CH_4 + CO_2 \leftrightarrow 2\,CO + 2\,H_2$	(1)
Methanation	$CH_4 + H_2O \leftrightarrow CO + 3\,H_2$	(2)
Boudouard reaction	$CO_2 + C \leftrightarrow 2\,CO$	(3)
Steam char reaction	$C + 2\,H_2O \leftrightarrow CO_2 + 2\,H_2$	(4)
Water-gas shift reaction	$CO_2 + H_2 \leftrightarrow CO + H_2O$	(5)
Methane decomposition	$CH_4 \leftrightarrow C + 2\,H_2$	(6)

It is apparent from the series of the single and two-stage experiments, that both the higher temperature pyrolysis and the synthesis gas forced to flow through the high temperature zone of the gasifier have increased H_2/CO ratios, compared to the low temperature pyrolysis *(Figure 10)*.

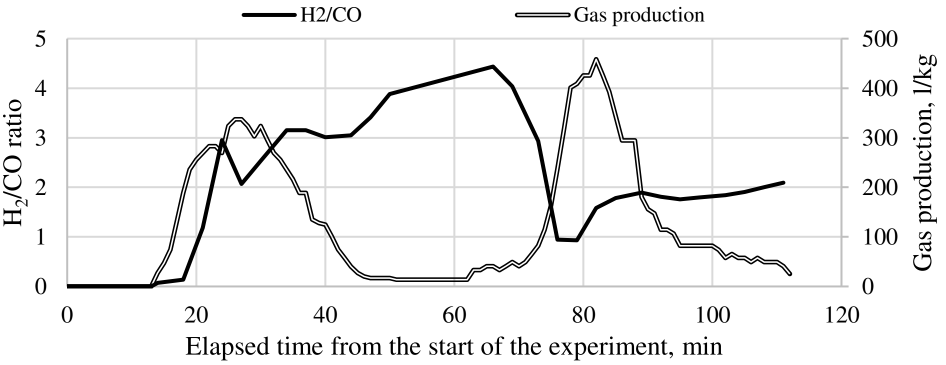

Figure 10

The evolution of the H_2/CO ratio and the gas flow in the two-stage experiment

In the high temperature pyrolysis, the ratio of H_2/CO reached up to 4/1, while the synthesis gas produced via low temperature pyrolysis and forced flow through the high temperature zone, reached up 2/1 ratio. It can be concluded, that with a two-stage setup an increased hydrogen/carbon monoxide ratio can be accomplished, while the methane concentration can be decreased almost tenfold compared to the low temperature pyrolysis. Furthermore, by mixing the synthesis gas from the low temperature and high temperature zones, the syngas can be steadily held above a H_2/CO ratio that could serve as base material for chemical industrial use in synthetizations *(Table 1).*

In addition to these results, based on the adiabatic flame temperatures calculated from the samples taken throughout the two-stage experiments it can be concluded that the values are comparable to those of the natural gas *(Figure 11).* These results demonstrate the viability of this two-stage setup. The produced synthesis gas is a viable option for base material for chemical industrial application while at the same time it can be used in power generation applications.

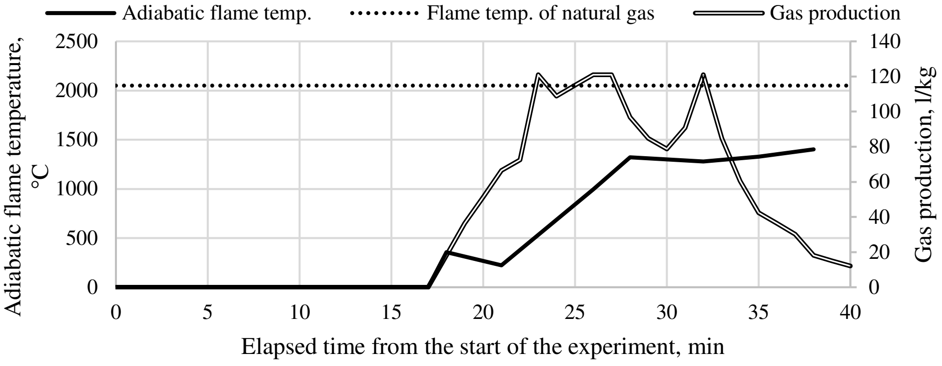

Figure 11

Evolution of the adiabatic flame temperature and flow rate in the two-stage experiment

CONCLUSION

The main goal of this research was to investigate the first step of every gasification, the pyrolysis, focusing on the low temperature pyrolysis, as most of the volatiles are released during this phase of the gasification. Through separating the pyrolysis into two stages, the processes taking place and the composition of the synthesis gas produced could be further investigated. The experiment was setup using two separate furnaces to fine-tune the conditions of the pyrolysis. Therefore, the composition of the produced synthesis gas can be altered. The results clearly show that this setup is a viable solution to reduce the amount of methane and increase the carbon monoxide and hydrogen ratios within the synthesis gas. The results are also encouraging to further investigate this two-stage setup with the inclusion of the redox char gasification in the high temperature zone, while the low temperature zone will be kept with similar setup. This will evaluate the possibilities of the two-stage setup within the whole process and could lead to a "high quality" synthesis gas production from low rank coals which can be used in both, power generation applications and industrial chemical applications.

ACKNOWLEDGEMENT

The authors are grateful to Mária Ambrus for her advice.

REFERENCES

[1] World Energy Council: World Energy Resources. London, 2013. https://www.worldenergy.org/wp-content/uploads/2013/09/CompleteWER_2013_Survey.pdf (Downloaded: 2017. 04. 10.)

[2] *International energy outlook 2016*. U.S. Energy Information Administration. Washington. 2016. https://www.eia.gov/outlooks/ieo/pdf/0484(2016).pdf (Downloaded: 2017. 03. 28.)

[3] DUDLEY, B.: *BP Statistical review of world energy*. 2016. https://www.bp.com/content/dam/bp/pdf/energy-economics/statistical-review-2016/bp-statistical-review-of-world-energy-2016-full-report.pdf (Downloaded: 2017. 04. 01.)

[4] CALABRESE, P. A.–BAI, D.: *Engineered fuel feed stock useful for displacement of coal in coal firing plants*. Patent application. WO2009158539 A1. 2009.12. 30.

[5] BREAULT, R. W.: Gasification Processes Old and New: A Basic Review of the Major Technologies. *Energies,* Vol. 3, Issue 2 (2010), 216–240.

[6] HIGMAN, C.–BURGT, M. V. D.: *Gasification*. Elsevier Inc., Bulrington, 2008.

[7] Heating value of gases from biomass gasification. Report prepared for: IEA Bioenergy Agreement, Task 20 - Thermal Gasification of Biomass Lars Waldheim, Torbjörn Nilsson TPS Termiska Processer AB May 2001. (Downloaded: 2015. 10. 19.) http://www.ieatask33.org/app/webroot/files/file/publications/HeatingValue.pdf

[8] Engineeringtoolbox http://www.engineeringtoolbox.com/ (Downloaded: 2016. 12. 10.)

[9] BÍRÓ A: *Tüzeléstan*. Miskolci Egyetem, 1997.

[10] www.tigazdso.hu (Downloaded: 2017. 04. 06.)

Materials Science and Engineering, Volume 42, No. 1 (2017), pp. 69–77.

ENHANCING ENERGY COST EFFICIENCY OF HOT ROLLING

ERIKA KUN[1]

Energy cost driven production management of high temperature technologies is rather questionable, generally considered unfeasible. Hot rolling is a typical high temperature process. Unprepared and unexpected intervention, shutdown of technology to decrease its energy costs results in deterioration of end product quality, increase of production wastes and even the damage of manufacturing technology. In the meantime increasing energy and energy cost efficiency, thus decreasing unit heat and electric energy consumption and costs is crucial to stay competitive. Besides from the aspect of real time energy markets targets of increasing energy and cost efficiency can be different in the continuously altering price environment. Next paper focuses on modeling unit energy consumption of hot rolling technology, and the possibilities of enhancing energy cost efficiency in different price scenarios.

Keywords: high temperature technology, energy efficiency, energy cost efficiency, real time energy markets

INTRODUCTION

It is generally accepted that energy cost driven production is not feasible at high temperature technologies. Being an integrated-steel-producer employed energy trader I had difficulties accepting this axiom. Next paper discusses question of whether and how it is possible to adjust production to energy prices both technically and economically reasonable way.

ISD Dunaferr company group is an integrated steel producer. Both upstream (semi-finished products) and downstream (finished product manufacturing) processes operate on its site. Hot rolling mill is the first downstream producer, where continuously casted slabs are transformed to either coils or sheet metal.

Hot rolling technology has high energy consumption, heat, thus combustion fuel consumption for reheating slabs is significant, and electrical energy usage is also great. The process uses large amount of cooling water and technology gas (nitrogen) as well.

Heat energy consumption and electrical energy consumption are dependent on each other. Is it possible to model this relationship considering the rather diverse output of the hot rolling mill? In case of positive answer are both electricity and heat energy equally important or – according to the generally accepted – only heat energy should be examined?

However heat energy consumption defines the unit energy consumption of forming, the characteristics of the electric energy load profile could contribute to energy cost efficiency. The characteristics of the hot rolling mill's electricity consumption defines the overall load profile of the company group. Power market is a real-time market with great price volatility. Programming high load demand to low-price periods could result significant savings in electricity costs. (Time of usage energy consumption) [1].

---

[1] ISD POWER Ltd.,
1–3. Vasmű tér, Dunaújváros 2400
kun.erika@isdpower.hu

1.1. Unit heat consumption

Slabs are re-heated to forming temperature by high performance reheating furnaces – pusher-type and walking beam furnaces. Heat energy demand of reheating steel slabs (Q_{slab}) could be defined with *Formula 1*.

$$Q_{slab} = m * c(T_2 - T_1),\ [\text{GJ/t}]\ [1]$$

where Q_{slab}: heat absorbed by slabs, enthalpy of slabs;
m: weight of slabs;
T_2 and T_1: discharging and charging temperature of slabs;
c_p: specific heat of steel (1).

Examining the rule represented by *Formula 1* it shows that increasing charging temperature the total heat demand of reheating decreases – see calculation in *Table 1*. The unit heat energy consumption reflects to one of the company group's pusher-type reheating furnace.

Table 1

Heat energy consumption and charging temperature of slabs

	Temperature of slabs		
	20°C	400°C	700°C
Unit heat energy	1,55 GJ/t	1,25 GJ/t	0,94 GJ/t
Savings of heat energy	0	19%	39%
Heat absorbed by slabs[2]	0,8 GJ/t	0,56 GJ/t	0,37 GJ/t

Studying the unit heat energy consumption and heat absorbed by slabs row of *Table 1* it is striking that decrease of unit heat energy consumption is bigger that the heat absorbed by slabs. That could be of several reasons, eg. smaller heat losses due to shorter reheating times, differences in furnace controls.

Table 2 shows the effect of decreasing the discharging temperature on heat energy consumption.

Table 2

Heat consumption[GJ/t] and discharging temperature

		Discharging temperature [°C]		
		1220	1240	1260
Charging temperature [°C]	20	0,8335	0,8523	0,8725
	100	0,7911	0,8099	0,8301
	200	0,7377	0,7564	0,7766

---

[2] Target reheating temperature = 1200 °C

It is visible that whilst charging temperature can be increased by hundreds of degrees, the decreasing of discharging temperature shows power-of-an-order difference in possible heat energy consumption decrease – practically 40–50°C.

1.2. Unit power consumption

The temperature dependence of electrical energy consumption of forming can be examined using *Formula (2)*.

Formula (2) shows the electrical energy demand of forming equipment, motors and drives.

$$W_{el} = W_W * \eta \quad \text{(W)} \; (2)$$

where

$\mathbf{W_w}$	$V*k_{wm}*\varphi_h$, unit rolling-work,
$\boldsymbol{\varphi_h}$	size-alteration of deformation, int he direction of biggest deformation,
$\mathbf{k_{wm}}$	mean deformation strength,
$\boldsymbol{\eta}$	overall efficiency indicator, consist of the bearing-friction coefficient, efficiency of drives and efficiency of motors [3].

Examining *Formula (2)* it is visible that load, thus electricity consumption of rolling is temperature dependant, as the mean deformation strength of the material is a function of temperature.

Table (1 and *2)* shows that the required heat energy thus combustion fuel is determined by the target reheating temperature of steel.

In short: setting lower temperatures to start rolling, the heat energy thus combustion fuel required for re-heating the material decreases. In the meantime due to the bigger deformation strength caused by lower temperatures, the power consumption of forming will increase. The two tendencies reverse, theoretically at optimal target reheating temperature the sum of unit energy consumption of reheating and forming is minimal [4].

2. COLLECTING AND ANALYZING DATA

Great number of data can be obtained in relation with forming in the company group's hot rolling mill quality management system. I processed this data to be able to seek evidence for the previously stated. I created an 'energy-consumption related database, with data mining and database management. To justify the temperature dependence of power consumption of rolling I use the statistical method of linear regression – instead of the above formulas.

While performing data analysis I collected energy consumption related attributes to each workpiece (e.g. discharging temperature, thickness reduction, temperature of workpiece during processing) and the electrical energy consumption of forming equipment. I created a unit power consumption indicator, which is ratio of the total power consumption of roughing and continuous rolling, and weight of the down-coiled coil.[3]

---

[3] I use unit power (kWh/t) and heat consumption (GJ/t) data to examine energy consumption.

The technology phases of rolling are re-heating and forming. In this material the forming phases of roughing (where de-scaled raw strip is manufactured), and finishing (where the strip microstructure and size features are set) phases are examined.

Unit power consumption indicator is different in every phase of the technology due weight reduction caused by descaling of slabs and sheer cropping of sheet-metal strip. Whilst unit heat energy consumption of reheating refers to the initial weight of slabs, the total unit forming power refers to the down coiled strip. When we separate forming process to rouging and continuous rolling, the unit power consumption indicator has to be separated as well. In case of roughing the denominator is the initial weight of slabs (the loss due to de-scaling is not taken into consideration), in case of continuous rolling the denominator has to be the weight of down coiled strip.

Figure 1 shows the total unit forming power as the function of discharging temperature.

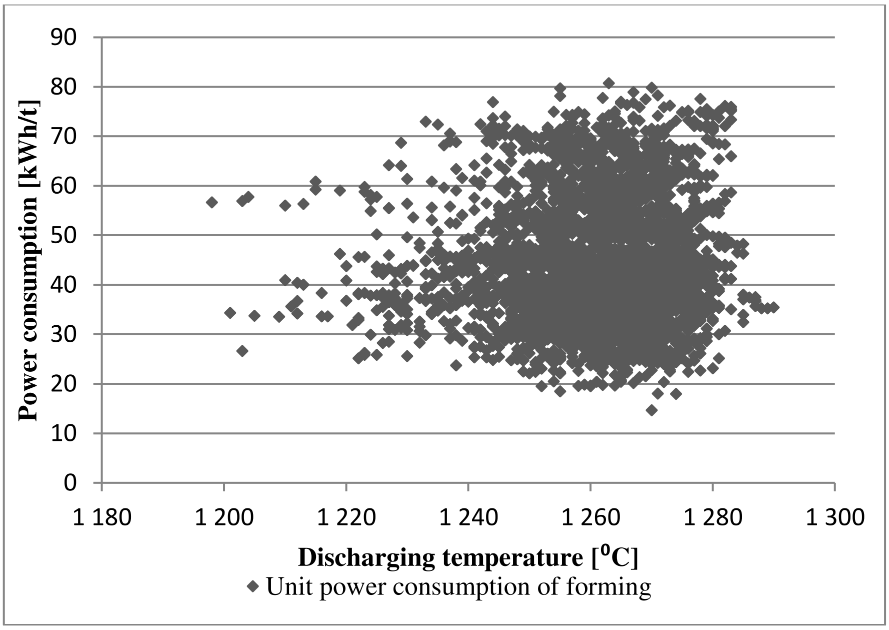

Figure 1

Discharging temperature and unit power consumption of forming

It shows stochastic relationship between discharging temperature and total unit forming power, due to the following:

- The forming equipment consists of two main group of tools: rougher tools and the continuous finishing line, of which the latter has its own temperature-control algorithm dependent upon the target microstructure of the finished product.
- The power consumption of tools is influenced by several factors besides deformation strength, like
  - target thickness of finished product,
  - deflection rate, scheduling of rolling,
  - overall width of slab,
  - width reduction of product during rouging etc.

Figure 2 shows the total unit forming electric energy consumption as function of target strip height (thickness).

The dots representing power consumption shows a 'function-like' relationship between the finished product thickness and power consumption of the whole forming process.

The differences between the power consumption belonging to each thickness value may arise from different deflection rate, changes of surface, differences in target rolling/finishing temperature or different deformation strength.

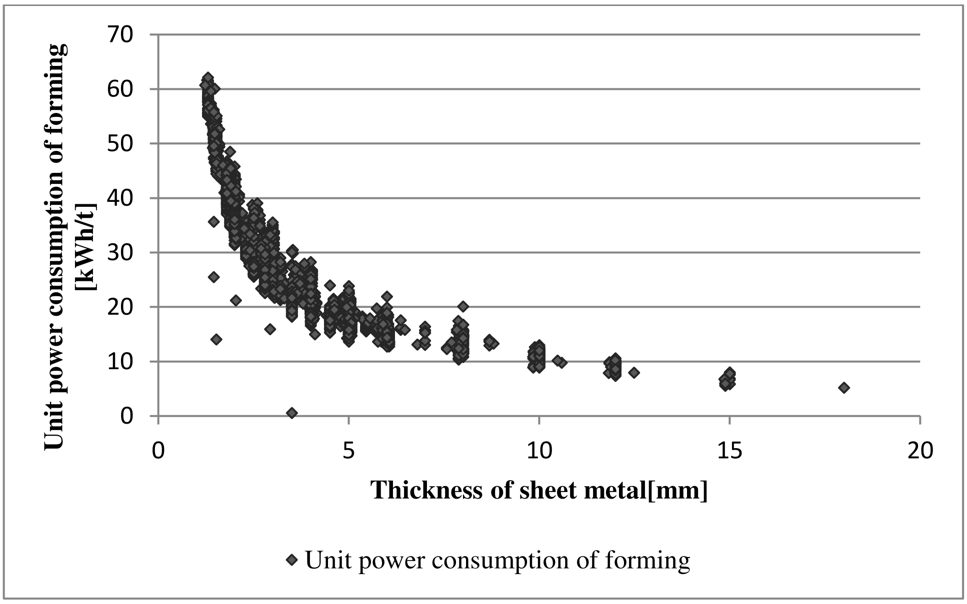

Figure 2

Power consumption of forming and target thickness of sheets

3. POWER CONSUMPTION OF ROUGHING AND TARGET DISCHARGING TEMPERATURE

When we separate the two main forming phase (roughing and finishing) from each other, complete different results are visible considering the discharging temperature dependence of unit power consumption

I performed statistical analysis on the assembled database using Excel's simple statistical functions to seek evidence for *Formula (2* and *3)* in factual measurement data. I calculated the covariance and correlation coefficients if there is a deterministic relationship between power consumption of roughing and discharging temperature. *Table 3* shows the results.

Numbers do not show any relationship between the forming power consumption and discharging temperature. The unit power consumption of roughing and discharging temperature shows loose relationship, the overheat[4] of slabs and power consumption is an over average relationship. The indicator is negative showing that the bigger discharging temperature the smaller is the power consumption.

---

[4] overheat: the difference between discharging temperature and target reheating temperature

Table 3

Statistical data on temperature dependence of forming power

	1. furnace	**2. furnace**
Covariance	–4,845	–4,334
Correlation		
Discharging temperature and total unit power consumption	0,065	0,079
Discharging temperature and power consumption of roughing	–0,266	–0,225
Overheating of slabs and unit power consumption of slabs	–0,579	–0,600

Figure 3 shows the results of figure 3 graphically, displaying the weak correlation between discharging temperature and unit power consumption of roughing. The dots representing power consumption show a declining trend, the higher the discharging temperature the lower the power usage.

The relationship is rather weak, the assuming a function-like relationship as result of linear regression would make our forecast rather uncertain (due to the big error terms).

The weak correlation could be caused by a few other factors:

- processed product structure is diversified both in quantity and size,
- roughing is a multi-phase technology: the raw-sheet is produced in 7–13 passes with reversing rolling, the energy consumption of each passes is defined by rolling velocity, thickness and width reduction.

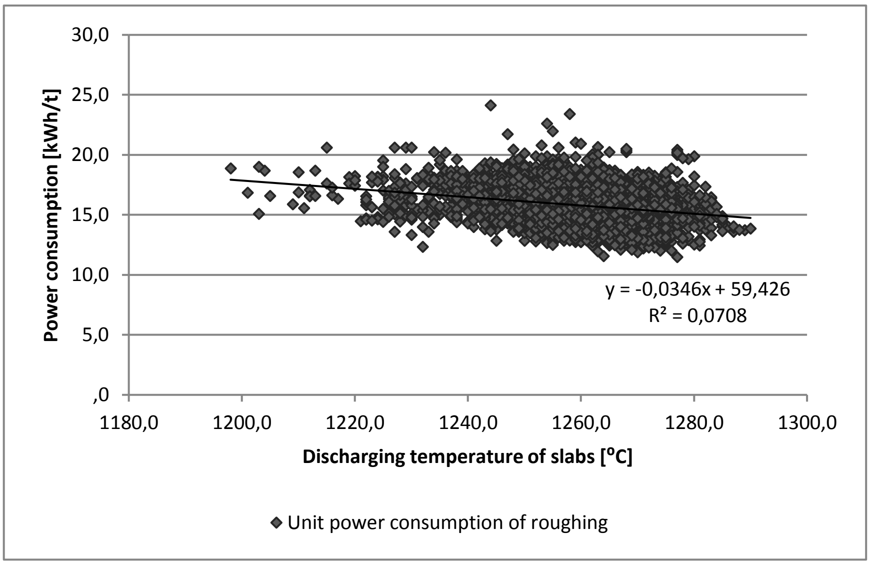

Figure 3

Discharging temperature and unit power consumption of roughing

Should overheat of slabs be considered as independent variable *Figure 4* could be drawn.

Figure 4 shows the overheat dependence of unit power consumption of roughing – for slabs heated in pusher-type furnace No1. The figure graphically shows stronger relationship between the two variables.

Overheat is the difference between target reheating temperature and discharging temperature. Overheat arises from different target reheating temperatures following each other in furnaces, and the combustion control of the furnace is set to higher target temperature. The thinner is the finished product, the higher the target reheating temperature. On the contrary the thicker the finished product the lower the target reheating temperature – the thickness off the rough sheet is set accordingly. The probability of an overheated slab being discharged from the furnace is P = 0,85, the expected value of overheat is T = 26,96 ^{0}C.

Figure 3 and *4* oversimplify the temperature dependence of unit electric energy consumption of roughing. For thorough further examination each phase of roughing (passes) and/or the unit power consumption thickness-based correction is needed.

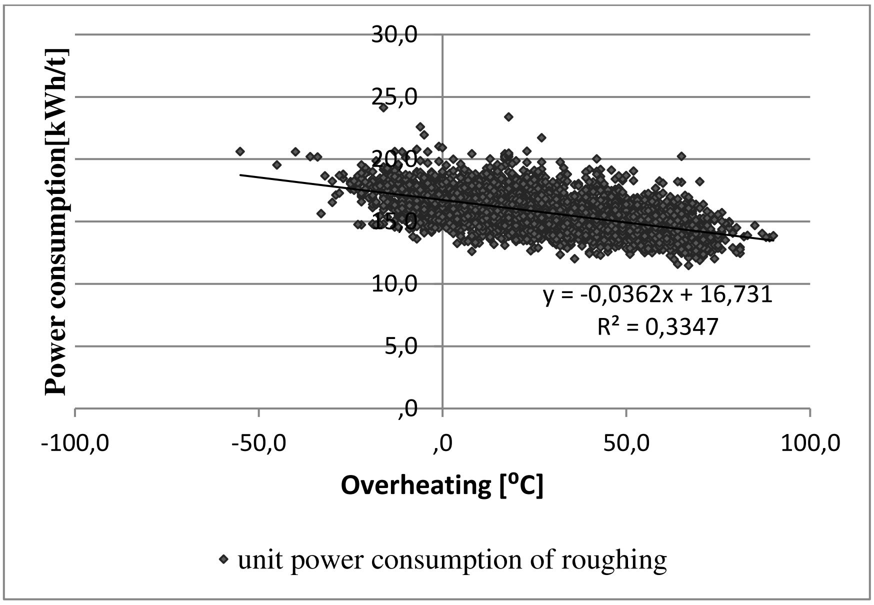

Figure 4
Overheat and power consumption of roughing

4. CALCULATION OF ENERGY COST EFFECTIVENESS

Using regression formula shown in *Figure 3* to calculate unit electric energy consumption and the heat demand from *Table 2* we can define unit energy consumption and energy cost relatively easily. The basis of saving is the factual discharging temperature of slabs (1260 ^{0}C). *Table 4* shows the possible cost saving.[5]

---

[5] During calculation I consider furnace losses as constant values.

Table 4

Achievable energy cost savings in various energy-price scenarios

	SCEN1	SCEN2	SCEN3	
Price of power	36	55	70	EUR/MWh
Price of natural gas	6	10	20	USD/GJ
Exchange rate1	312	312	312	HUF/EUR
Exchange rate2	285	285	285	HUF/USD

			Overall savings		
Target reheating temperature	Power	Heat demand	SCEN1	SCEN2	SCEN3
°C	kWh/t	GJ/t	thHUF		
1220	17,214	0,834	-76 717	-131 101	-288 110
1240	16,522	0,852	-40 154	-68 543	-150 040
1260	15,830	0,873			

- SCEN1 represents the 2016 price environment. It is visible that due to the low power and natural gas prices there is a little chance of cost saving.
- SCEN2 represents 2015, where the amount of saving achieved on energy prices should make one think of consider reviewing the operation of technology and improve its programming methods.
- SCEN3 represents high price environment, where energy cost adjusted manufacturing could result great savings.

Note: the P = 0,85% probability has to be taken into consideration in calculating the savings, that would result decrease of cost saving potential.

The amount of savings in *Table 4* draw attention to the fact that avoiding overheat (decrease the discharging temperature by 20 °C) of slabs could be a relevant factor for competitiveness.

5. FOLLOWING STEPS AND BRIEFING

Unit energy consumption is a simple indicator, saying nothing about the real-time operation of technology however the production characteristics will show in energy prices. The unit energy cost indicator can be decreased by leaving the unit energy consumption indicator unchanged, if we synchronize the power demand of technology with the time-dependence of power prices. (High energy consumption periods of production should be scheduled to low price environment.)

Considering the results indicated in *Table 4* we can easily prove the fact that due to the power-of-an-order difference of heat and power consumption it is highly recommendable to start energy efficiency enhancement with furnace optimization and increase its energy efficiency.

Saving on energy, thus unit energy consumption reduction could be achieved by more efficient scheduling of reheating. To validate this statement to the examined technology optimizing is necessary to the data set used for this examination.

REFERENCES

[1] TAN, M.–DUAN B.–SU, Y.–HE, F.: Optimal hot rolling production scheduling for economic load dispatch under time-of-use electricity pricing, 2017. *Mathematical Problems in Engineering,* 2017.

[2] KAPROS T.: *Kamragáz tüzelés hatékonyság vizsgálat*. TÜKI, Tüzeléstechnikai Kutató és Fejlesztő Zrt, Miskolc Egyetemváros, 2012.

[3] SPITTEL, T.–HENSEL, A.: Rationeller Energieinsatz bei Umformprozessen. *Deutscher Verlag für Grundstoffindustrie*, Leipzig, 1983.

[4] BRAUN G.: *Az acél szélesszalag meleghengerlési technológia tervezésének újszerű alapelvei*. PhD-értekezés, Kerpely Antal Anyagtudományok és Technológiák Doktori Iskola, Miskolc, 2003.

Materials Science and Engineering, Volume 42, No. 1 (2017), pp. 78–85.

EXAMINATION OF THE MECHANICAL PROPERTIES OF RESIN BONDED FOUNDRY CORE MIXTURES

LAURA MÁDI[1]–LÁSZLÓ VARGA[2]–TAMÁS MIKÓ[3]

The mechanical resistance of foundry cores to molten metal can be well indicated by bending tests. In order to understand the deformation properties of the cores, the proper interpretation of load-deformation curves is required. Stauder [1] characterised the strength of cores with a modulus based brittleness index (B_M). Synthetic resin cores are brittle in room temperature but capable of permanent deformation in higher temperatures. The correspondence between the changes in the mechanical properties of the cores and the effects of thermal load on the behaviour of the various cores are presented in the article.

Keywords: foundry; core sand; bending test; brittleness index; thermal load

INTRODUCTION

The production technology for castings has developed significantly during the past decade. The production of cylinder head with more and more complex designs could be rather challenging for core makers. The usage of the experience and results gained from sand researches is necessary for creating sand recipes. Due to heat effects, the cores might soften and the buoyancy of the molten metal increases which might cause the movement of the core. Thus, knowing the behaviour of various additives in case of high temperature is important as different moulding mixtures behave dissimilarly during casting and solidification [2]. Resin-bonded core mixtures are brittle when cold but are capable of permanent deformation when hot.

1. FACTORS INFLUENCING THE STRENGTH OF CORES

Many factors influence the mechanical properties of sand cores which can be seen in *Figure 1.* There are two main expectations concerning the mechanical properties of cores. On the one hand, the cores have to endure the thermal and mechanical strain during form filling and solidification caused by hot molten metal. On the other hand, cores should be easily removed after solidification. The strength of cores depends on the origin of the sand as well. The strength of rough sand from the primary site, in case of similar grain size and binder-content,

---

[1] University of Miskolc, Institute of Foundry
Miskolc-Egyetemváros 3515, Hungary
ontlaura@uni-miskolc.hu

[2] University of Miskolc, Institute of Foundry
Miskolc-Egyetemváros 3515, Hungary
ontvlaci@uni-miskolc.hu

[3] University of Miskolc, Institute of Physical Metallurgy, Metalforming and Nanotechnology
Miskolc-Egyetemváros 3515, Hungary
femmiko@uni-miskolc.hu

is always higher than the strength of regenerated, abraded, spherical sands. New sands from two sites, from Frechen (F35) and Sajdikovó (SH32) were compared. The specific surfaces of small particle sized sands are higher, so they have higher reactivity. Too fine-grained sands (sludge <0,05 mm) are not very suitable for form making, as the released gases cannot pass through them and too much binder is absorbed because of their high specific surface. In case of coarse grained sands, the possibility of penetration defects is higher. Thus, the aim of core producers is to work with sands with optimal grain structure and particle distribution that provide good surface quality.

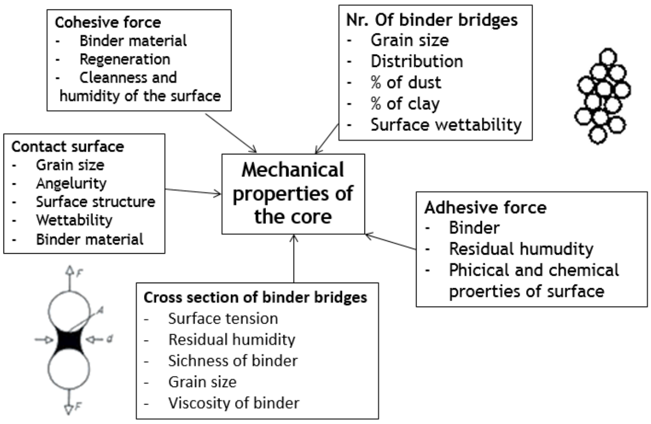

Figure 1
Factors influencing the mechanical properties of cores [2]

The discrete element method (DEM) was developed in the 1970's for the numerical modelling the movement of granular materials and the correlation between grains in case of high number of grains. The method became widely used during the 1990's, when the problems could be solved using computers. Modern software are capable of handling over a million particles. During discrete element modelling, the model consists of easily separable elements with different degrees of freedom. New links can be created and broken between the elements. Equations of motion are solved for each particle. Most discrete element software use completely rigid elements. Thus, the appropriate modelling of various materials requires the definition of the correct connection between the elements.

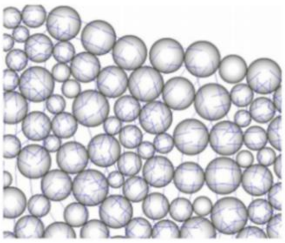

Figure 2
Parts of the discrete element method [1]

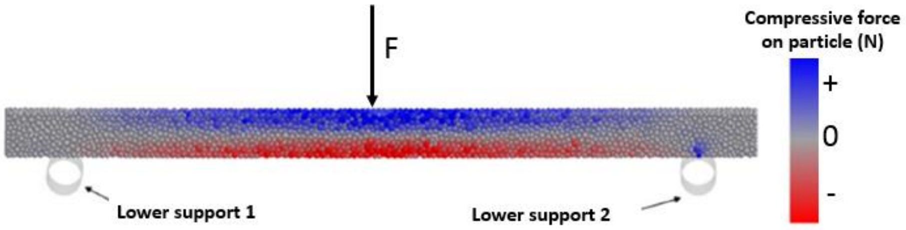

Figure 3
Tensile and compressive forces during three point bending tests [1]

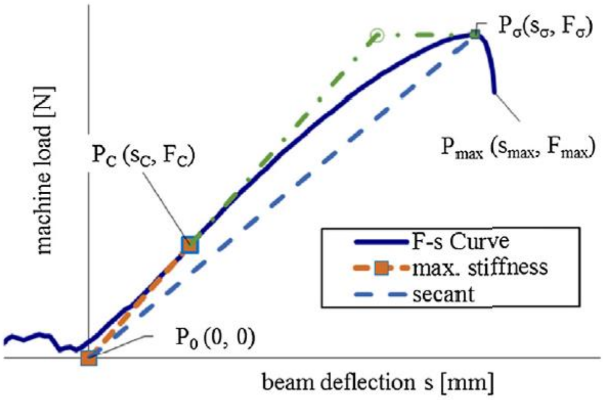

Figure 4
The characteristic points of a machine load-beam deflection curve [1]

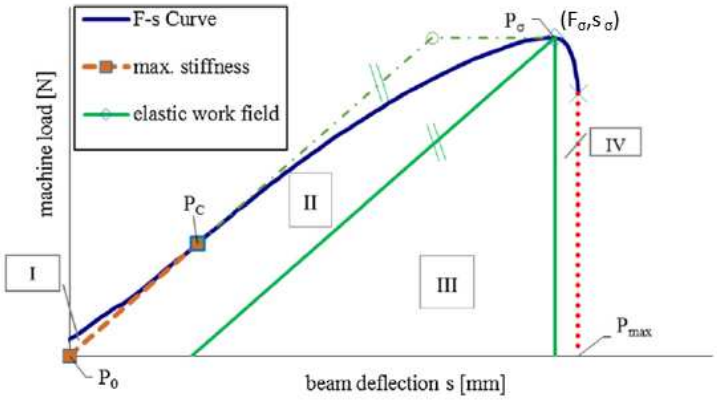

Figure 5
The regions used for the mechanical work evaluation [1]

Using DEM, the tensile and compressive forces in cores can be simulated, as it can be seen in *Figure 3*. Bending tests represent the mechanical resistance of cores to molten metal. The effectively obtained test bar dimensions were 22.7 x 22.7 x 180 mm. The lower support distance *l* was 150 mm and the cross section side length *a* was 22.7 mm, the radius of the cylindrical tool was r = 5mm. Bending strength and the modulus of elasticity can be derived from the load curve. In order to determine the deformation-properties of core sands, knowing the load-deflection curve is essential, which can be seen in *Figure 4* [4].

The regions below the curves in *Figure 5*. can be divided into 4 areas based on the specific points. The nomenclature of the areas can be seen in *Table 1*.

Table 1

Nomenclature for the various work areas used [1]

I.	W_{pl}^{i}	initial plastic work (P_0-P_c)
II.	W_{pl}^{σ}	plastic work until max. stress
III.	W_{el}^{σ}	elastic work until max. stress
IV.	W_{pl}^{f}	plastic work until final breakage

Modulus based brittleness index (B_M) can be determined using the steepness of the curves at points P_c and P_σ, using the following equations:

P_c= maximum stiffness [N/mm]:

$$P_c = \frac{d^2\sigma}{ds^2} = \frac{F_\sigma}{s_\sigma}$$

P_σ= maximum strength [N/mm]:

$$P_\sigma = \frac{d\sigma}{ds} = \frac{F_c}{s_c}$$

$$\sigma_b = E \cdot \varepsilon$$

where:

- σ_b= brittleness bending stress [MPa]
- F_σ= maximum load [N]
- s_σ= displacement in case of maximum load [mm]
- F_c= load in case of elastic deformation [N]
- s_c= maximum displacement of the core without permanent deformation [mm]

$$E = \frac{\sigma_b}{\varepsilon} = \frac{l^3}{4a^4} c_{max}$$

where:

- E= Young modulus [MPa]
- ε= ultimate elongation [%]
- l= lower support distance (150 mm)
- a= cross section side length (22,7 mm)

- c_{sec}= secant stiffness [N/mm]
- c_{max}= maximum stiffness [N/mm]
- B_M= modulus based brittleness index

$$B_M = \frac{c_{sec}}{c_{max}}$$

$$c_{sec} = \frac{F_\sigma}{s_\sigma}$$

$$c_{max} = \frac{F_c}{s_c}$$

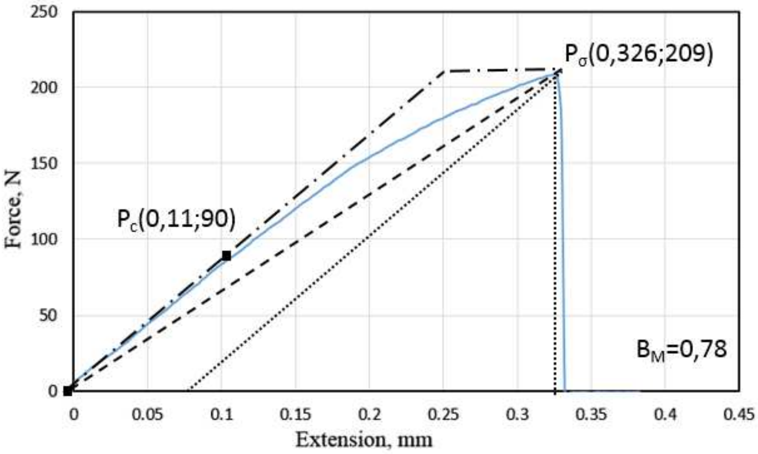

Figure 6

Evaluation of bending curve (CB, SH32 new sand, 0.55% resin content, see under recipe 7)

The modulus based brittleness index from the curve is characteristic to CB-cores [4]. The total expended work of the bending test can be calculated with the following equation:

$$W_M = \int_0^{s_{max}} F(s)dS \approx \sum_{s=0}^{s_{max}} F\Delta s$$

2. MATERIALS-METHOD AND EXPERIMENTAL CONDITIONS

The test bars were prepared with cold- and hot-box processes, using DMPA catalyst in case of cold-box process, under laboratory conditions. The size of a test bar is 22.7 x 22.7 x 180 mm. The effects of diverse grain sizes – fine and medium –, binder quantities and qualities, and thermal load for 5 min at 350 °C on the mechanical properties are demonstrated in the article. A universal Instron 5982 device was used for bending tests, which can be seen in *Figure 7*. The distance between the supports was 150 mm, the cross section are was 22.7 mm. Cylindrical tools with R = 5 mm radius were used for the bending tests. The velocity of the load was 3 mm/min. Stauder et al. [1] examined the effect of load at various velocities. They discovered that in case 50 mm/min load, the value of deflection is decreased and the average bending strength is higher. Slow load makes the plastic deformation of the cores possible. The composition of the mixtures can be seen in *Table 2*.

Figure 7
The universal Instron 5982 equipment

Table 2
Core recipes

	New		**Regenerated (R)**		**Mixed**		**Used**
Resin	SH32	F35	medium (M)	fine	25%U-75%RM	50%U-50%RM	U
CB-0.40%			1	4			
CB-0.55%	7	8	2	5	9	10	11
CB-0.70%			3	6			
HB	14		12	13			

3. DISCUSSION

Bending tests were performed on test bars from the mixtures on room temperature and prepared with 5 minutes of thermal load on 350 °C. Thermal loads were performed in a furnace, and the bending tests were performed right after taking the test bars out of the furnace. The results are presented in *Figure 8* and *9*.

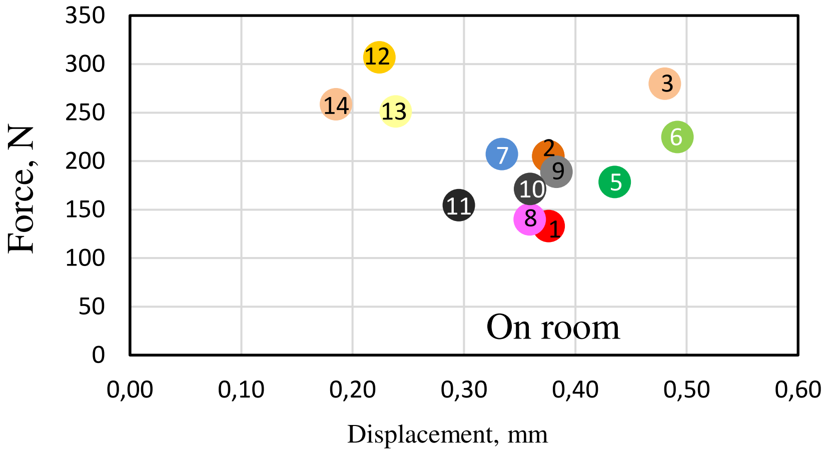

Figure 8
Force-displacement values for fracturing on room temperature

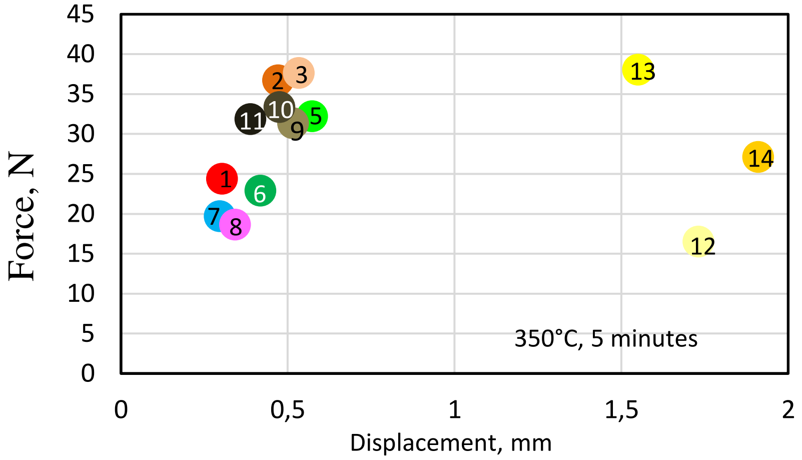

Figure 9
Force-displacement values in case of thermal load

The results in *Figure 8* can be divided into two types. One of them is the cores prepared with hot-box process (12, 13, 14) which have high strength and rigidity. The second one is the cold-box type (1–11). In case of the pairs of 3–6, 2–5 and 12–13 it can be observed, that cores with finer sand matrixes have lower strength but higher plasticity. Cores with similar resin content are a smaller group among cold-box type (7, 8, 2, 5, 9, 10, 11). Increasing resin-content (1–2–3, 5–6) also increases both strength and plasticity. After thermal load on 350°C, the strength of hot-box cores decreased to the values of cold-box mixtures. However, the plasticity of hot-box cores significantly increases, as seen in *Figure 9*. Hot-box cores have better plasticity in case of thermal load than cold-box cores.

CONCLUSIONS

The mechanical resistance of foundry cores to molten metal can be well indicated by bending tests. In order to determine the deformation-properties of core sands, the evaluation of load-deflection curves is essential. Bending strength and the modulus of elasticity can be derived from the load curve. Stauder et al. [1] characterised the strength of cores with a modulus based brittleness index. Artificial resin-bonded sand cores are rigid when cold, but capable of permanent deformation when hot. HB-cores have high strength and low plasticity on room temperature, while CB-cores have low strength and high plasticity. After thermal load on 350 °C, the strength of HB cores decreases to the values of CB-cores, while their plasticity is increased. Cores with finer sand matrixes have lower strength but higher plasticity than medium particle sized sand cores with similar composition.

ACKNOWLEDGEMENT

The research was supported through the New National Excellence Program of the Ministry of Human Capacities. The authors would like to thank Nemak Győr Aluminium Foundry Ltd. for supporting the research, the staff of the Institute of Foundry for helping with the experiments, and Mária Ambrus for her advice.

REFERENCES

[1] BERNHARD, J. S.–KERBER, H.–SCHUMACHER, P.: Foundry sand core property assessment by 3-point bending test evaluation. *Journal of Materials Processing Technology* Vol. 237 (2016), 188–196.

[2] DÉTÁRI A.: *Forma-fém kölcsönhatásainak vizsgálata, különös tekintettel a formázóanyagok újrahasznosíthatóságára*. PhD-értekezés, Miskolc, 2009.

[3] SCHINDELBACHER, G.–KERBER, H.: Umfassende Charakterisierung von Formstoffen mit einer neuen Prüfmethode*, Giesserei, Rundschau*, 2013, Heft 3/4, S. 58–66. (http://www.voeg.at/web/archiv.html)

[4] KERBER, H.–RIEGLER, M.–SCHINDELBACHER, G.–SCHUMACHER, P.: *New possibilitieswith improved green sand testing facilities*. Jan-Blaˇziˇc, M. (ed.), 54th International Foundry Conference. Slovenian Foundrymen Society, Portoroz,Slovenia, 2014, 10.

Materials Science and Engineering, Volume 42, No. 1 (2017), pp. 86–93.

PARTICULATE MATTER AND HEAVY METAL AIR POLLUTION IN THE MIDDLE EAST REGION

TAMÁS MERÉTEI–PÁL ZOLTÁN BITE–
CSONGOR BÁTHORY[1]–ZSUZSANNA BOLLA[2]

The purpose of the research was to evaluate the background particulate matter pollution originating from the barren, desolate desert region and from the sea side. Another objective of this paper is to show the metal content in PM_{10} in a major city in the GCC region grouped by sources and compare them with the results measured in Hungary.

Keywords: PM_{10}, $PM_{2.5}$, heavy metal air pollution

INTRODUCTION

One of the most developing areas around the world is in the Middle East region within those countries of the Gulf Cooperation Council (GCC), where the focus on environmental protection is increasing at a great extent. Beside the noise, groundwater and nature protection, more and more emphasis is placed on air quality protection. The residents are annoyed by the busy roadways and many of the industrial plants, but the main source of annoyance is still the transportation. The number of cars per capita, the built dwelling houses and buildings under construction even at 30 meters from the edge of the highways as well as regulatory failures do not facilitate the job of the local environmental authorities. Extreme weather and terrain conditions make it a challenge for even the best teams and monitoring instruments to carry out evaluated air quality measurements.

1. EMISSION SOURCES

The research had begun to map the main anthropogenic emission sources. One of the major emission sources in major cities of the GCC region is the transportation. In our estimation from the emitted PM_{10} it is around 63% (including road traffic, seaport and airport emission). The second major source is the emission of the industry with 15%, after that the non-road emissions and power plants around 10%.

1.1. Road traffic

Road traffic is responsible almost for the half (43%) of the transportation's PM_{10} emission. *Table 1* shows the development of vehicle number per 1000 capita of Hungary and that of the GCC. Data are credible from western counties, and is limited from eastern regions due to the publicity of statistics. Qatar and Kuwait are much smaller and have less desert areas,

---

[1] csongor666@gmail.com
[2] info@vibrocomp.com

so the densely populated area is the reason of the higher numbers. It is also worth mentioning, that the City of Dubai's vehicle density was 540 per 1,000 people in 2015 [1].

Table 1

Vehicle per 1000 capita, 2005–2014 [2] [3]

Year	**2005**	**2006**	**2007**	**2008**	**2009**	**2010**	**2011**	**2012**	**2013**	**2014**
Hungary	329	337	345	351	347	345	342	347	355	366
Kuwait	426	426	430	429	433	444	458	469	475	482
Qatar	443	381	390	449	421	413	420	432	432	442
Saudi Arabia	145	147	153	158	165	173	183	193	197	202
United Arab Emirates	193	170	180	204	185	173	179	188	202	216

Figure 1 shows the percentage change in vehicle per 1000 capita values compared to the previous years. The most significant changes were in Qatar and the United Arab Emirates and by evaluating these and Hungary's values the effect of the 2008 world economic crisis can also be observed. From 2011 – except Hungary-, the values show an increasing tendency, which even lasts to the present day. This hectic, but strong growth tendency makes the road traffic the most important and key player in case of emission sources.

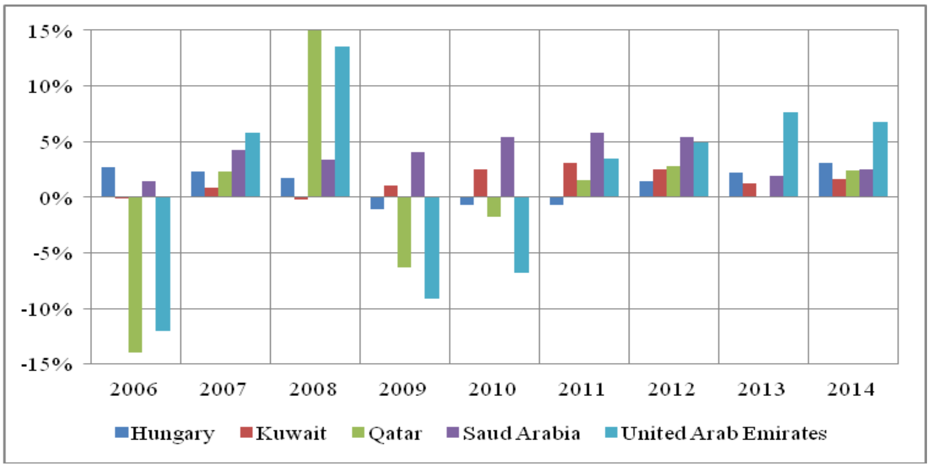

Figure 1

Percentage changes in vehicle per 1000 capita values, 2005–2014

Data are not available corresponding to the composition of the vehicle fleets and due to the lack of emission categories it is even hard to estimate. Based on observations, it can be said that among individual types of passenger cars, the most powerful models are distributed to the GCC area. Heavy trucks are usually in worse condition, the use of the latest models and the use of catalyzer is not typical in this area. In our estimation vehicle fleet correlate well with the German passenger car fleet of 2010 and the German heavy duty vehicle fleet of 2008.

1.2. Seaport

Three ports from the GCC region are among the top 50 world container ports in 2015. These were the Jebel Ali Port (United Arab Emirates) being the 9th with 15.6 million containers, the Jeddah Port (Saud Arabia) being the 36th with 4.19 million containers and the Sharjah Port (United Arab Emirates) being the 44th with 3.4 million containers [4]. These numbers show that the ports' emissions can't be neglected in the Arabian Gulf. As part of the International Convention for the Prevention of Pollution from Ships (MARPOL), the International Maritime Organization's (IMO) members agreed at a global 0.5 Vol% limit on sulfur content for 2020. This is less restrictive than European and North American regulations, but 0.5% still represents a significant cut from the 3.5% global limit currently applied and it would make the Middle-East's current regulations redundant [5]. Besides the pollution from ships, the emission of service facilities and auxiliary engines and machines are also contributing to the overall emissions.

1.3. Airport

Airports have a significant traffic in 24 hours and usually are close to the city center. Airplanes are flying at a low altitude over the city, and the auxiliary vehicles, engines and traffic around the airports also makes airports a considerable source of air pollution. As the cities are growing they are likely to be built around the airports as well, therefore residential building will be too close to the airports, leading to a noise and air quality problem as well. Restructuring of airports and/or expansion is expected due to the above reasons. For example the secondary airport of the Emirate of Dubai (DWC), which is at the edge of the city, is now being expanded from the current capacity of 5 million passengers a year to 26 million by 2018 [6].

1.4. Industry

The main activity is corresponding to the petroleum industry – pollution sources mainly corresponding to oil refining and the use of petrochemicals products. Metal industry is also present due to the ports' import capacity, but because of lack of local raw materials it is not significant. The beverage and food factories are significant and following the needs of the market, which is of a high extent.

Lot of small garages and workshops are not controlled in terms of air quality. Public waste oil delivery locations were not found. Concrete industry is largely present with vigorous utilization, because of the individuals' building needs and also large public investments. Filtration of stack gases is rudimentary, small and large factories have filters, however separators are rarely incorporated into those.

1.5. Power Plant

Emission inventory is to be improved because presently there is no well-developed mandatory emission collection system. Two or three times larger Combined Cycle Gas Turbine (CCGT) power plants are in a major city as much as Paks in Hungary (2000 MW), for example, the Emirate of Abu Dhabi has a 9940 MW, the Emirate of Dubai has a 3066 MW, whole Kuwait has a 5000 MW and whole Qatar has over 9000 MW power plants [7]. The power plants are usually built together with desalination plants to secure the water supply in the subtropical climate.

2. SAMPLING METHOD

2.1. Sampling points by types of sources

The sampling points were appointed by the sources and the residential areas like Background, Road, Port, Airport, Industry, Residential and Rest Area. Sampling results are averaged by sources' type.

2.2. Sampling method

PM_{10} and $PM_{2.5}$ were sampled with a high volume sampler using a quartz filter and were analyzed by gas chromatography to specify the metal content in PM_{10}. The evaluation focused on lead (Pb), nickel (Ni), cadmium (Cd) and arsenic (As) metals. Samples to be analyzed for the sand and sea salt content were treated with PTFE filters to be measurable. Sampling has been carried out during winter and spring time in 2015–2016.

3. SAMPLING RESULTS

3.1. PM_{10} and $PM_{2.5}$

15% of PM_{10} values exceeded the 50 $\mu g/m^3$ values. 17% of the sampled values were over 100 $\mu g/m^3$, mainly at Industry and Road sampling point types, and even at Background. The average PM_{10} value was 75 $\mu g/m^3$.

$PM_{2.5}$ was sampled at the following sampling point types: Background, Road, Airport, Industry and Residential. The average $PM_{2.5}$ value was 28 $\mu g/m^3$. The results showed that the average $PM_{2.5}$ content in PM_{10} was around 40%. The lowest content was found at Background, where it was 23%. $PM_{2.5}$ values were at the same level, except one Industry sampling point was higher. At this particular point, PM_{10} was the lowest as well, probably it occurred because of the meteorological conditions during sampling (rain was recorded).

Sea salt (NaCl) and quartz (SiO_2) were analyzed from the PM_{10} samples to find out the sand and sea salt content. The analyses' results showed that 56% of the weight of sampled PM_{10} is SiO_2 and 3% is NaCl *(Figure 2)*. The salinity of particulate matter is approaching the average salinity of sea (3.5%). Soil and sand composition is unknown at the sampled area. Quartz could also come from different sources (construction activities, wear of road pavement and re-suspended road dust). It is important to notice that a significant proportion of PM_{10} is coming from natural sources, as that percentage distribution of sea salt and quartz in PM_{10} was the same in background samples.

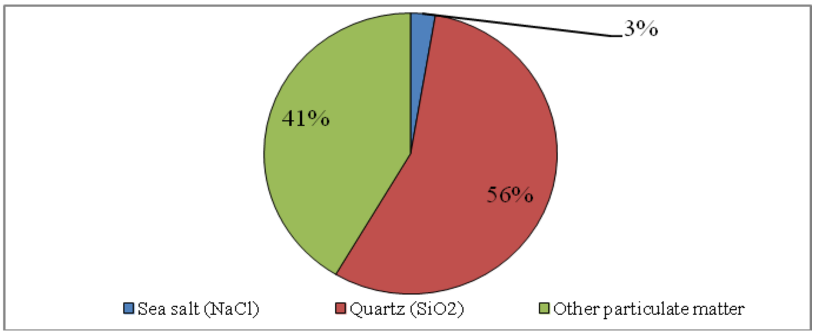

Figure 2

Average percentage distribution of sampled PM_{10}

The sampled values were averaged by sample areas, which represent the seven (7) source types and the average values. To compare the Hungarian data [8] we have chosen six (6) monitoring station from the stations of the Országos Légszennyezettségi Mérőhálózat (OLM) (National Air Pollution Monitoring Network), where PM_{10} and metal contents were monitored during 2015. Hungarian samples were taken in 4x2 weeks periods during 24 hours according to standards [8]. *Table 2* shows the chosen monitoring stations, their type and the conformity to source types. The conformity is acceptable, Gilice tér is a Rural background, but approximates the Airport type.

Table 2

Conformity of OLM monitoring stations

Monitoring Station	**Monitoring Type**	**Source Type**
K-Puszta	Background	Background
Budapest, Széna tér	Urban traffic	Road
–	–	Port
Budapest, Gilice tér	Rural background	Airport
Dunaújváros, Apáczai Csere J. u. 3.	Urban industry	Industry
Győr, Szigethy Attila út	Urban background	Residential
Sarród, Nemzeti Park	Rest area	Rest Area
Average of Above	Average	Average

The comparison of PM_{10} values is shown on *Figure 3*. All Hungarian values are less than the GCC values. Background is higher in average at GCC as well and the rest area in GCC is significantly higher compared to the pattern in Hungary. Port area is next to the sea side, so the background pollution from desert side does not appear there.

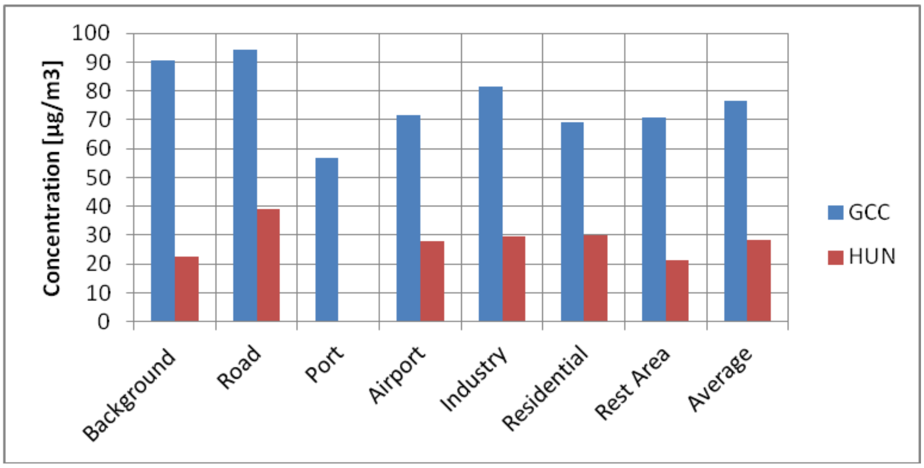

Figure 3

Average PM_{10} values [8]

$PM_{2.5}$ results are limited in both regions; therefore we did not compare those values.

3.2. Lead (Pb) and Nickel (Ni)

The metal content of PM_{10} was calculated to part per million percentage (ppm) by the weight of PM_{10} per m^3 and by the weight of the metal per m^3. The values of different regions are comparable with this method; the percentage distribution of metals shows the typical composition. The Pb and Ni content of samples can be seen on *Figure 4*.

Pb content in percentage was three times higher (Airport) or even five times higher (Road) in Hungary, except at the Rest Area, where it was almost the same percent. As the Pb content is almost the fifth at Background in GCC, it can be concluded that Pb pollution is not significantly coming from desert and sea side.

It can also be seen that the Ni content, in Hungary has much lower percentage. At the Port side in GCC it is the highest, but also the Industry and Rest Area are outstanding in Ni content. The high Ni content at Background added to the other sample areas, except covered areas, like paved road (Road, Airport) and lawn or built territories (Residential). It can also be seen that Pb and Ni contents are the lowest in GCC at Road.

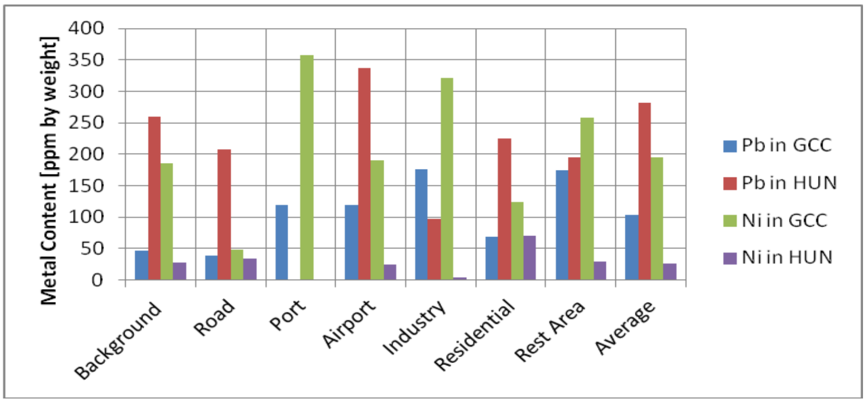

Figure 4
Lead and Nickel content [8]

3.3. Cadmium (Cd) and Arsenic (As)

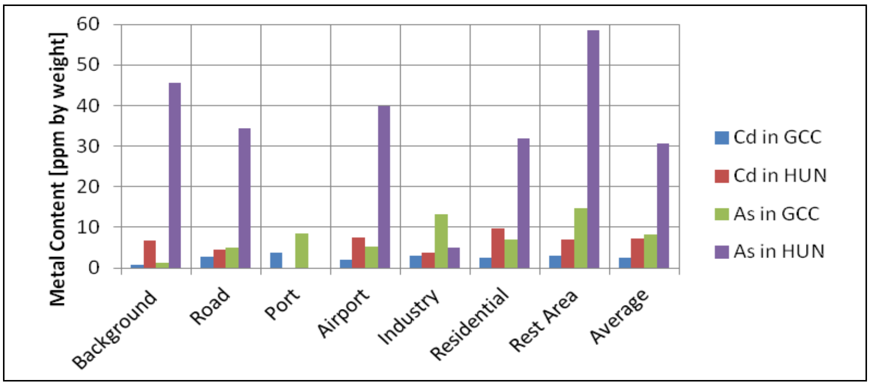

Figure 5
Cadmium and Arsenic content [8]

Figure 5 shows the Cadmium and Arsenic metal content of average PM_{10} samples. Cd content in percentage is much lower in GCC, especially at Background. The ppm values in GCC and Hungary are near to each other at Industry and Road. The lowest Cd percent is at Industry in Hungary. Residential Area has four times more percentage Cd content in Hungary than in GCC.

High As percentage content in Hungary is immediately noticeable. In GCC this value is the highest at Rest Area. But at Industry types, GCC values are higher than in Hungary – actually these are the lowest in Hungary. Except Industry, as content in percentage is much lower in the GCC, especially at Background.

CONCLUSION

The examined PM_{10} values are higher in the GCC than in Hungary. In GCC the natural background sources are contributing more to the PM_{10} values. In Hungary the high PM_{10} values are usual measured during winter time due to the domestic heating; the background pollution isn't significant compared to GCC.

Surrounding of roads have the highest PM_{10} values in both regions. Compared to this, examined metal percentages are the lowest. It means that a significant part of PM_{10} samples are mixed with other components. PM_{10} emission of road traffic is mostly composed of vehicles engine emission, wear of road pavement and re-suspended road dust. Based on the high SiO_2 content and low Pb percentage of PM_{10} samples in the GCC, proportionally next to the background pollution, the re-suspended road dust is a significant emission source.

Port area is next to the sea side, so the background pollution is not significant there. Pb and Ni percentages can be higher because of the lack of deserts' natural emission, and the industrial activities nearby.

Airport has less Cd, As and Pb percentage in the GCC as in Hungary and more Ni. PM_{10} values are less in the GCC than the Background value. The Hungarian sampling point was in a rural area therefore did not perfectly represent the effect of nearby airport.

Industry in the GCC has the second high PM_{10} value, examined metal percentages are outstanding. Besides, there are higher Pb and As percentages than in Hungary.

Residential has one of the lowest Pb, Ni and Cd percentage in the GCC and As percentage isn't even over the Average. In Hungary Pb and Ni are over, Cd and As are under the Average.

Rest Area has the same PM_{10} values as Residential in the GCC, the metal contents are, however, lower, due to the vegetation and less road traffic. The same situation is present in Hungary, but Ni and As percentages are higher than in the GCC.

Ni content in percentage is much lower in Hungary, especially at Industry. The higher values in the GCC require further investigation. As content in percentage is much lower in the GCC – except Industry – especially at Background. The higher values in Hungary require further investigation.

The parts per million calculation method of metal content in PM_{10} samples eliminates the high-value differences in $\mu g/m^3$ dimension and make the values comparable in the GCC and in Hungary.

If we consider that high proportion of PM_{10} in the GCC is coming from background, it is hard to imagine how to reduce, but environmental regulations and best available technologies are good options to decrease the anthropogenic air pollution to a sustainable air quality level. Although the Hungarian and the GCC regions must face different challenges, we should keep an eye on countries, which do not understand the word “impossible”, waiting for any new breakthroughs in order to provide a more livable environment.

REFERENCES

[1] Gulf News: For every two Dubai residents, there is one car. http://gulfnews.com/news/uae/for-every-two-dubai-residents-there-is-one-car-1.1472177 (Downloaded: 2017. 06. 25.)

[2] Organisation Internationale des Constructeurs d’Automobiles (OICA) – World vehicle in use 2014

[3] United Nations: World Population Prospects: The 2015 Revision, July 2015

[4] Top 50 world container ports. http://www.worldshipping.org/about-the-industry/global-trade/top-50-world-container-ports (Downloaded: 2017. 06. 25.)

[5] Asia Weekly: Shipping’s Dirty Secrets. https://projects.asiaweekly.com/shippings-dirty-secrets/ (Downloaded: 2017. 06. 25.)

[6] Dubai Airport. http://damasterplan.ae/da-masterplan/dwc-passenger-terminal-expansion/(Downloaded: 2017. 06. 25.)

[7] Global Energy Observatory. http://globalenergyobservatory.org (Downloaded: 2017. 06. 25.)

[8] Országos Meteorológiai Szolgálat: Az OLM 2015. évi szálló por PM10 és PM2.5 mintavételi programjának összesítő értékelése, ÉLFO LRK Adatközpont, 2016. november

Materials Science and Engineering, Volume 42, No. 1 (2017), pp. 94–101.

FILLING SIMULATION OF TILT CASTING

DÁNIEL MOLNÁR[1]

Reliable fluidity data for commercial aluminium foundry alloys are not readily available. However, such data are important in the optimization of mould filling calculations. The term fluidity in the foundry is used to indicate the distance of a molten metal can flow in a mould of a constant cross-sectional area before it solidifies. This definition is different from the definition presented in physics which describes fluidity as the inverse of viscosity, a fundamental temperature related property of a liquid.

Fluidity is mainly a complex technological property and it depends upon many factors which can be categorized as follows:

1. Metal variables: chemical composition, solidification range, viscosity, heat of fusion.
2. Mould and mould/metal variables: heat transfer coefficient, mould and metal thermal conductivity, mould and metal mass density, specific heat, surface tension.
3. Pouring method variables: gravity casting, tilt casting, low pressure die casting, high pressure die casting.

By carefully selecting the appropriate combination of these variables, fluidity can be controlled. This plays a key role for thin walled castings because misruns, often encountered in these castings, are a result of insufficient fluidity of the liquid metal. It is not easy to control fluidity due to the large number of variables involved. However, if variations in fluidity due to uncontrolled factors can be estimated, defect problems, such as unexpected misruns and/or cold shuts, can be overcome and process costs reduced.

Keywords: gravity casting, tilt casting, computer simulation

1. THEORETICAL BACKGROUND

1.1. Solidification of alloys

Unlike pure metals and eutectics, the flow of alloys ceases at the leading tip of the flowing stream. As the solute concentration is increased, the mode of solidification changes from growth of columnar grains with more or less planar front (for pure metals and dilute alloys) to the formation of equiaxed dendrites or columnar dendrites where the dendrite arms fracture forming equiaxed grains (for solute rich alloys). These grains flow downstream with the liquid metal, until a critical fraction solid is reached and the flow stops by choking at the tip of the freezing metal as shown in *Figure 1* [1–3].

---

[1] University of Miskolc, Institute of Foundry Engineering
Miskolc-Egyetemváros 3515, Hungary
daniel.molnar@uni-miskolc.hu

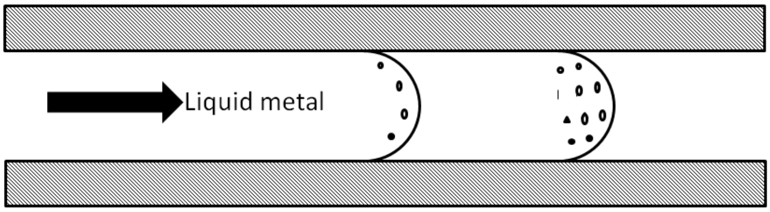

Figure 1

Schematic representation of solidification in alloys

Flemings developed simplified mathematical models for the fluid length of metals that are poured into a cylindrical channel in a mould [2, 5]. For the fluidity of alloys:

$$L_f = \frac{A\rho v(f_s^{cr}H + C\Delta T)}{Sh(T - T_{cr})}\left(1 + \frac{B}{2}\right) \tag{1}$$

where:

L_f	[mm]	fluid length
A	[mm^2]	mould surface area
ρ	[kgm^{-3}]	density
v	[mms^{-1}]	velocity of metal flow
f_s^{cr}	[%]	critical fraction solid
H	[kJkg^{-1}]	heat of fusion
C	[kJkg^{-1}K^{-1}]	specific heat
ΔT	[K]	temperature interval
S	[mm]	circumference of the mould channel
h	[Wm^{-2}K^{-1}]	heat transfer coefficient
T	[K]	temperature of the alloy
Tc	[K]	coherency temperature
h	[Wm^{-2}K^{-1}]	heat transfer coefficient
α	[m^{2}s^{-1}]	thermal diffusivity of mould
Δy	[mm]	choking range
K	[Wm^{-1}K^{-1}]	thermal conductivity

$$B = \frac{h\sqrt{\pi\alpha\Delta y}}{K\sqrt{v}}$$

The method greatly simplifies the fluid-flow problem by neglecting friction and acceleration effects. Flemings' model is based on the assumptions that:

- the solid particles form during the flow in the fluidity channel and travel downstream with the liquid;
- the flow stops when the fraction solid near the flow tip reaches a certain value (critical fraction solid, f_s^{cr});
- the flow velocity is constant until the flow stops.

1.2. Numerical modelling of fluidity

Fluid flow pays an important role for the production of sound castings. Mould filling is the first step of every casting process. For many castings, mould filling determines the quality of the final product. Excessive turbulence, air or gas entrapment, premature solidification, form erosion, any of these factors can spoil the final product. After the mould filling phase, during solidification of castings fluid flow comes again into play. Buoyancy effects, segregation of alloy components, feeding flow are the examples of fluid flow phenomena that can take place during the solidification. Modelling of fluid flow is required if the mentioned phenomena need to be taken into account.

In order to be able to model filling properly, the following equations must be in general b solved:

- The three momentum equations (momentum conservation) together with a suitable constitutive law relating stresses and velocities, typically incompressible, Newtonian fluid for metals.
- The continuity equation (mass conservation).
- The energy equation (energy conservation).

Important phenomena that should be taken into account are e.g. temperature dependent viscosity and the tracking of free surfaces. These non-linear phenomena are often taken into account in an explicit manner in the numerical formulation which means that very small steps should be taken [4].

1.3. Effect of different parameters on fluidity

Composition is one of the main factors influencing fluidity. Small alloying additions to pure metals reduce fluidity and the fluidity of unalloyed aluminium is reduced with decreasing purity. The fluidity of aluminium-silicon alloys increases with increasing silicon content reaching a maximum at 17–18wt% silicon. The fluidity of aluminium-silicon alloys has a maximum at a silicon content well above the eutectic composition. After this maximum in fluidity, further additions of silicon will reduce the fluidity due to the increase in number of proeutectic silicon particles interfering with the metal flow. Hence, maximum fluidity will be achieved at a silicon content where the increased interference of proeutectic silicon compensates for the increased heat of fusion from the formation of silicon. [3]

Chemical composition plays an important role on castability because it influences casting properties and defects, e.g. hot tearing. The solidification range strongly influences the mode of solidification and it has been shown that the mode of solidification significantly affects the fluidity of the melt. Fluidity length is inversely proportional to the solidification interval of the alloy, i.e. mushy alloys which solidify with a large solidification range have lower fluidity than alloys which solidify with a short freezing range. [2, 3]

Superheat, i.e. the difference between the casting temperature and the liquidus temperature, is also a key factor influencing fluidity. The fluidity increases with increasing superheat for a given alloy composition. The increase in melt temperature by 1 ºC, in the temperature interval 700–760 ºC, increased the fluidity length by 1%. A linear relationship between pouring temperature and fluidity was shown for all investigated alloys. Increasing the pouring temperature, and hence the melt superheat, delays the nucleation and growth of fine grains at the tip of the flowing metal in the test channel, hence the fluidity length increases.

Fluidity also depends on the pressure height which forces the liquid metal through the pipe that forms during solidification in a narrow channel. Thus, one may expect that the taller the sprue the greater the fluidity. However, unnecessarily long sprues and special pouring cups can be avoided, which will result increased sand yield and reduced costs.

Viscosity of molten metals is quite low. Studies have shown that changes in viscosity with temperature and/or slight changes in composition are not great enough to account for the observed variation in fluidity. [6]

Ratio of fluid phase has a significant effect on the viscosity of the melt:

- Under 10% of solid phase ratio: Newtonian liquid.
- Between 10-20% of solid phase ratio: non-Newtonian liquid with relative viscosity.
-

$$\eta_r = (1 - 2{,}5\varphi)^{-1}\eta_0 \tag{2}$$

- Between 20-40% of solid phase ratio: non-Newtonian liquid with modified relative viscosity:
-

$$\eta_{r_{mod}} = (1 - 2{,}5\varphi - a\varphi^2 + b\varphi^3)^{-1}\eta_0 \tag{3}$$

- Over 40% of solid phase ratio: no filling.

where:

η_0	[10^{-5} m^2s^{-1}]	Viscosity of the Newtonian liquid
φ	[%]	Ratio of the solid phase
a, b	[-]	Constants

2. SIMULATION OF THE TILT CASTING PROCESS

The method of simulation can be seen on *Figure 2*.

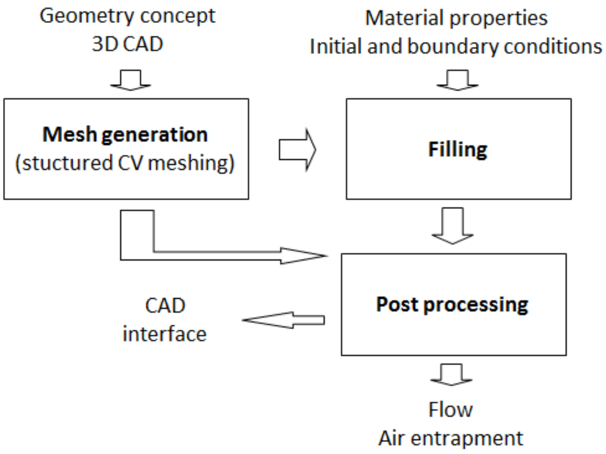

Figure 2
Method of simulation

The filling process is the point in manufacture when most of the defects are introduced into the cast part. Tilt casting solutions for gravity pouring could be described as damage limitation exercises. Here a Control Volume model is used to simulate the tilt casting process of an aluminium casting. The target of the experiments were to identify the critical process parameters and build a simulation protocol by the help of several tilt casting processes and geometries can be modelled and examined. Main factors of tilt casting are:

- If tilt casting is initiated from a tilt orientation at or below, the horizontal, during the priming of the runner the liquid metal accelerates downhill at a rate out of the control of the operator. The metal runs as a narrow jet, forming a persistent oxide flow tube. In addition, the velocity of the liquid at the far end of the runner is almost certain to exceed the critical condition for surface turbulence. Once the mold is initially inclined by more than 10° below the horizontal at the initiation of flow, it is no longer possible to produce reliable castings by the tilt casting process.
- Tilt casting operations benefit from using a sufficiently positive starting angle that the melt advances into an upward sloping runner. In this way its advance is stable and controlled. This mode of filling is characterized by horizontal liquid metal transfer, promoting a mold filling condition free from surface turbulence.
- Tilt filling is preferably slow at the early stages of filling to avoid the high velocities at the far end of the running system. However, after the running system is primed, speeding up the rate of rotation of the mould greatly helps to prevent any consequential non-filling of the castings. [7]

Technological steps of tilt casting process can be seen on *Figure 3*.

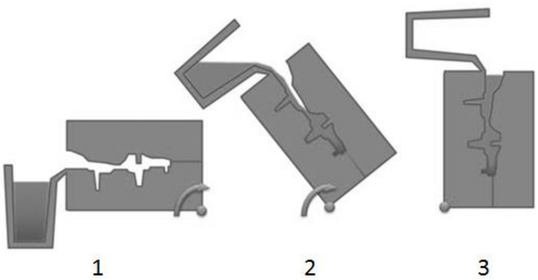

Figure 3
Technological steps of the process

1. Pouring all the required melt to the pouring ladle by controlling the following parameters:
   Gating point position of the melt to the ladle (X, Y, Z coordinates), diameter of the entering metal stream (mm), angle of the entering metal stream (°), pressure height of the melt (mm), velocity of pouring (kg/s), friction factor (%), amount of poured alloy (kg).
2. Achieving the tilt movement by controlling the following parameters:
   Downtime after filling (s), filling stop criteria (kg), initial position of the geometry (CAD), direction of rotation, centre point of rotation (X, Y, Z coordinates), axis of rotation (X, Y, Z), time of tilt (s), tilt angle (°).

3. Solidification calculation by controlling the following parameters:
   Material properties (chemical composition, latent heat, percolation threshold, nucleation ratio, phase diagram, heat conduction, specific heat, density, viscosity, heat transfer coefficient), pouring temperature, temperature values (cope, drag, core, environment), time of removal.

In the simulation constant and variable parameters were altered to achieve total cavity filling. A standard aluminium alloy was poured into a permanent metal die made of alloyed steel. The cores were produced with cold-box technology on 200 °C application tempe-rature. The environment was air on 30 °C temperature. During filling the diameter of the liquid alloy stream was 80 mm and the tilt angle was 55°. Variable parameters can be seen in the experimental model and in *Figure 4*.

Table 1
Experimental model

Number	**Melt**	**Drag & Cope**	**Drag tower**	**Cope tower**	**Pressure height**	**Pouring velocity**	**Poured metal**	**Time of tilt**	**Venting**
	Temperature								
	°C	°C	°C	°C	mm	kg/s	kg	s	
1	730	400	320	400	2	1.6	2	5	No
2	730	400	320	400	5	2.55	1.5	5	No
3	730	400	320	400	5	3.33	2.8	3	No
4	730	400	320	400	4	2.98	2.3	3	No
5	730	400	320	400	4	2.98	2.3	4	No
6	730	400	320	320	4	2.98	2.3	4	No
7	750	450	420	420	4	2.34	2.37	4.5	Yes
8	750	450	450	450	4	2.98	2.37	4.5	Yes
9	750	450	420	420	4	2.98	2.37	3	Yes

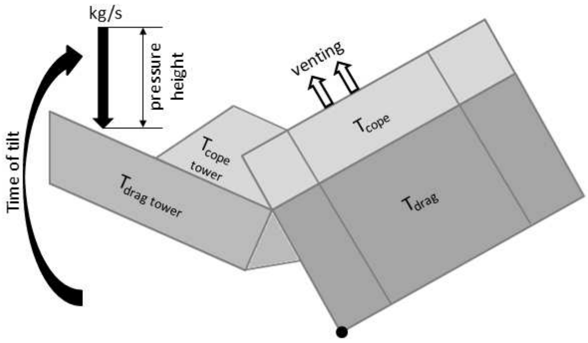

Figure 4
Variable parameters

2.1. Post-processing

- In Experiment 1–2. not enough metal was poured to the pouring ladle. The pouring velocity was too low so the melt freezes in the gating system. The entire casting cavity is unfilled. Pouring velocity and the quantity of the melt were increased to avoid freezing.
- In Experiment 3. the enlarged melt quantity helps to fill the cavity but unfilled areas detected in the lower- and upper part of the geometry. Pressure height, pouring velocity and the quantity of melt were changed to reach better filling of the cavity.
- In Experiment 4–6. the time of tilt was changed and it is determined that without venting the geometry cannot be filled completely.
- In Experiment 7–9. venting is defined to ensure the filling of the cavity. Venting is accomplished in the area of the riser head. The temperature of the die elements were increased to keep warm the melt and to avoid cold flow. The amount of the poured metal was increased till the technology limit and the time of tilt was determined correspondently to the measurements.

Using the determined technological parameters the complete cavity is filled without turbulences. Both critical parts of the cavity can be filled without significant air entrapment. Venting is effective, the geometry of the venting channel is adequate and the position of venting is applicable.

In *Figure 5* dash line represents the cavity and the dark areas shows the amount of entrapped air in the cavity. Target is achieved while all air entrapment managed to eliminate from the cavity.

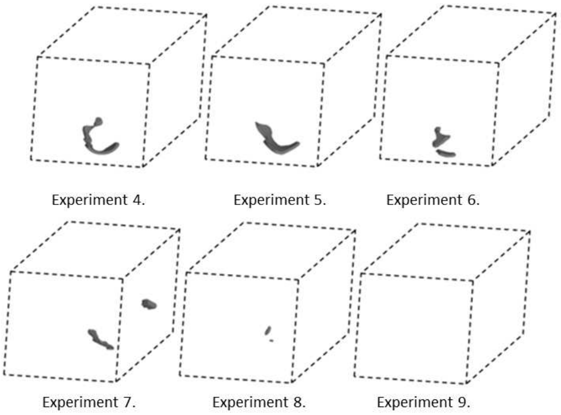

Figure 5
Entrapped air in the cavity

From the point of view of the adequacy of simulation the following factors played the main rules: tilting parameters, temperature values and die materials. The most important results of simulation, besides of the determination of technological parameters, are the identification of the critical process parameters.

- Geometrical adequacy: height of the pouring basin, cross-section of the basins' nose, geometry of the flow channel between the basin and the gating system.

- Pouring conditions: consideration of liquid contraction, cross-section of the melt stream, definition of pressure height to avoid splashing.
- Material properties and temperature adequacy: definition of the material and the temperature of the basin, application of refractory coatings to avoid melt cooling.
- Tilt conditions: filling stop criteria, rotation options, downtime after filling, time of tilt, tilt angle.

REFERENCES

[1] LOPER, C. R.: *AFS Transactions*. 1992, 533–538.

[2] FLEMINGS, M. C.: *Solidification Processing*. McGraw-Hill Inc., London, 1974.

[3] KIM, J. M. et al.: *AFS Transactions*. 1995, 521–529.

[4] HATTEL, J.: *Fundamentals of Numerical Modelling of Casting Processes.* Polyteknisk Forlag, Lyngby, Denemark, 2005.

[5] FLEMINGS, M. C. et al.: *AFS Transactions.* 1961, 625–635.

[6] MOLNAR D. et al.: *Foundry Trade Journal.* 2017, 26–29.

[7] CAMPBELL, J.: *Complete Casting Handbook.* 2011, 932–948.